Construction of a solid-state RGB laser

Jimmy Johansson

KTH
VETENSKAP
OCH KONST

**ROYAL INSTITUTE
OF TECHNOLOGY**

Master of Science Thesis

Laser Physics
Department of Applied Physics
School of Engineering Sciences
Royal Institute of Technology

Stockholm, Sweden 2007

Abstract

In this master thesis project, a solid-state red-green-blue (RGB) laser was built. The project consisted of two parts.

In the first part, an actively Q-switched diode-pumped solid-state laser was constructed. As laser gain medium, a Nd:YVO$_4$ crystal, which lased at 1064 nm, was used. The Q-switch was a home built electrooptic modulator based on two RTP crystals. The modulator had a shortest rise time of 15 ns. At a pulse repetition frequency of 1000 Hz, a pulse energy of 39 μJ was obtained from the laser. The peak power was 1.1 kW and the pulse length was 25 ns. Imperfect birefringence compensation in the electrooptic modulator is believed to be the limiting factor for the pulse energy.

In the second part of this project, three different frequency conversion stages were considered. The purpose of the frequency conversion stages was to convert light at 1064 nm into red, green and blue light. Based on simulations in the software SNLO, one of the stages was chosen for experimental realization. The practical setup consisted of an optical parametric oscillator (OPO), with a periodically poled KTP crystal as nonlinear medium. When pumping this OPO with frequency-doubled light at 532 nm, a signal at 632.0 nm and an idler at 3362 nm were obtained. At a pump energy of 0.5 mJ, the pump depletion was measured to 30 % and the conversion efficiency to 18 %, meaning 0.07 mJ of red energy.

After the OPO, a sum frequency generation (SFG) process between the pump and the idler gave blue at 459.3 nm. The blue energy was however low, only 2 μJ. A way of increasing the conversion efficiency of the SFG process would be to achieve a better overlap between the spectrum of the idler and the acceptance bandwidth of the SFG process. Therefore the bandwidth of the idler was indirectly narrowed by using a volume Bragg grating as incoupler to the signal-resonant OPO. The bandwidth of the signal was in this way decreased by 50 % and the idler bandwidth was believed to have decreased by the same fraction. However, the blue output energy did not increase as expected.

Final experiments showed that the blue output energy was strongly dependent on the beam quality of the pump at 532 nm; when the beam quality was changed from $M^2 = 6$ to $M^2 = 1.5$, the blue output pulse energy increased from 2.4 μJ to 5.0 μJ.

Sammanfattning

I det här examensarbetet har en röd-grön-blå (RGB) fasta tillståndslaser byggts. Projektet bestod i princip av två separata delar.

I den första delen av projektet konstruerades en aktivt Q-switchad diodpumpad fasta tillståndslaser. Som lasermedium användes en Nd:YVO$_4$-kristall som lasrade vid 1064 nm och som Q-switch användes en hemmabyggd elektrooptisk modulator baserad på två RTP-kristaller. Modulatorn hade som bäst en stigtid på 15 ns. Vid en pulsrepetitions-frekvens på 1000 Hz gav lasern pulser på 15 μJ med en toppeffekt på 1.1 kW och en pulslängd på 25 ns. Den begränsande faktorn för puls-energierna var troligen ofullständig kompensation av dubbelbrytningen i den elektrooptiska modulatorn.

I den andra delen av projektet behandlades frekvenskonvertings-steget, det vill säga den modul som skulle omvandla ljus med våglängd-en 1064 nm till ljus med våglängder i det röda, gröna och blå området. Tre olika frekvenskonverteringssteg utvärderades först i programvaran SNLO, för att få en uppskattning av vilken verkningsgrad som de kunde förväntas ge. Baserat på simuleringarna valdes ett konvertingssteg ut för att undersökas experimentellt. Den praktiska uppställning bestod av en optisk parametrisk oscillator (OPO), med en periodiskt po-lad KTP-kristall som icke-linjärt medium. När OPO:n pumpades med frekvensfördubblat ljus vid våglängden 532 nm erhölls en signal vid 632.0 nm och en idler vid 3362 nm. Pumputömningen uppmättes till 30 % och verkningsgraden till 18 %, vilket innebar en röd pulsenergi på 0.07 mJ.

I en kristall efter OPO:n, genomfördes summafrekvensgenerering (SFG) mellan signalen och idlern, vilket gav blått vid 459.3 nm. Dock erhölls endast pulser på 2 μJ vid denna våglängd. För att öka konver-teringsgraden för processen gjordes ett försök att använda ett bulk-braggitter som inkopplingsspegel till den signalresonanta OPO:n. På så sätt erhölls 50 % smalare bandbredd på signalen. Bandbredden på idlern antogs minska med samma andel, varför ett bättre överlapp mellan idlern och acceptansbandbredden på summafrekvensprocessen torde ha erhållits, vilket skulle ha medfört en högre verkningsgrad för konverteringen. Emellertid ökade inte den blå energin.

Strålkvalitén på pumpen vid våglängden 532 nm visade sig dock ha stor betydelse för hur effektiv konverteringsprocessen från pumpen till blått blev; när strålkvalitén ändrades från $M^2 = 6$ till $M^2 = 1.5$, ökade den blå pulsenergin från 2.4 μJ till 5.0 μJ, det vill säga pulsenergin fördubblades då strålkvalitén på pumpen förbättrades.

Acknowledgements

Contents

1   Introduction

The next generation of displays will most probably be based on laser technology. In order to make the laser displays commercially successful, the laser sources must be made power efficient, compact and cheap. The laser beam must also be of high quality. At the date of this work, there are no sources that satisfactory fulfill all these demands simultaneously. It is therefore of great interest to find new solutions that improve the quality and simplicity of the laser sources.

The main goal of this diploma thesis project was to examine concepts of nanosecond-pulsed solid-state red-green-blue (RGB) lasers. The project consisted of two separate parts. In the first part, an actively Q-switched laser source, emitting nanosecond pulses at 1064 nm, was constructed. As Q-switch, an electrooptic modulator based on RTP was used. In the second part of the project, a frequency conversion stage based on nonlinear conversion processes in periodically poled KTP was examined using a 20 Hz Nd:YAG laser.

The obvious final goal for future work is to combine the two parts into a high average power nanosecond-pulsed RGB laser with a pulse repetition frequency around 20 kHz (HDTV). However, before this can be done, the peak power and the average power of the Q-switched laser must be high enough.

1.1   Outline of the thesis

In the remaining part of this introductory chapter, the latest proceedings in the development of laser display technology and solid-state RGB lasers will be presented. It will also be motivated why lasers should be used for display applications.

In chapter 2, some fundamentals of color theory are explained, including the concepts of the CIE color space. The theory is needed in order to be able to determine the fractional power required at each laser wavelength, in order to obtain a visual impression of for instance white.

Chapter 3, 4 and 5 include the theory and experiments regarding the actively Q-switched laser. In chapter 3 the basic theory of electrooptics is presented and the most common electrooptic materials are overviewed. In chapter 4 an evaluation of the electrooptic modulator constructed within this project can be found. The Q-switching experiments, where the electrooooptic modulator was used, are presented in chapter 5.

Chapter 6 and 7 are focusing on frequency conversions. In chapter 6, the most important theory of nonlinear optics is summarized, and in chapter 7, different frequency conversion setups are presented. Chapter 7 includes both results of simulations of the frequency conversion stages, as well as descriptions of practical experiments of one of the setups.

In the last chapter, the most important results are summarized and discussed. In particular the discussion focuses on suggestions for future work.

1.2   General advantages of laser-based projection systems

Using laser light in projection displays has several advantages compared to older standard techniques, like for instance CRT monitors, plasma displays and lamp projectors. The biggest advantage is the large color gamut which can be obtained. Other positive aspects are high contrast ratio and high brightness. It is also possible to obtain nice projection on curved surfaces, due to the large focal depth of the laser beams. The main reason why the laser TV:s have not reached the wide market yet is the high costs of the systems. [1, 2, 3]

1.3   Different types of laser-based projection systems

In general one could say that there are two different types of RGB laser sources commonly used: semiconductor lasers and diode-pumped solid-state lasers. At the moment the semiconductor technique is developing very fast and there are several companies competing, for instance Sony, Mitsubishi, Samsung and OSRAM. The latter company is currently collaborating with Coherent on an optically pumped semiconductor laser (OPSL). Several manufacturers have already presented working prototypes of laser-HDTV (High Definition TV: 1920x1080 pixels) sets. [1, 2, 4, 5, 6]

One company which has come far in the development process is Novalux. They have constructed a high-power surface-emitting diode laser called NECSEL (Novalux Extended Cavity Surface Emitting Laser). Simplified, this laser consists of an infrared InGaAs laser, emitting in the IR, and a nonlinear crystal, PPLN, which is used for frequency doubling of the infrared light into the visible. The design of the laser makes it possible to use it in pulsed mode, with a pulse repetition frequency up to 1 MHz. Novalux claims that the brightness of their laser source is six orders of magnitudes larger than lamps and LED:s, and that the output is speckle free. Furthermore, the lifetime of the laser is said to be 30000 hours, which means that it would not need to be replaced before the TV itself needs to be replaced. At the moment (2007) it seems that Novalux will be able to keep the cost of the devices down; according to the manufacturer, the cost of a laser source emitting 3W at each wavelength, is estimated to be around $70, if the production rate is one million of units per year. [1, 7]

The first laser TV:s will probably be rear-projected (RPTV) systems, using digital light processing (DLP) microchips, originally developed by Texas Instruments. The DLP microchips consist of small mirrors, which can reflect incoming light from the laser source onto the TV display. Each mirror rep-

resents one pixel on the TV, and they can be turned on and off thousands of times per second. Different colors can be obtained by letting each primary sequently illuminate the mirrors under short intervals, and by letting the mirrors be on and off a certain number of times for each color during some illumination cycles. Different amount of powers of each primary will then be reflected onto the screen during this time, and since the sensors of the human eye has a certain integration time, a color sensation is obtained, which depends on the total energy of each primary detected over the integration time. [1, 4]

Compared to lamp based systems, the semiconductor laser based systems need fewer optical and mechanical parts, which decreases the weights and the costs of the systems. Considering the low weight, the small size and the high power efficiency of the semiconductor RGB lasers, it will probably be possible to implement them in for instance mobile phones in the future. Furthermore, Novalux claims that the Necsels can be arranged in arrays to produce high output powers, which is necessary for cinema projectors.[1] However, one should note that at least 10 W per color is needed for such a system.[8]

For low-power systems, like home theaters, the semiconductor technology is the most promising technique. However, for more demanding systems like cinemas, simulators, planetariums etc. solid-state lasers will probably be competitive to semiconductor lasers even in the future. The biggest reason for this is the high beam quality which can be obtained from the solid-state lasers. A company among others, which are manufacturing diode-pumped solid-state RGB lasers, is Jenoptik. With their sophisticated system, a brightness of 1200 lumen of white light can be achieved. However, the system is very expensive, weighs over 400 kg and consumes 3 kW of power. In contrast to semiconductors, the power at each color in this system cannot be adjusted with current. Instead acoustooptical modulators are used. The projection is accomplished by using a two-axis mirror scanner.[9] For a nice review on projection scanning systems, see reference [10].

In order to make solid-state RGB lasers competitive to semiconductor RGB lasers for high power projection systems, they must be made simpler, more efficient and cheaper than they are today. In the next section, the latest proceedings in solid-state RGB lasers will be overviewed.

1.4   Solid-state RGB lasers

A compact way of obtaining red, green and blue emission is to use nonlinear conversion processes in the laser crystal itself. This type of function has been realized by Brenier et al in a $GdAl_3(BO_3)_4$:Nd^{3+} crystal.[11] The transitions $^4F_{3/2} \rightarrow {}^4I_{11/2}$ and $^4F_{3/2} \rightarrow {}^4I_{13/2}$ of the Nd^{3+} ion, gave lasing at 1062 nm and 1338 nm respectively. These two lasing wavelengths were self-frequency doubled in the crystal into green at 532 nm and red at 669 nm. Blue was

3

achieved by self-sum frequency mixing between the pump at 744.7 nm and the radiation at 1338 nm. The difficulty was to obtain phase matching for all three processes at the same time. Brenier showed however, that it was possible to obtain all three colors, even though the birefringent phase matching conditions were not fully fulfilled for the different processes. But, as one could suspect, the output powers were very low; the conversion efficiencies from the input pump power to the red and green powers were below 1 %, and the conversion efficiency from the input pump power to the blue power was much smaller than 1 %.

Capmany [12] studied a similar technique in $LiNbO_3:Nd^{3+}$, but instead of angle phase matching, quasi-phase matching was employed. In order to get close to all the phase matching conditions simultaneously, the crystal was aperiodically poled. However, also in this case the conversion efficiencies from the pump wavelength to the RGB wavelengths were less than 1 %. Hence, this method does not seem to have a future, due to the difficulty of obtaining phase matching for the three different nonlinear processes in the same crystal at the same time.

Brunner et al [13] have demonstrated a very efficient high-power RGB system based on a mode-locked thin-disk Yb:YAG laser emitting 80 W at 1030 nm. The pulse repetition frequency of the Yb:YAG laser was 57 MHz and the pulse length was 705 fs. The following frequency conversion stage included one periodically poled SLT crystal and four LBO crystals. The non-linear processes in the LBO crystals were critically phase matched, which meant that they could be operated at room temperature. A total output power of 24.9 W of white light D65 was produced by the system. Except the high power, other positive aspects of this system were the scalability and the possibility to easily change the red and blue wavelengths. However, it must be mentioned that the system was large and heavy, and in addition the cost of the system was probably very high. Other RGB lasers based on different types of mode locking techniques have for instance been proposed by Henrich et al.[14]

The company Q-Peak has developed a RGB laser source based on an actively q-switched Nd:YLF laser, emitting light at 1047 nm. At a repetition rate of 22 kHz, an average output power of 50 W from the Nd:YLF laser can be achieved. The output from this laser is sent into a frequency conversion stage, which among other components contains a ring cavity OPO. Both critical and noncritical birefringent phase matching techniques in LBO crystals are utilized. The system gives a total output of 14.9 W of white light D65. Even though this system requires less parts than the system described by Brunner, the system is still space demanding. [15]

The urge for small, easy-to-handle, but at the same time powerful RGB lasers, has pushed the development toward new solutions. Gao et al [16] have demonstrated a compact RGB source based on a q-switched Nd:YAG laser, with an average output power of 1 W and a pulse repetition frequency

of 4 kHz. After frequency doubling the output from the laser, the laser beam was injected into an interesting crystal functioning as a singly resonant OPO with intra-cavity sum frequency generation. To obtain such a function, a monolithic periodically poled SLT crystal with two different grating periods was used. The first period generated a signal at 633 nm and an idler at 3342 nm. The idler was then sum frequency mixed with the radiation at 532 nm in the next grating, which gave blue at 459 nm. The sides of the crystal were coated in order to be resonant at the signal wavelength; the incoupling side was coated to be highly reflective at the signal wavelength and the outcoupling side was coated to have a reflectance of 65 % at the signal wavelength. This system gave output powers of 203 mW, 146 mW and 69.4 mW at the red, green and blue wavelengths respectively. A positive aspect of the system is that it is expected to be scalable. A similar approach has also been suggested by Robles-Agudo et al.[17]

Another interesting approach of obtaining the three primaries, is to use one aperiodically poled crystal, instead of different periodically poled crystals. Ren et al [18] have demonstrated a RGB laser, in which an aperiodically poled $LiTaO_3$ crystal was pumped with an acoustooptically q-switched Nd:GdVO$_4$ laser, lasing at both 1063 nm and 1342 nm. After three frequency conversion processes in the crystal, red at 671 nm, green at 532 nm and blue at 447 nm were obtained. When the crystal was pumped with 580 mW at 1063 nm and 1.21 W at 1342 nm, the red, green and blue output powers where 251.5 mW, 193.3 mW and 13.1 mW respectively. However, due to the wavelength choice, the total power after white light balancing was low. Another, very similar setup, has also been reported by the same group, see reference [19].

1.5 Advantages of Q-switched RGB lasers

As mentioned earlier, the system examined in this work is consisting of two separate parts: a laser source emitting light at 1064 nm and a frequency conversion stage producing red, green and blue light from light at 1064 nm. The efficiencies of the nonlinear processes in the frequency conversion stage are dependent on the intensities of the interacting fields: higher intensities give higher conversion. Therefore pulsed laser systems with high peak powers are much more efficient than continuous-wave (CW) based laser systems. Pulsed systems also reduce the speckles, which is a major problem in CW based systems.

RGB laser systems based on mode-locked lasers are in most cases more efficient than systems based on Q-switched lasers. However, mode-locked lasers are more complicated, demands more optics and are larger than Q-switched lasers. Therefore the Q-switching technique has been utilized within this project.

2 Colors and power balancing

One of the big advantages of the laser TV:s is the possibility to obtain better color presentation. In order to understand how this works, the basic anatomy of the human eye will shortly be introduced, after which the concepts of the CIE (International Commission of Illumination) color space will be treated. The CIE color space is a powerful tool to describe the color sensation of the human eye. Based on this diagram, three colors (primaries) will be chosen for the laser in a later chapter. By adjusting the relative ratio of the powers of the three wavelengths in a certain way, white light can be obtained. The procedure how this is done is presented in chapter 2.3.

2.1 The sensors of the human eye

The light sensors of the human eye are situated at the retina - a thin membrane only 0.1 mm thick (see figure 2.1). Two different main types of senors are used: rods and cones. In total there are 130 million of such receptors over the whole retina. In a small area (approximately 5 mm in diameter) called macula, the density of cones is larger, and in the middle of the macula, there is an area 1.5 mm in diameter called fovea, the central part of which only contains cones. [20]

The rods are very light sensitive and are used for dark vision. These photo sensors cannot distinguish between colors, because they all consist of the same photochemical substance (rhodopsin). The cones, on the other hand, are not as light sensitive but can distinguish between colors. This is because they come in three different types, each with its own type of photo active protein, which are sensitive in the blue, green and red region respectively. By stimulating the three types of cones by different power ratios, different colors will be experienced. [21]

To describe the sensitivity of the eye at different wavelengths, the relative visibility curve is often used. This curve is found by first measuring the flux required at different wavelengths in order to get the same brightness sensation over the visible spectrum, and then taking the inverse of these measured values. It is however a well known fact that the central wavelength shifts slightly towards lower wavelengths when the intensity is decreased. This so called Purkinje effect can be an important aspect when choosing wavelengths of the laser TV; depending on whether the screen and the surrounding room is bright or dark, different primaries will optimize the visual effect. In figure 2.2 the two extreme cases of the relative visibility curve have been plotted. [23]

Another important property of the eye to consider when constructing a TV is the temporal resolution, which describes the ability of the eye to discriminate luminous changes in the time domain. An easy experiment to conduct in order to describe this resolution is simply to use a periodically
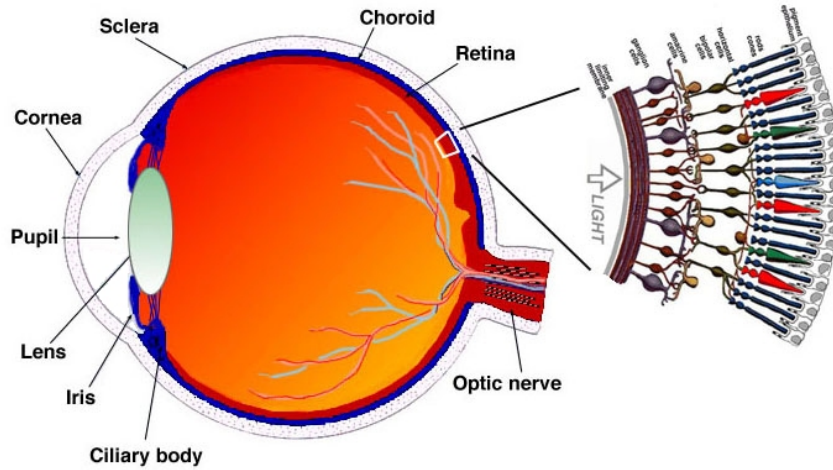
Figure 2.1. *Anatomy of the human eye. The close up figure shows the cones and the rods of the eye. [22]*
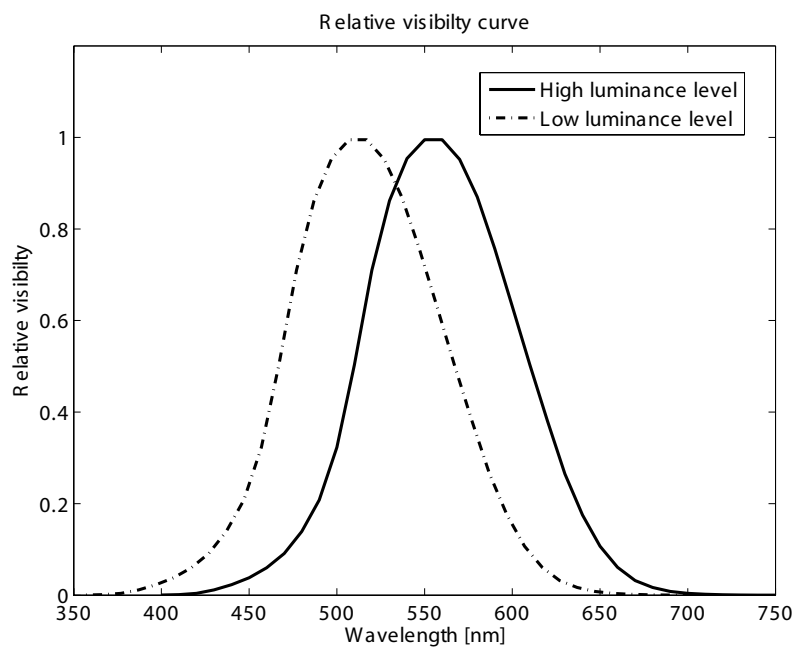
Figure 2.2. *The peak of the relative visibility curve shifts approximately 35 nm between low and high illumination level. Curve data from reference [23].*

flashing light. If the frequency of the light pulses is higher than a certain value called the critical flicker frequency, then the flickering is no longer visible. This effect is dependent both on the size and the intensity of the object, where the latter dependency is described by the so called Ferry-Porter law:

$$CFF = a \log L + b \qquad (2.1)$$

Here L is the luminance of the flickering object, and a as well as b are just constants. This model is valid in a broad retinal luminous interval ranging from 0.5 Td (Trolands) to 10^4 Td. Beyond the upper limit, the curve flattens out and the critical flicker frequency decreases. From measurements, the maximum critical flicker frequency is found to be around 45 Hz, explaining why TV monitors do not give a flickering sensation for most people. [22]

The temporal resolution is based on the integration times of the detectors of the eye. In order to be able to separate two light pulses, these need to be separated by a time interval larger than the integration time. The characteristic integration term is approximately 10 to 15 ms for cones and 100 ms for rods. Hence bright flashes are easier to discriminate than flashes with lower luminous levels. [22]

In the case of laser-TV design, the temporal resolution is of no big deal since the standards of the frame update frequency are 50 Hz and 100 Hz, and they are therefore higher than the maximum critical flicker frequency. Nevertheless, it is interesting and important to understand this fundamental phenomena.

2.2   CIE color space

The relative visibility curve (figure 2.2) describes the overall sensitivity of all of the sensors together. In order to be able to describe the sensitivity of the different cones, another experiment need to be done: the color matching experiment. This experiment is based on three test light sources, normally red, green and blue, and one reference source. If the spectra of the test sources are denoted by **R**, **G** and **B** respectively, and their weight factors by R, G and B, then the total color impression can be described by $\mathbf{C} = R\mathbf{R} + G\mathbf{G} + B\mathbf{B}$. In the CIE color system from 1931 the test sources, or the so called primaries, are monochromatic sources with the wavelengths 700 nm, 546.1 nm and 435.8 nm respectively. [24]

The idea with the color matching experiment is now to match the color **C** to an arbitrary reference source **D** by adjusting the weight factors R, G and B. In order to obtain matching for some colors **D**, it is necessary to combine one of the light sources **R**, **G** or **B** with the reference source **D**. Mathematically this is denoted by a negative weight of the light source moved. [24]

(a) *RGB color matching functions.*

(b) *XYZ color matching functions.*
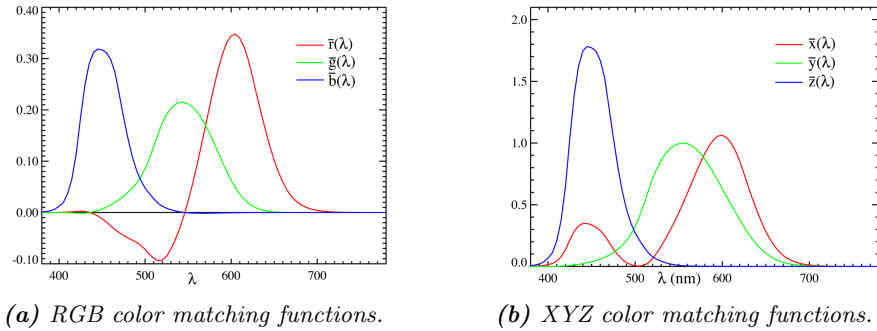
Figure 2.3. *Plot of the color matching functions in the RGB and XYZ color spaces respectively. Note that the weight factors can be negative in the RGB color space, in contrast to the weight factors in the the XYZ color space, which are always positive.[21]*

If this experiment is carried through by tuning the wavelength of the reference source over the whole visible spectrum, the normalized weight factors $\bar{r}(\lambda)$, $\bar{g}(\lambda)$ and $\bar{b}(\lambda)$ can be determined. These weight factors are called CIE 1931 color matching functions and they are visualized in figure 2.3(a). [21, 24]

The weight factors makes it is possible to calculate the RGB colors for an arbitrary spectrum $P(\lambda)$ as follows:

$$R = k \int P(\lambda)\, \bar{r}(\lambda)\, \mathrm{d}\lambda \tag{2.2}$$

$$G = k \int P(\lambda)\, \bar{g}(\lambda)\, \mathrm{d}\lambda \tag{2.3}$$

$$B = k \int P(\lambda)\, \bar{b}(\lambda)\, \mathrm{d}\lambda \tag{2.4}$$

where k is just a normalization constant.

It is often convenient to transform the RGB coordinate system into a new coordinate system XYZ, so that all coordinates become positive. If we denote the transformation matrix by $\mathbf{C}_{xr}$, the transformation is simply given by $\mathbf{X} = \mathbf{C}_{xr}\mathbf{R}$. In the same way also the RGB color matching functions $\bar{r}(\lambda)$, $\bar{g}(\lambda)$ and $\bar{b}(\lambda)$ can be transferred into the XYZ color space, giving the XYZ color matching functions $\bar{x}(\lambda)$, $\bar{y}(\lambda)$ and $\bar{z}(\lambda)$. These are plotted in figure 2.3(b). For an arbitrary spectral power distribution $P(\lambda)$, the XYZ coordinates are now given by: [24]

$$X = k \int P(\lambda)\, \bar{x}(\lambda)\, \mathrm{d}\lambda \qquad (2.5)$$

$$Y = k \int P(\lambda)\, \bar{y}(\lambda)\, \mathrm{d}\lambda \qquad (2.6)$$

$$Z = k \int P(\lambda)\, \bar{z}(\lambda)\, \mathrm{d}\lambda \qquad (2.7)$$

In order to get a quantity which is independent of the luminance (or brightness), the following normalization can be performed:

$$x = \frac{X}{X + Y + Z} \qquad (2.8)$$

$$y = \frac{Y}{X + Y + Z} \qquad (2.9)$$

$$z = \frac{Z}{X + Y + Z} \qquad (2.10)$$

Here x, y and z are called the chromaticity values and they only depend on hue and saturation. In the xyz-space, the chromaticity values span the triangular plane $x + y + z = 1$. If this plane is projected onto the xy-plane, the famous xyY chromaticity diagram is obtained, see figure 2.4. From this diagram, it is always possible to calculate the XYZ coordinates if one of the luminances X, Y or Z is given. [24]

In simplicity the chromaticity diagram describes the human gamut, i.e. the chromaticities which a person can see. Normal visualization systems like printers, projectors, monitors, TV-screens etc. can only partly cover the human gamut. Standard projectors, for instance, can only cover the chromaticities inside the black triangle sketched in figure 2.4. However, with a laser-TV it is possible to obtain a much larger chromaticity span, because the primaries are monochromats situated at the outer border of the chromaticity diagram. Hence, with a laser-TV it would be possible to represent colors in a better way than normal monitors can. Normally three primaries are used, but one could equally well use an arbitrary amount of primaries. [25, 10]

2.3 Power balancing

With three primaries, a large amount of chromaticities can be reached by scaling the power distributions of the primaries. In the case of lasers, the relative ratios between the powers required for a certain chromaticity are easily calculated. This is because the spectral power distributions $P(\lambda)$ approaches delta functions when the bandwidths of the primaries becomes shorter and shorter. Assume that the wavelengths of the primaries are λ_1, λ_2 and λ_3. Then equations 2.5 - 2.7 approaches:
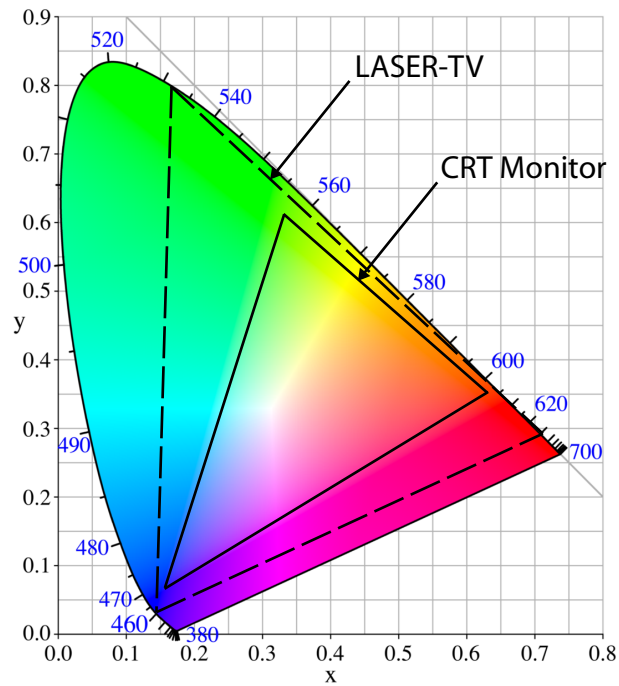
Figure 2.4. *The CIE 1931 xyY chromaticity diagram. The solid triangle represents the chromaticity span of a regular computer monitor, and the dashed triangle represents the chromaticity span of a laser-TV with the primaries* $\lambda = 458$ *nm,* $\lambda = 532$ *nm and* $\lambda = 630$ *nm. It is important to realize that the colors shown in the diagram are only representative, not true, since printers can only cover a part of the chromaticity diagram. The same holds also for other viewing media, like for instance computer monitors.[21]*

$$\begin{bmatrix} X \\ Y \\ Z \end{bmatrix} = k \begin{bmatrix} \bar{x}(\lambda_1) & \bar{x}(\lambda_2) & \bar{x}(\lambda_3) \\ \bar{y}(\lambda_1) & \bar{y}(\lambda_2) & \bar{y}(\lambda_3) \\ \bar{z}(\lambda_1) & \bar{z}(\lambda_2) & \bar{z}(\lambda_3) \end{bmatrix} \begin{bmatrix} P(\lambda_1) \\ P(\lambda_2) \\ P(\lambda_3) \end{bmatrix} \qquad (2.11)$$

Now if X, Y and Z as well as the color matching functions are known, then the relative power ratios can be calculated by multiplying both sides of the above matrix equation with the inverse matrix. The result is as follows:

$$\begin{bmatrix} \bar{x}(\lambda_1) & \bar{x}(\lambda_2) & \bar{x}(\lambda_3) \\ \bar{y}(\lambda_1) & \bar{y}(\lambda_2) & \bar{y}(\lambda_3) \\ \bar{z}(\lambda_1) & \bar{z}(\lambda_2) & \bar{z}(\lambda_3) \end{bmatrix}^{-1} \begin{bmatrix} X \\ Y \\ Z \end{bmatrix} = k \begin{bmatrix} P(\lambda_1) \\ P(\lambda_2) \\ P(\lambda_3) \end{bmatrix} \qquad (2.12)$$

This important result will be used in section 7.2, when the RGB laser is white balanced. White light is often defined as the chromaticity obtained when the spectral power is constant over the whole visible spectrum.[26] However, it is not necessary to have this special spectral power distribution in order to obtain white light, because with two or more appropriately chosen primaries it is possible to balance the powers to reach white balance. If one wants to complicate things a little bit, there are not just one white point in the chromaticity diagram, but rather a whole series representing different color temperatures of the Planck radiation.[24] For instance, for a color temperature of 6500 K (daylight), denoted D65, the XYZ coordinates could be $X = 95.017$, $Y = 100.000$ and $Z = 108.813$.[27],[28] Values of the color matching functions are tabulated in special color books, like in Wyszecki on pages 725-747.

3 Electrooptics

The actively Q-switched laser constructed, which will be described thoroughly in chapter 5, contains an electrooptic modulator. In order to understand the function of this modulator, basic knowledge of the electrooptic effect is needed. Therefore, the fundamental theory of electrooptics is going to be presented in this section. Furthermore the crystal used in our setup will be examined as well as the pulse generator needed for the electrooptic amplitude modulation.

3.1 Theory of the electrooptic effect

An electric field $\mathbf{E}$ applied to a medium interacts with the positive and negative particles in the medium leading to a change in the distribution of charges on molecular level. The change of charge distribution results in an electric dipole moment $\boldsymbol{\mu}$, causing a change in the inner electric field.[29] The total dipole moment on the macroscopic level is described by the polarization $\mathbf{P}$ and is simply the sum of the dipole moments on the microscopic level:

$$\mathbf{P} = \frac{1}{V} \sum_{n=1}^{N} \boldsymbol{\mu}_n \tag{3.1}$$

This expression can be simplified by introducing the parameter N_V, representing the number of dipole moments per unit volume:

$$\mathbf{P} = N_V \langle \boldsymbol{\mu}_n \rangle \tag{3.2}$$

where $\langle \boldsymbol{\mu}_n \rangle$ is the average dipole moment.[30]

The mechanisms behind the generation of the dipole moments depend on the medium. In a liquid consisting of anisotropic molecules, a dipole vector is generated when an electric field is applied, because the molecules are rotated into a preferred direction relative to the field. In a liquid consisting of isotropic molecules, on the other hand, a dipole vector is generated when a electric field is applied, because the molecules and the electron clouds around them are deformed. Crystals are different to liquids because in crystals the molecules are fixed in their lattice positions and can not be rotated. Therefore a change in the dipole moments occurs only because the field displaces the electron cloud from the nucleus a little bit. More correctly, the field causes a relative change between the electrons and the nucleus, but since the mass of the electrons are much smaller than the mass of the nucleus, the displacement of the nucleus can in most cases be neglected.[30]

All these mechanisms can lead to changes in the refractive indices depending on how the electric field is applied. *In general, the phenomena of*

an electric field causing a refractive index change is called the electrooptic effect. The electrooptic effect can also be found in glasses and gases. However, in the latter case the effect is very small compared to the effect in liquids and crystals.[30] In our case we are interested in the electrooptic effect in crystals. Hence, this will be treated more in depth in the following sections.

3.1.1 Mathematical description of anisotropic crystals

For convenience one usually introduce the displacement vector $\mathbf{D}$ in order to describe the electric field and polarization. The displacement vector is defined as follows:

$$\mathbf{D} = \varepsilon_0 \, \mathbf{E} + \mathbf{P} \tag{3.3}$$

where ε_0 is the electric permittivity in vacuum. A direct relation between the displacement vector and the electric field, can be obtained by introducing the electric permittivity constant ε:

$$\mathbf{D} = \varepsilon_0 \, \varepsilon \, \mathbf{E} \tag{3.4}$$

For isotropic crystals, $\mathbf{D}$ and $\mathbf{E}$ are parallel, which means that ε in these cases must be a scalar quantity. However, for anisotropic crystals, $\mathbf{D}$ and $\mathbf{E}$ are not necessary parallel, which means that ε in general must be described by a tensor of second order. It will later on be very obvious that the tensor description is very effective in describing anisotropic crystals.

On component form, equation 3.4 becomes

$$D_i = \varepsilon_0 \, \varepsilon_{ij} \, E_j \tag{3.5}$$

This expression can be rewritten as

$$E_i = (\varepsilon_0 \, \varepsilon_{ij})^{-1} \, D_j \tag{3.6}$$

Now the energy density of an electric field $\mathbf{E}$ in a medium is proportional to the quantity $Q = \mathbf{E} \cdot \mathbf{D}$, or $Q = E_i \cdot D_i$ on component form. Using equation 3.6, the energy density can be expressed as

$$Q(\mathbf{D}) = (\varepsilon_0 \, \varepsilon_{ij})^{-1} \, D_i \, D_j \tag{3.7}$$

Since this expression is always larger than zero (i.e. since the quadratic form is positive definite) it can be visualized as an ellipsoid - the indicatrix [30]:

$$1 = \varepsilon_{ij}^{-1} \, x_i \, x_j \tag{3.8}$$

By letting x_1, x_2 and x_3 be parallell to the principal axes of the crystal (i.e. the optic main axes), then the above equation can be written as:

$$1 = \frac{1}{\varepsilon_{11}} x_1^2 + \frac{1}{\varepsilon_{22}} x_2^2 + \frac{1}{\varepsilon_{33}} x_3^2 \tag{3.9}$$

Here we make use of the relation $\varepsilon_{ii} = n_i^2$:

$$1 = \frac{1}{n_1^2} x_1^2 + \frac{1}{n_2^2} x_2^2 + \frac{1}{n_3^2} x_3^2 \tag{3.10}$$

Let us denote the propagation direction of the phase fronts with $\hat{\mathbf{k}}$. One can now show that if this vector is put in the same system as the indicatrix, then the main axes of the intersection of the normal plane of the $\hat{\mathbf{k}}$-vector and the indicatrix determines the refractive indices of the two corresponding linearly independent field components of the plane wave propagating in the direction of $\hat{\mathbf{k}}$, see figure 3.1.[31] If the intersection is circular, the direction of $\hat{\mathbf{k}}$ is called an optic axis. In this direction, the refractive index is the same independently of the polarization of the incident light. Depending on the number of unequal elements n_i, the number of optic axes varies; there are three different crystal classes depending on the the number of optic axes. If all n_i are equal, the crystal is called optically isotropic, i.e. all axes are 'optic axes'. If two of the elements are equal, the crystal is called optic uniaxial, because there is only one optic axis. Finally, if all elements are unequal the crystal is called optic biaxial, because there are two optic axes.[30] It is important to note that the optic axes are *not* the same as the optic main axes!

3.1.2 Mathematical description of the electrooptic effect

Using the tensor description introduced earlier, the electrooptic effect can be described as

$$\Delta \left(\frac{1}{\varepsilon} \right)_{ij} = r_{ijk} E_k + R_{ijkl} E_k E_l + \dots \tag{3.11}$$

where r_{ijk} is the linear electrooptic coefficient and R_{ijkl} is the quadratic electrooptic coefficient. The first order effect is called the Pockel's effect and the second order effect is called the Kerr effect. Higher order terms are in most cases neglected and from hereon we will not consider them.

$$\Delta \left(\frac{1}{\varepsilon} \right)_{ij} = r_{ijk} E_k + R_{ijkl} E_k E_l \tag{3.12}$$

There is now a logical connection to the indicatrix presented in the prior chapter. By application of an electric field on the crystal, the tensor $\Delta \left(\varepsilon^{-1} \right)_{ij}$ will describe the rotations and the deformations of the indicatrix. Hence, if we know the tensors r_{ijk} and R_{ijkl} we can fully describe the new refractive index properties of the crystal.
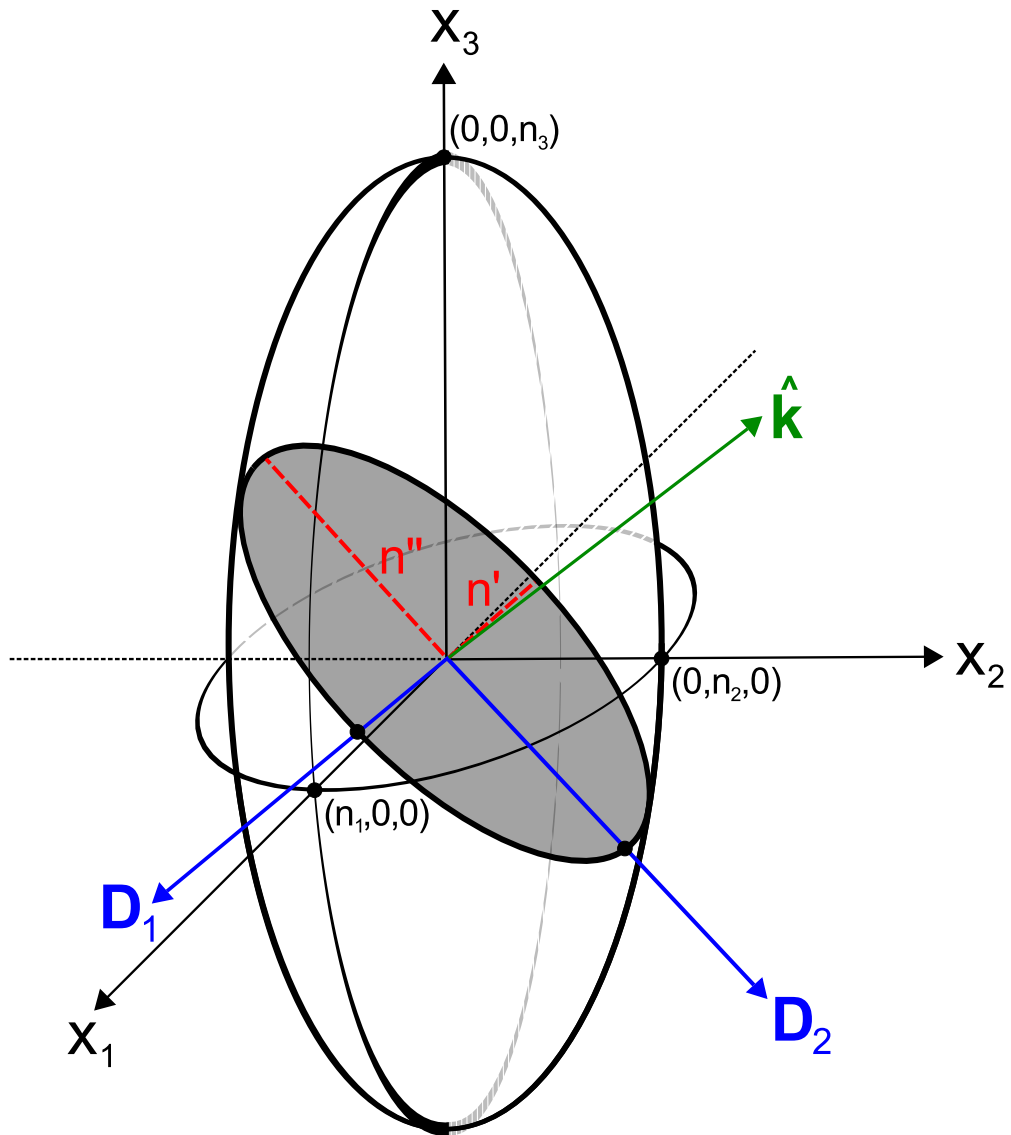
Figure 3.1. *Visualization of the index ellipsoid. The vector $\hat{\mathbf{k}}$ describes the propagation direction through the crystal. The gray filled ellipse marks the intersection between the normal plane of $\hat{\mathbf{k}}$ and the index ellipsoid. Half the lengths of the main axes of this ellipse determine the refractive indices n' and n'' of the two perpendicular plane wave field components of the wave propagating in the direction of $\hat{\mathbf{k}}$.*

3.1.3 Crystal symmetries and element presentation

The Kerr effect is neglectable in the electrooptic modulator used in the Q-switched laser, which means that it is only necessary to examine the linear terms in equation 3.12:

$$\Delta \left(\frac{1}{\varepsilon} \right)_{ij} \cong r_{ijk} \, E_k \qquad (3.13)$$

Since the permittivity tensor is symmetric, the linear electrooptic tensor must also be symmetric in its first two indices, i.e. $r_{ijk} = r_{jik}$. The symmetry reduces the number of independent elements from $3 \cdot 3 \cdot 3 = 27$ to $6 \cdot 3 = 18$ elements. To present the coefficients it is therefore convenient to use a reduced form of the linear electrooptic tensor, so that only the independent elements has to be written out. The reduced form uses the symmetry relations $ij = m$ and $ji = m$ in r_{ijk}, generating the reduced 'tensor' r_{mk}, see table 3.1. Please note that this reduced form of the tensor does *not* transform as a tensor.[30]

Elements	Reduced form
11	1
22	2
33	3
23,32	4
13,31	5
12,21	6

Table 3.1. *Connection between elements and their reduced forms.*

For many crystals, some of the elements are zero and some of the elements are equal. In order to obtain this useful information, one must first find out which *point symmetry group* the crystal belongs to. A point symmetry group defines a set of operations that can be applied to the crystal, for which the structure of the crystal is identical before and after the application of the operation with respect to a fixed reference frame. There are three main operations that can be applied: rotation, inversion and rotational inversion.

In the international system, the rotational operation is labeled with an integer n, which specifies the angle of rotation as $\theta = 2\pi/n$. Only 5 integers are allowed from a geometric point of view: 1, 2, 3, 4 and 6. The next operation, the inversion operation, is denoted by $\bar{1}$ and performs an inversion with respect to the origin. Finally, the rotational inversion describes a mixture of the two operations defined above: first a rotation and then an inversion. Possible operations are denoted by $\bar{1}$, $\bar{2}$, $\bar{3}$, $\bar{4}$ and $\bar{6}$. The second of these operations, $\bar{2}$, is often denoted by m, because it acts as a mirror.[30]
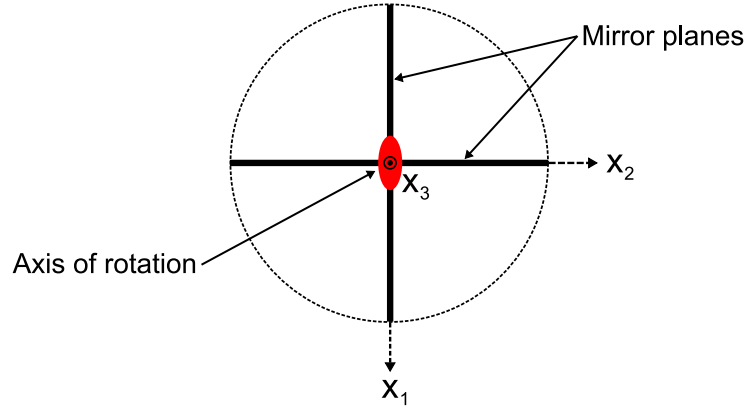
Figure 3.2. *Symmetries of point group mm2. The bold black lines mark the mirror planes and the oval describes the 2-fold rotational symmetry.*

From geometry considerations it is possible to find 32 different crystal classes. These can be grouped in 7 different crystal systems: triclinic, monoclinic, orthorhombic, tetragonal, cubic, trigonal and hexagonal. For a thoroughly description of these systems, see for instance reference [32].

Knowing the point symmetry group of a crystal, one can make use of a very important principle called the Neumann's principle. It states that the material tensors should be invariant with respect to the symmetry operations of the point group of the crystal. The best way to understand how this principle can be used in order to examine the elements of the linear electrooptic tensor is to read through an example. Therefore an example is presented in the next section.

3.1.4 Calculation of constraints on the linear electrooptic tensor for the mm2 point group

In order to understand the response on the refractive index of a specific crystal when applying an electric field **E**, it is important to examine the symmetric constraints which can be put on the crystal. The electrooptic modulator used in the experiments described in the next chapter was based on an RTP crystal, belonging to the point group mm2. The symmetries of this point group can be described as in figure 3.2.

The first sign 'm' describing the point group defines a mirror operation in the xz-plane (if the axes convention defined in Nye [32] is used). The transformation matrix for this operation is:

$$a_{ij} = \begin{pmatrix} 1 & 0 & 0 \\ 0 & -1 & 0 \\ 0 & 0 & 1 \end{pmatrix} \qquad (3.14)$$

The transformation of the linear electrooptic coefficients r_{ijk} using the matrix above can be written as

$$r'_{lmn} = a_{li}\, a_{mj}\, a_{nk}\, r_{ijk} \tag{3.15}$$

By noting that the transformation matrix is diagonal, equation 3.15 simplifies to:

$$r'_{ijk} = a_{ii}\, a_{jj}\, a_{kk}\, r_{ijk} \tag{3.16}$$

Now Neumann's principle states that the linear electrooptic coefficient should be identical before and after the transformation, i.e. the following must be valid:

$$r_{ijk} = a_{ii}\, a_{jj}\, a_{kk}\, r_{ijk} \tag{3.17}$$

Considering the transformation 3.14 and the equation 3.17, it is obvious that all terms containing an odd multiple of the element a_{22} must be zero. For the other terms, no information is given. If the zero elements are denoted by $\cdot$, these elements can nicely be presented using the reduced tensor form:

$$r_{ij} = \begin{pmatrix} & \cdot & \\ & \cdot & \\ & \cdot & \\ \cdot & & \cdot \\ & \cdot & \\ \cdot & & \cdot \end{pmatrix} \tag{3.18}$$

The second mirror, describing the point symmetry group mm2, represents mirroring in the yz-plane. The transformation matrix for this operation is:

$$a_{ij} = \begin{pmatrix} -1 & 0 & 0 \\ 0 & 1 & 0 \\ 0 & 0 & 1 \end{pmatrix} \tag{3.19}$$

Of course equation 3.17 is also valid for this transformation. Thus, all terms containing odd multiples of the element a_{11} must be zero:

$$r_{ij} = \begin{pmatrix} \cdot & & \\ \cdot & & \\ \cdot & & \\ \cdot & & \\ & \cdot & \cdot \\ & \cdot & \cdot \end{pmatrix} \tag{3.20}$$

The last operation describing the point symmetry group mm2 is '2', i.e. rotation around the z-axis with π radians. As earlier, it is a good idea to start writing down the transformation matrix a_{ij}:

$$a_{ij} = \begin{pmatrix} -1 & 0 & 0 \\ 0 & -1 & 0 \\ 0 & 0 & 1 \end{pmatrix} \qquad (3.21)$$

Again equation 3.21 is valid. Considering the above transformation matrix, all terms containing odd multiples of the elements a_{11} and a_{22} must be zero:

$$r_{ij} = \begin{pmatrix} \cdot & \cdot \\ \cdot & \cdot \\ & \cdot & \cdot \\ & & \cdot \\ & & \cdot \\ \cdot & \cdot \end{pmatrix} \qquad (3.22)$$

Finally, the combination of the tensor descriptions 3.18, 3.20 and 3.22 gives the resultant constraints from the point group symmetries on the linear electrooptic tensor:

$$r_{ij} = \begin{pmatrix} \cdot & \cdot & \bullet \\ \cdot & \cdot & \bullet \\ \cdot & \cdot & \bullet \\ \cdot & \bullet & \cdot \\ \bullet & \cdot & \cdot \\ \cdot & \cdot & \cdot \end{pmatrix} \qquad (3.23)$$

Here $\bullet$ denotes the elements on which no constraints could be put. Some of the non-zero elements of the RTP crystals used in the experiments described in the next chapter have been measured by the manufacturer.[33] Unfortunately these coefficients are only specified for 532 nm, and not for 1064 nm, which is the laser wavelength which will be used in the experiments. However, other manufacturers specifies the coeffients for 1064 nm, see below. [34],[35]

$$r_{ij} = \begin{pmatrix} \cdot & \cdot & 10.6 \\ \cdot & \cdot & 12.5 \\ \cdot & \cdot & 35.0 \\ \cdot & \bullet & \cdot \\ \bullet & \cdot & \cdot \\ \cdot & \cdot & \cdot \end{pmatrix} \quad [\mathrm{pm/V}] \qquad (3.24)$$

The interested reader who wants to know which constraints which can be put on other point groups than mm2, can find a nice overviewable table of reduced tensors in Yariv [31].

3.1.5 Piezoelectric ringing

Equation 3.13 is based on a very simplified model, because depending on the frequency of the applied electric field there are also other indirect contributions from the electric field that cause changes in the refractive index. One of these contributions comes from the (inverse) piezoelectric effect, which describes the strain on the crystal induced by the applied field. Mathematically the piezoelectric effect can be described by:

$$s_{kl} = d_{mkl}\, E_m \tag{3.25}$$

where s_{mn} is the induced strain and d_{kmn} is the coefficients connecting the strain with the electrical field E_k. The link between the refractive index change and the piezoelectric effect is given by the elastooptic effect:

$$\Delta \left(\frac{1}{\varepsilon} \right)_{ij} = p_{ijkl}\, s_{kl} \tag{3.26}$$

where p_{ijkl} is the elastooptic tensor. Inserting equation 3.25 into the above equation gives the following result:

$$\Delta \left(\frac{1}{\varepsilon} \right)_{ij} = p_{ijkl}\, d_{mkl}\, E_m \tag{3.27}$$

Further on, combining this equation with equation 3.13 gives a formula for the total refractive index change:

$$\Delta \left(\frac{1}{\varepsilon} \right)_{ij} = r^S_{ijm}\, E_m + p_{ijkl}\, d_{mkl}\, E_m = \underbrace{(r^S_{ijm} + p_{ijkl}\, d_{mkl})}_{r^T_{ijm}}\, E_m \tag{3.28}$$

Here r^S_{ijm} denotes the constant strain coefficients, or the so called clamped tensor, and r^T_{ijm} denotes the constant stress coefficients, or the so called unclamped tensor. In an electrooptic modulator it is important to avoid using frequencies of the electric field near the acoustic resonance frequencies of the crystal, because at those frequencies the optical field will beat with the frequency of the acoustic waves, something called *piezoelectric ringing*. One easily realizes that the acoustic resonances are dependent on the material and the thickness of the crystal.[30, 36]

At higher frequencies the molecules can no longer vibrate to the applied electrical field, because the vibration energy of the molecules would be too large. The electrooptic coefficients then become approximately equal to the clamped coefficients.[36]
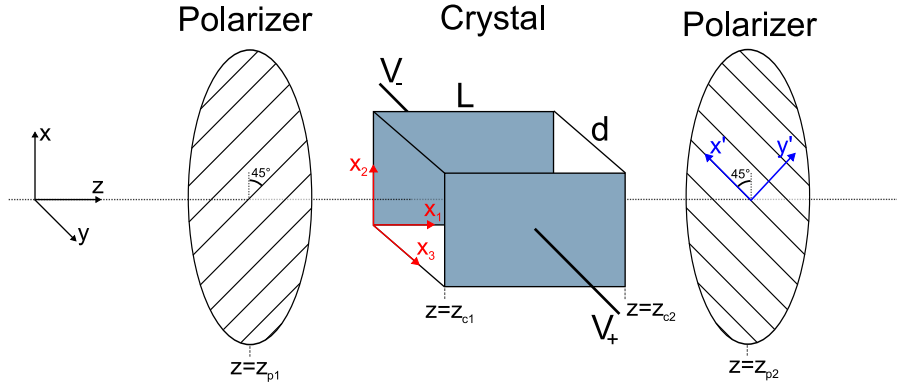
Figure 3.3. *Electrooptic amplitude modulation setup using two polarizers. By changing the voltage it is possible to tune the transmission between $0\,\%$ and $100\,\%$.*

3.2 Electrooptic amplitude modulation

The electrooptic effect in crystals can be used to modulate the phase, the polarization state and the amplitude of light by using different combinations of crystal orientations, crystal lengths and polarizers. In this chapter two amplitude modulation setups are going to be presented, starting with the configuration illustrated in figure 3.3. This is the most common and easiest understood setup: If the crystal introduces a phase shift difference of $\Delta\varphi = \pi$ radians, the outgoing light polarization will be $90°$ shifted to the incoming light and all of the incoming light will be transmitted. On the other hand, if the crystal does not introduce a phase shift, i.e. $\Delta\varphi = 0$, then the transmission through the crystal will be zero. Hence, by choosing the orientation of the crystal appropriately and by applying an electric field over it, the transmission through the modulator can be set between 0 and $100\,\%$.[30, 31]

The mathematical description of the amplitude modulator is rather straightforward. A good start is to write down the complex representation of the electrical field between the first polarizer and the crystal:

$$\mathbf{E_0}(z,t) = \frac{|E_0|}{\sqrt{2}}\, e^{i(wt-kz)}\, \hat{\mathbf{x}} + \frac{|E_0|}{\sqrt{2}}\, e^{i(wt-kz)}\, \hat{\mathbf{y}}, \quad z_{p1} < z < z_{c1} \qquad (3.29)$$

For further treatment, the propagation factor $\exp\left(i(wt-kx)\right)$ can be left out, because here only the polarization state is of interest. However, whenever this factor becomes important again, it can just be hooked on to the polarization factor again. This is analogous to using Jones vectors.[29]

$$\mathbf{E_0} = \frac{|E_0|}{\sqrt{2}}\, \hat{\mathbf{x}} + \frac{|E_0|}{\sqrt{2}}\, \hat{\mathbf{y}}, \quad z_{p1} < z < z_{c1} \qquad (3.30)$$

The propagation through the crystal introduces different phase shifts for the x- and y-components of the electrical field:

$$\mathbf{E_1} = \frac{|E_0|}{\sqrt{2}}\, e^{i\varphi_x}\, \hat{\mathbf{x}} + \frac{|E_0|}{\sqrt{2}}\, e^{i\varphi_y}\, \hat{\mathbf{y}}, \quad z_{c2} < z < z_{p2} \tag{3.31}$$

The polarizer transmits only the electric field components parallel to the polarization direction of the polarizer. To simplify a bit a new coordinate system is used, with its $\hat{\mathbf{x}}$-axis parallel to the polarization direction. In this coordinate system, the outgoing electric field from the modulator becomes:

$$\mathbf{E_2} = \frac{|E_0|}{\sqrt{2}}\, e^{i\varphi_x} \underbrace{\cos 45^\circ}_{= \frac{1}{\sqrt{2}}} \hat{\mathbf{x}}' - \frac{|E_0|}{\sqrt{2}}\, e^{i\varphi_y} \underbrace{\cos 45^\circ}_{= \frac{1}{\sqrt{2}}} \hat{\mathbf{x}}' \tag{3.32}$$

Or more simplified:

$$\mathbf{E_2} = \frac{|E_0|}{2}\, e^{i\varphi_x}\, \hat{\mathbf{x}}' - \frac{|E_0|}{2}\, e^{i\varphi_y}\, \hat{\mathbf{x}}' = |E_0|\, \frac{e^{i\varphi_x} - e^{i\varphi_y}}{2}\, \hat{\mathbf{x}}' \tag{3.33}$$

The intensity after the modulator is proportional to $\mathbf{E_2} \cdot \mathbf{E_2^*}$, which explicitly can be expressed as:

$$I_2 \propto |E_0|^2\, \frac{e^{i\varphi_x} - e^{i\varphi_y}}{2} \cdot \frac{e^{-i\varphi_x} - e^{-i\varphi_y}}{2} \tag{3.34}$$

After conducting the multiplication and simplifying further one obtains:

$$I_2 \propto |E_0|^2 \cdot \underbrace{\left(\frac{1 - \cos(\varphi_x - \varphi_y)}{2} \right)}_{\sin^2\left(\frac{\varphi_x - \varphi_y}{2}\right)} \tag{3.35}$$

Notice that $|E_0|^2$ is proportional to the incoming electric field before the crystal. Using this, one finally arrives at the following elegant expression for the transmission:

$$T_{transmission} = \sin^2\left(\frac{\Delta\varphi}{2}\right) \tag{3.36}$$

where $\Delta\varphi = \varphi_x - \varphi_y$ is the relative phase difference between the wave components after the crystal. When no voltage is applied over the crystal, the phase shift of the i-component of the wave, over a distance Δz, is simply given by:

$$\varphi_i = k\, \Delta z = \frac{2\pi\, n_i\, \Delta z}{\lambda} \tag{3.37}$$

If the length of the crystal is L, then the relative phase difference between the two orthogonal components of the wave becomes:

$$\Delta\varphi = \frac{2\pi}{\lambda}\left(n_x - n_y\right)L \tag{3.38}$$

When an electric field is applied over the crystal, the relative phase difference changes, because according to formula 3.13 there will be a change in the refractive index. In order to use as low voltage as possible, one should try to configurate the setup so that the largest electrooptic coefficient is exploited.[33] For the RTP crystal for instance, this would mean to make use of the r_{23} and r_{33} constants:

$$\Delta\left(\frac{1}{n_2^2}\right) = r_{23}\,E_3 \quad \text{and} \quad \Delta\left(\frac{1}{n_3^2}\right) = r_{33}\,E_3 \tag{3.39}$$

where the reduced tensor form were used. Differentiation of the left hand side of equation 3.39 gives:

$$-\frac{2}{n_2^3}\,\Delta n_2 = r_{23}\,E_3 \;\Rightarrow\; \Delta n_2 = -\frac{n_2^3}{2}\,r_{23}\,E_3 \tag{3.40}$$

$$-\frac{2}{n_3^3}\,\Delta n_3 = r_{33}\,E_3 \;\Rightarrow\; \Delta n_3 = -\frac{n_3^3}{2}\,r_{33}\,E_3 \tag{3.41}$$

If the coordinate axes of the xyz-system is chosen to coincide with the axes 2, 3 and 1 of the crystal in given order, then the phase shift introduced by the crystal, with an electric field applied, changes to:

$$\Delta\varphi = \frac{2\pi}{\lambda}\left(n_x - \frac{n_2^3}{2}\,r_{23}\,E_3 - \left(n_y - \frac{n_3^3}{2}\,r_{33}\,E_3\right)\right)L \tag{3.42}$$

Separation of the birefringent and the electrooptic terms in the above equation gives:

$$\Delta\varphi = \underbrace{\frac{2\pi}{\lambda}\left(n_x - n_y\right)L}_{\Delta\varphi_{birefringent}} + \underbrace{\frac{\pi\,n_3^3}{\lambda}\left(r_{33} - \left(\frac{n_2}{n_3}\right)^3 r_{23}\right)E_3\,L}_{\Delta\varphi_{electro-optic}} \tag{3.43}$$

Often it is convenient to rewrite the electrooptic term as follows:

$$\Delta\varphi_{electro-optic} = \frac{\pi n_3^3}{\lambda}\underbrace{\left(r_{33} - \left(\frac{n_2}{n_3}\right)^3 r_{23}\right)}_{r_c}E_3\,L = \frac{\pi\,n_3^3\,r_c}{\lambda}E_3\,L \tag{3.44}$$

where r_c is called the effective electrooptic coefficient. If d is the thickness of the crystal and V the voltage over crystal, then equation 3.44 can be expressed as:
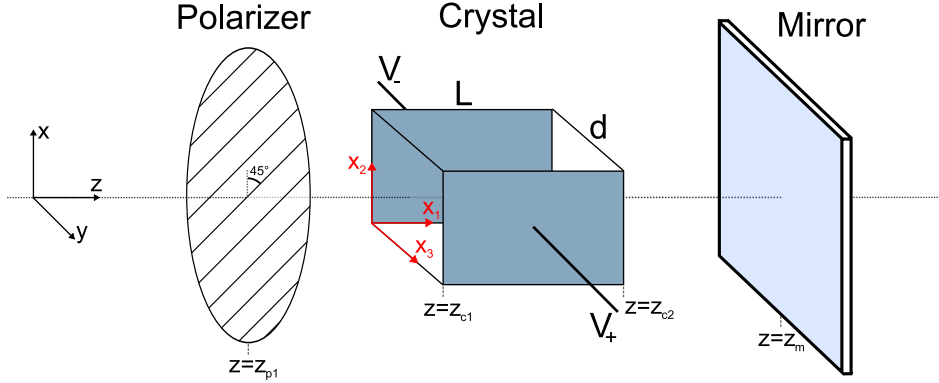
Figure 3.4. *Electro-optic amplitude modulation setup using one polarizer and one mirror.*

$$\Delta\varphi_{electro-optic} = \frac{\pi \, n_3^3 \, r_c}{\lambda} \frac{V}{d} \, L \qquad (3.45)$$

The voltage needed to achieve a phase difference of π radians, the so called half-wave voltage, is given by:

$$V_\pi = \frac{\lambda}{n_3^3 \, r_c} \frac{d}{L} \qquad (3.46)$$

It is important to note that the birefringent part of equation 3.43 also contributes to the total phase shift difference. This means that there in general will be a biased transmission through the modulator. By applying a bias voltage, inserting a wave plate between the polarizers or using a two crystal setup (which will be discussed later on) this can be compensated. However, a bias transmission do not always need to be a negative thing. In many setups it is preferred to have a bias at $\Delta\varphi = \pi/2$, because the transmission curve (equation 3.36) is approximately linear in a rather large interval around this bias voltage and hence the response is relatively high.

In a laser cavity, one would like to use as few components as possible, because a larger cavity causes diffraction problems. In the case of an electrooptic modulator, it means that there would be an advantage to use only one polarizer. A such one polarizer electrooptic modulator setup is shown in figure 3.4. There are two great differences between the setups in figure 3.3 and figure 3.4. The first difference is that the beam propagates twice through the crystal in the second setup, which means that there is only a need to have a quarter wave retardation for each pass in order to rotate the polarization by 90°. The second difference is that the transmission is 100% when the field is off in the latter case, in comparison to the first case where the transmission is 100% when the half wave voltage is applied.

The voltage required to achieve quarter wave retardation is given by:

$$V_{\pi/2} = \frac{1}{2} \frac{\lambda}{n_3^3 r_c} \frac{d}{L} \qquad (3.47)$$

i.e. $V_{\pi/2} = V_\pi/2$. The π radians phase shift introduced by the mirror is of no interest, because both polarization components are shifted by π radians, and therefore there is no phase shift difference between the components.

3.3 Electrooptic crystal materials

Most electrooptic crystals are grouped into different families depending on their crystal and molecular structure. In this chapter technical data and important aspects of the most important and commonly used crystals are shortly going to be presented. The main goal of the section is to understand the choice of the electrooptic crystal material for the modulator in the Q-switched laser.

It is natural to start the overview by looking at the **KDP-family**, which is a group of crystals with molecular structure MY_2XO_4, where M represents K, Rb, Cs or NH_4(A), and Y represents H or D, and X represents P or As. The most common of the possible combinations are KDP, ADP, DKDP and DADP. The most critical fact of these crystals are that they are hygroscopic, a fact from which both positive and negative properties follows. One of the good properties is the high optical uniformity, which can be achieved even in large and fast grown samples. However, since the material is hygroscopic it is soluble in water and must therefore be encapsulated in some kind of protection layer. This of course introduces reflection losses at each interface; at best the total transmission loss can be reduced to 4% using AR-coatings.[36] A such large loss in a laser cavity is an issue and should be avoided, which means that this crystal would not be a good choice for the Q-switching purpose.

The next important group is the **LNB-family**, consisting of $LiNbO_3$ (LNB) and $LiTaO_3$ (LTA). In contrast to the former group, these crystals are non-hygroscopic, which simplifies the practical handling of the materials. For instance there is no need for encapsulation, which of course gives much lower transmission losses; with AR-coatings the transmission losses can be reduced to less than 1%.

For the Q-switching purpose, these crystals have two limitations that need to be considered. Firstly, photorefractive damage in LNB makes this crystal useful only for intensities below 100 MW/cm^2. Secondly, piezo-electric ringing of the r_{22} electrooptic coefficient arises between 1 kHz and 10 MHz in LNB.[36] Even though it is possible to push the lower limit up to 10 kHz, this is still to low for the laser TV application which requires a pulse repetition frequency of at least 18 kHz.

Another essential difference between the LNB- and KDP-family, is that the crystals of the LNB-family can be used in the transverse field configura-

tion, whereas the crystals of the KDP-family are mostly used with longitudinal applied electric field. For the 3m point group of symmetry, which the LNB-family belongs to, there are two different kinds of transverse modes possible: one with the electric field along the x- or y-axis and the k-vector along the z-axis, and one with the electric field along the z-axis and the k-vector along the x-axis. In the former case, the electrooptic coefficient which can be used is quite low, $r_{22} = 6.8$ pm/V. In contrary, in the latter case, a much larger effective electrooptic coefficient can be used. However, since there will be a constant refractive index difference term generating a bias phase shift in that case, similar to the first term in equation 3.43, it is a must to have a fast compensation for this, because the phase shift introduced by the birefringence is very temperature sensitive. The solution is often to use a two crystal setup, which will be discussed more in depth later on. In principle this two crystal setup just consists of two crystals rotated 90° relative to each other's x-axes. But for this to work in practice, the crystals need to show high optical uniformity, so that both crystals introduce the same phase retardation. For the crystals of the LNB-family it is very hard to achieve a satisfying high uniformity, due to growth difficulties in the manufacturing process. [36]

Due to the disadvantages with the KDP- and LNB-family, the technology has pushed further to find new better electrooptic materials. One group of rather new materials is the **LGS-family** ($La_3Ga_5SiO_{14}$) which possess the rather high damage threshold 950 MW/cm^2. [36] However, these can only be operated at low frequencies, because of problems with piezoelectric ringing at higher frequencies.

Another new material is **BBO**, abbreviated for β-BaB_2O_4. This material possess a damage threshold of approximately 5 GW/cm^2 for 10 ns pulses, which is extremely high in the context. In addition, no photorefractive effect is occurring at these intensities. However, piezoelectric ringing is appearing already at 6 kHz, which restrict the use of this modulator material to lower frequencies than required for the laser-TV application.[36] The electrooptic coefficient is also too low ($r_{22} < 2.7$ pm/V), to give reasonable demands on the voltage equipment in our lab.

The last group to be presented is the **KTP-family**. Crystals in this family exhibit very good electrooptic properties and do not suffer from the problems found in the other crystals discussed above. The two most important materials are $KTiOPO_4$ (KTP) and $RbTiOPO_4$ (RTP). Both of these crystals have high effective electrooptic coefficients: $r_{c2} = 22.9$ pm/V for KTP and $r_{c2} = 23.6$ pm/V for RTP. The most remarkable property is that the upper limit for piezoelectric ringing for KTP is as high as 30 kHz and for RTP no piezoelectric ringing is detected at all. This is a unique property of the KTP-family. [36]

Further on both crystals show high optical uniformity in the y-z plane,

Property	Notation	Value
Electrooptic coefficients (@ 633 nm) [35],[34]	r_{13}	10.6 pm/V
	r_{23}	12.5 pm/V
	r_{33}	33.0 pm/V
Transparency range [33]		0.35 - 4.5 μm
Damage threshold [36]		1800 MW/cm^2
(@ 1064 nm and 10 ns pulses)		
Point group		mm2
Density [33]		3.6 g/cm^3
Electric resistivity [33]		10^8 Ω/cm
Relative dielectric constant [33]	ε_{eff}	13

Table 3.2. *Summary of properties of RTP.*

which is the explanation why the x-axis is often chosen as propagation direction. However, there are also some properties that differ between KTP and RTP. One difference is that for RTP the damage threshold is quite high, 1800 MW/cm^2 for 10 ns pulses, compared to KTP for which the damage threshold is only 800 MW/cm^2. A second difference is that the electric resistivity for RTP is of the order of 10^8 Ω/cm, compared to the electric resistivity for KTP which is of the order of 10^6 Ω/cm. Hence, the risk of electrochromic damage is much smaller in RTP. [36]

After this overview of electrooptic crystal materials, RTP seems to be an excellent choice as modulator crystal material in the q-switched laser used for laser TV applications, especially regarding the high repetition frequency, the high damage threshold, the high electrooptic coefficients and the high electric resistivity. A summary of the important properties of RTP is presented in table 3.2.

4 Realization of the electrooptic amplitude modulator

In this section, the construction and characteristics of the homemade electrooptic modulator mentioned earlier will be presented. First the crystal orientations and the design of the holder will be discussed. Then the setup of the voltage supply will be described and finally the results of different characterization experiments will be summarized. The modulator was characterized in the pulsed regime, both when it was operated at a bias voltage and when it was operated at zero bias voltage.

4.1 Construction of electrooptic modulator

In section 3.3, different electrooptic crystal materials were discussed. From the discussion, RTP seemed to be the obvious candidate for the q-switching purpose. Modulators based on RTP have earlier been examined and are now commercially available.[36, 37] The main problem with the RTP crystals is the temperature dependent birefringence, which must be compensated somehow. Two different techniques are commonly used: temperature tuning and compensation with two crystals.[36, 38] The temperature tuning technique is based on temperature dispersion; by regulating the crystal temperature, the phase shift between the two electrical field components can be controlled to some extent. However, this configuration is not so stable, and therefore the setup with two equally long crystals is often used. Ebbers et al [38] discussed some different double-crystal configurations, which could be utilized in order to compensate the birefringence in KTP. Since RTP and KTP have similar properties, this discussion applies good to RTP as well. In this thesis, a variant of one of the setups Ebbers discussed will be examined, see figure 4.1. The two crystals in the figure are equally long and are aligned with their x_1 axes parallel to each other. Furthermore, the x_2 axis of one of the crystals is parallel to the x_3 axis of the other crystal, meaning that the crystals have been rotated 90° relative to each other. The principle of the double-crystal compensation can now be understood by considering the two different electric field components polarized in the x- and y-directions respectively (i.e. the electric field components polarized parallel to the main axes of the crystals). If the crystals are perfectly aligned, then the optical path lengths through the crystals will be the same for the two different electric field components, and hence the total polarization state will be the same before and after the crystals.

An advantage with the double-crystal setup is that it compensates for average temperature changes. However, there are also disadvantages with this method. Firstly, the relative alignment between the two crystals must be very precise, and secondly, the two crystals must show high optical uniformity.[36]
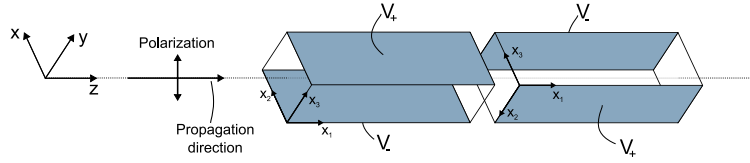
Figure 4.1. *Thermal compensation scheme used in the electrooptic modulator constructed. The incident light is supposed to be linearly polarized, with the polarization 45° tilted relative to the x_2 and x_3 axes of the crystal.*

Three different sets of RTP crystals were used in the experiments during this project. Each set of two crystals were cut from a larger piece of RTP. The two largest crystals were cut from a crystal with dimensions 11.0 x 6.0 x 1.0 mm (xyz), which gave two crystals each with dimensions 11.0 x 2.9 x 1.0 mm. The two other sets of crystals were cut from unpoled areas of periodically poled crystals. The sizes of the crystals of these two pairs were 6.5 x 2.2 x 1.0 mm and 4.8 x 2.0 x 1.0 mm respectively. As electrodes, silver glue was used (Electrolube SCP 003).

The construction of the modulator holder is shown in figure 4.2. Two electrically separated transmission lines connected each SMA contact with a corresponding crystal. As isolation, PMMA was used, and as conductors, copper was used. The crystals were glued on the holder using the type of silver glue mentioned above. To indirectly control the temperature of the crystals, a low current peltier element (Supercool) was attached to the copper pieces holding the crystals. A thermistor close to one of the crystals, sensed the temperature. In order to be able to do fine adjustments of the orientation of the modulator, the holder was placed on a translation stage.

4.2 Voltage supply

In order to be able to apply short voltage pulses over the crystal, the setup depicted in figure 4.3 was used. Pulses from a pulse generator (Stanford research systems, Model DG535) was sent into a pulse amplifier, constructed by Leif Kjellberg at ACREO for this specific purpose. The amplifier module was based on a special transistor technique. By changing the voltage of the high voltage DC supply (Oltronix LS 122R), the amplitude of the outgoing pulses could be varied. The maximum allowed input voltage was 500 V, and therefore also the outgoing pulse amplitude was limited by this value. In addition to the high voltage supply, a low voltage DC supply was needed to get the amplifier to function. The outgoing pulse characteristics from the amplifier depended on several parameters, such as the pulse length from the pulse generator, the voltage from the high voltage DC supply and the
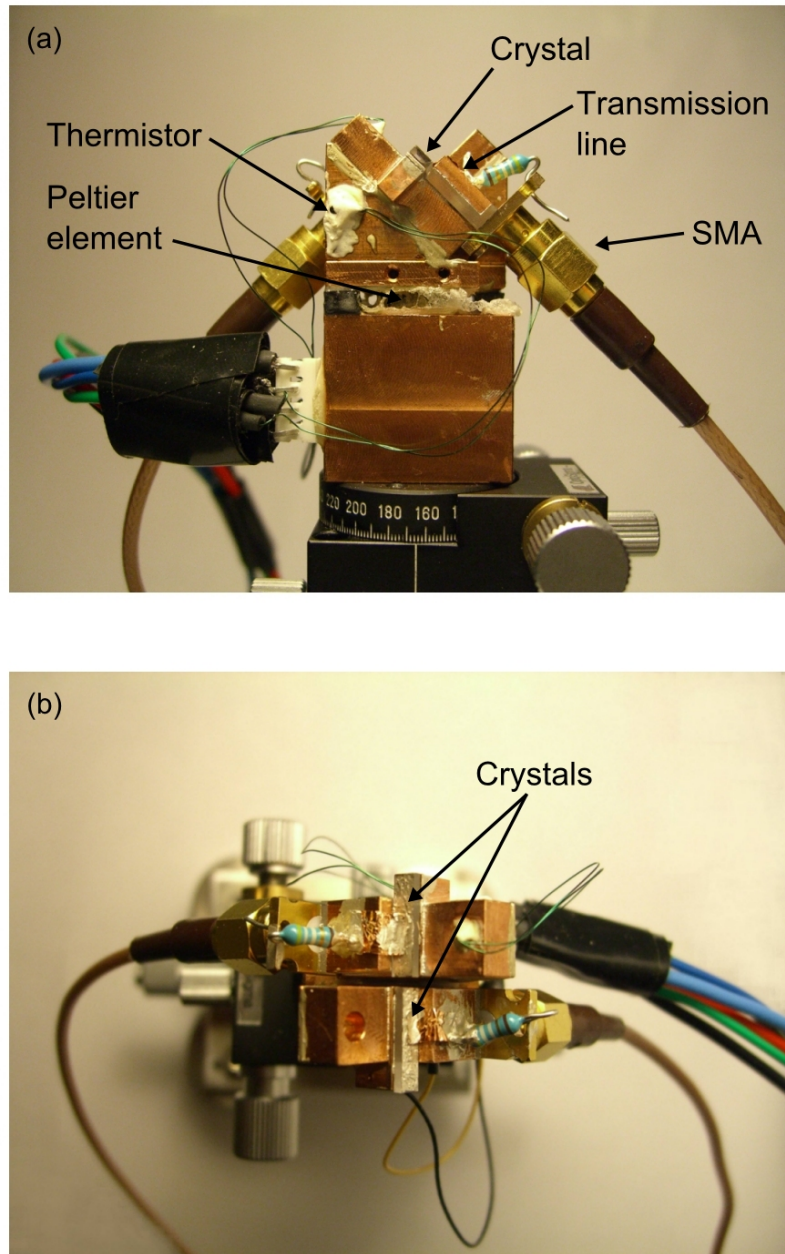
Figure 4.2. *Electrooptic modulator.* **(a)** *Side view.* **(b)** *Top view. The two 50 Ω resistances visible in the figures, were used to reduce ringing effects in the electric pulses.*
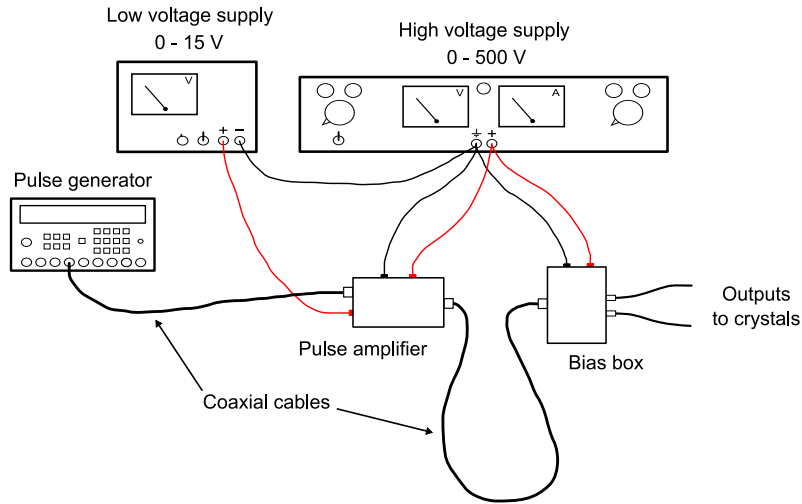
Figure 4.3. *Setup of the voltage supply. With the amplifier used, it was possible to obtain a peak voltage of approximately 500 V.*

voltage from the low voltage DC supply. The polarity of the pulses was easily set on the pulse generator.

The pulses from the amplifier box was sent into a bias box, which made it possible to have a bias voltage applied over the crystals. For instance it was possible to have a bias at 500 V and pulses with an amplitude -500 V, i.e. when the pulses were applied, the voltage dropped down to zero.

4.3 Biased measurements

In order to test the performance of the modulator, an amplitude modulation setup was built. To obtain the lowest possible half-wave voltage, the two longest crystals were glued on the modulator holder. A Nd:YVO$_4$ laser, emitting vertically polarized light at 1064 nm, was used as laser source, which meant that no polarizer was needed in front of the crystals. As analyzer, a Glan Taylor polarizer was utilized. Initially it was noted that the birefringence compensation of the modulator was not totally perfect. Therefore a half-wave plate was placed directly after the modulator crystals as compensation. By slightly tilting the wave-plate, almost perfect compensation was achieved.

As a first experiment, the DC voltage was tuned from 0 V to the maximum allowed value of 500 V. The result is shown in figure 4.4. The lines in the figure represent the theoretical behaviour described by the equations 3.36 and 3.45. Note that the theoretical half-wave voltage was lower than the value actually obtained. As seen in the figure, the measured half-wave voltage theoretically corresponded to the half-wave voltage expected for two
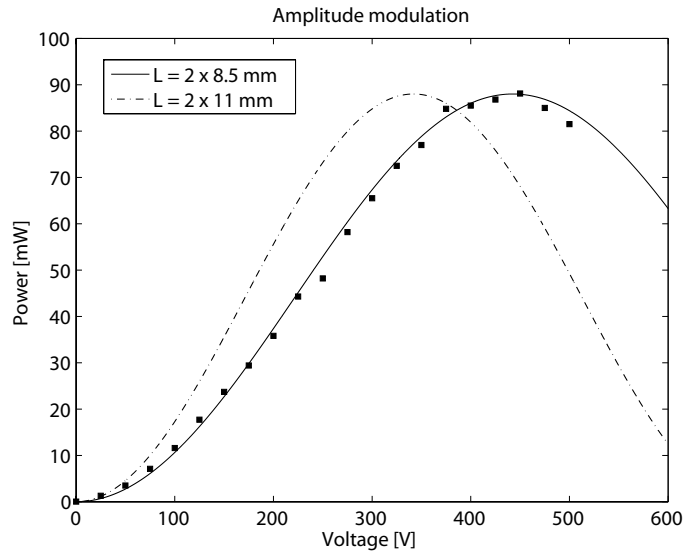
Figure 4.4. *Amplitude modulation. The measured half-wave voltage 443 V theoretically corresponded to the half-wave voltage of two crystals with the lengths 8.5 mm. The expected half-wave voltage (dashed line) was 100 V lower.*

crystals with the lengths 8.5 mm. The deviation from the expected voltage, could be due to several reasons. Firstly, the contact electrodes might not have been perfect close to the crystal ends; less glue were put on the surfaces close to the apertures (in order to avoid dirt on the AR coatings), which might have reduced the conductivity. Secondly, the electrooptic coefficients specified by the manufacturer, might not have been completely accurate for the crystal samples used.

Superimposed on the positive bias, negative pulses were applied. However, soon a major problem arised: one of the crystals turned very dark and the transmission through the crystal decreased, see figure 4.5. Also the other crystal showed some initial darkening near one of the electrodes. The darkening effect is called electrochromic damage and occurs in crystals when an electrical field is applied for a longer time. The phenomena is well investigated in KTP, see for instance references [39] and [40]. However, the darkening was not expected in RTP, due to the high resistivity of the RTP material. A way of solving the problem, might be to put thin isolating layers of SiO between the crystal and the electrodes. However, in that case there would be a large voltage drop over the isolating layers, which means that the applied voltage would need to be higher. The voltage from the supply would probably not be high enough for such a configuration. Hence, the conclusion must be that, with the equipment available, the modulator cannot be used

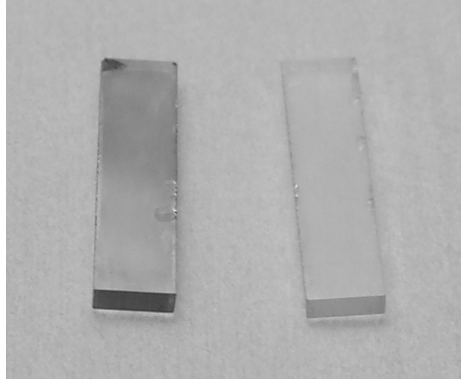**Figure 4.5.** *Electrochromic damage in the crystal to the left, drastically reduced the transparency. The crystal to the right only showed some initial electrochromic damage.*

in the biased configuration.

In order to recover the crystal transparency, the crystals were put on a cover glass, which in turn was placed on a heat plate. The crystals were heated for one hour at each of the temperatures 200 °C, 230 °C and 270 °C. However, no improved transparency was visible. First when the temperature was increased to 500 °C, a drastic increase in transparency was visible. Later measurements showed that the transparency was almost 100 %; the losses were smaller than the instability of the laser, and were therefore hard to measure.

4.4 Non-biased measurements

The two crystals used in the last experiment were remounted on the modulator holder. Again, voltage pulses were applied over the crystals, however this time without a constant bias voltage superimposed. In figure 4.7(a) and (b) an electric pulse and the corresponding optical modulation pulse are shown. The electric pulse was optimized in order to obtain the shortest possible rise time of the optical pulse. A close-up of the optimized pulse front is shown in figure 4.7(c). From the figure, the rise time is approximated to be 15 ns.

It is important to notice that a quarter-wave plate was used to compensate the non-perfect two-crystal birefringence compensation in the measurements above. In order to be able to evaluate the function of the Q-switch later on, it is vital to know how the polarization state changes when the light propagates through the crystal only. In figure 4.6, the polarization states before and after the crystal are plotted. Before the measurements were performed, the modulator was aligned so that the largest possible modulation was obtained. As can be seen in the figure, the polarization of the light from the laser was not perfectly linear. However, since this was the laser which was going to be q-switched, it is interesting to see how this particu-

lar polarization state changes when propagating through the crystal. From measurement data, the contrast ratio of the light from the laser was determined to be 1:145 and the contrast ratio of the outgoing light from the RTP crystals was determined to be 1:25.
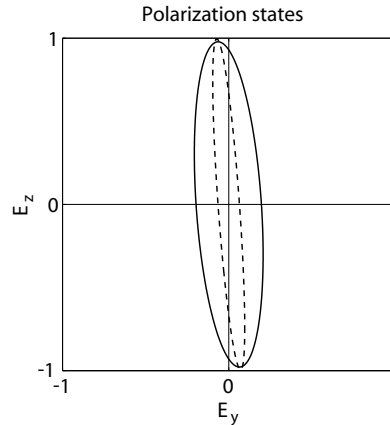
Figure 4.6. *The polarization states before (- -) and after (-) the RTP crystals. To determine the polarization states, the analyzer was rotated and at every twentieth degree the transmitted power was measured. Then the measured values were fitted to a model describing the system, and finally, using the model, the polarization state could be plotted.*

At this point it should be mentioned that no electrochromic damage was visible in the crystals even after several hours of operation in the non-biased mode. Note however that this does not imply that electrochromic damage will not appear when operating the modulator for a longer term. The long term behavior has not been investigated in this project, but is of course a crucial point for commercial modulator systems.

4.5 Conclusions

The characterization experiments of the electrooptic modulator showed that no bias voltage should be applied over the crystal, due to the risk of dichroic damage. Hence, the modulator should only be used in the pulsed mode. In a single pass configuration, a maximum modulation of 90 % was achieved, restricted by the maximum voltage of the voltage supply. In a double pass configuration (see figure 3.4) higher modulation is expected, since the half-wave voltage is lowered by a factor of two. The shortest achieved rise-time of the pulses was 15 ns.

When the electrooptic modulator will be used as a Q-switch in the next section, it is important to obtain a high contrast ratio. The experiments above showed that the contrast ratio achieved was low, and therefore a compensation wave plate will probably be needed in the Q-switch.

(a)

(b)

(c)

Figure 4.7. *(a)* *Voltage pulse out from the bias box.* *(b)* *Electrooptic modulation pulse. The highest modulation, 90 %, was obtained when the maximum allowed voltage was set on the high voltage supply.* *(c)* *The front of 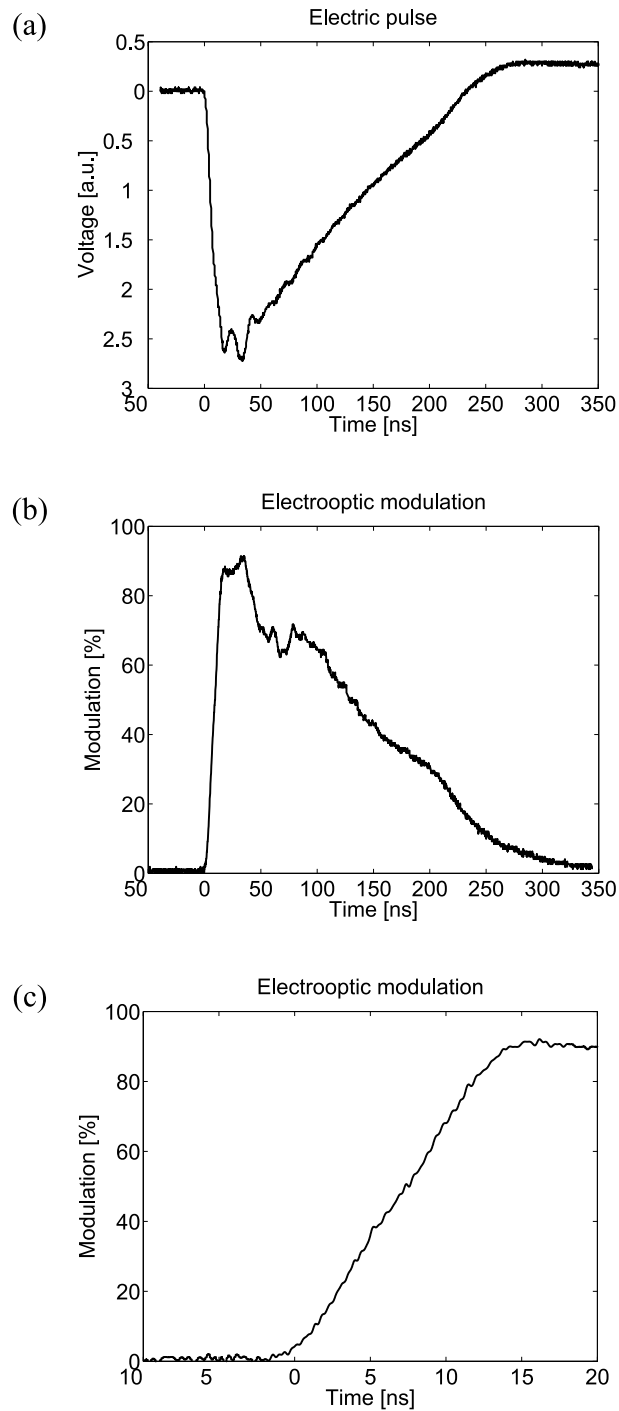the modulation pulse plotted in a smaller time scale. From the figure, the rise time is determined to be approximately 15 ns.*

5 Q-switched laser

In this chapter, the construction of the actively Q-switched laser will be described. As a starting point, a short introduction to the Q-switching technique will be presented in the next section. Then, in the next following section, different continuous wave (CW) lasers will be examined. Two of these lasers were successfully Q-switched at low output powers. The characteristics of those q-switched lasers are described in the final section of this chapter.

5.1 Introduction to Q-switching

Q-switching is a very common technique used to generate pulses with high peak intensities. The basic principle is to increase the losses in the cavity in order to suppress lasing, so that the population inversion in the laser medium becomes much higher than in the normal continuous wave case. Then, after the population inversion has been built up, the losses are quickly reduced to the normal level through a switching mechanism, whereupon a very fast depopulation of the upper laser level occurs, which leads to a light pulse. The name Q-switching refers to the fact that the cavity quality factor Q, defined as the ratio between the stored energy and the loss per cycle in the cavity, is modulated in this technique.[41, 25]

Mathematically the process can be described by the following set of rate equations [41]:

$$\begin{cases} \dfrac{dn}{dt} = K\,n\,N - \gamma_c\,n \\[2mm] \dfrac{dN}{dt} = R_p - \gamma_2\,N - K\,n\,N \end{cases} \tag{5.1}$$

where $N(t) = N_2(t) - N_1(t)$ is the population difference between the upper and lower laser levels, $n(t)$ is the photon number, R_p is the pump rate, γ_2 is the upper laser level decay rate, γ_c is the cavity decay rate and K is a coupling constant. The cavity decay rate can be calculated through the following expression:

$$\gamma_c = \frac{t_r}{L - \ln(1-T)} \approx \frac{t_r}{L+T} \tag{5.2}$$

where t_r is the cavity round-trip time, T is the outcoupling transmission, and L represents the remaining cavity losses.[42] The coupling constant K is given by the relation $K = 2\sigma/(t_r A)$, where σ is the stimulated emission cross section and A is the cross section area of the laser mode, which is here approximated to be constant throughout the cavity.[41, 25]

The differential equation system 5.1 cannot be solved analytically. However, there are several approximations which can be made on the system.

A detailed discussion treating such approximations can be found in reference [41]. Numerically the equation system can be solved in for instance MATLAB, utilizing the Runge-Kutta 4 method.

In practice, there are several Q-switching techniques which can be used, for instance rotating mirror Q-switching, electrooptic Q-switching, acoustooptic Q-switching, passive saturable absorber Q-switching, and thin-film Q-switching. In this diploma thesis project, the intention was to build an electrooptic Q-switch. The electrooptic Q-switching technique is a fast method in comparison to the other methods mentioned. However, one must consider that most electrooptic crystals possess a fairly low damage threshold, see section 3.3.[41]

5.2 Construction and characterization of the CW laser

In earlier reports, Nd:YVO$_4$ was chosen as laser material in Q-switched devices based on RTP-modulators.[36] The Nd:YVO$_4$ material has several favorable properties as for instance strong broadband absorption, large stimulated emission cross section, and linearly polarized laser output.[43] Some other important properties are summarized in table 5.1. Since Nd:YVO$_4$ seemed to have functioned very well as laser gain medium in earlier Q-switched devices, we decided to use this material in the laser built in this project.

Peak pump wavelength	808.5 nm
Laser wavelength	1064.3 nm
Linewidth	0.8 nm
Spontaneous lifetime	100 μs

Table 5.1. *Laser properties of Nd:YVO$_4$.[43, 44]*

A good starting point when building a Q-switched laser is to characterize the laser in CW mode. Two different crystals were examined as gain medium in this work - let us denote these as crystal I and crystal II. To pump the crystals, a LIMO laser diode was used. The emission spectrum of this diode at different temperatures is shown in figure 5.1(a). In the best case, the peak absorption wavelength and the peak emission wavelength overlap. Since Nd:YVO$_4$ has an absorption peak at 808.5 nm [45], it can be realized from figure 5.1 (a) that the diode must be heated above 35 °C in order to achieve such an overlap. The temperature dependency of the absorption is more directly illustrated in figure 5.1(b), where the absorption in a Nd:YVO$_4$ crystal with doping concentration of 0.4 % is plotted for the temperatures 30 °C and 32 °C respectively. However, it is important to note that the lifetime of the laser diode shortens when it is driven at a temperature above

30 °C, and therefore the temperature was kept at 30 °C during the rest of the experiments, even though higher absorption would be achieved at higher diode temperatures.
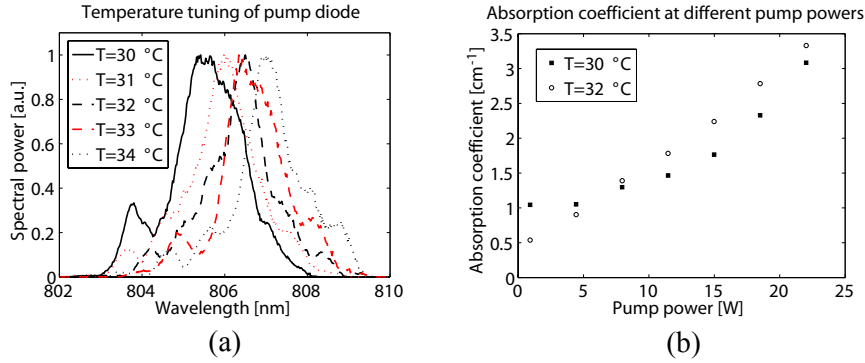

Figure 5.1. *(a) Temperature tuning of the pump diode. (b) Effective pump absorption coefficient of the Nd:YVO$_4$ crystal measured at different pump powers and at two different temperatures of the pump diode.*

Crystal I had a doping concentration of 0.4 %. The dimensions of the crystal were $3.0 \times 3.0 \times 3.0$ mm^3. One side of the crystal was coated to be HT at 808 nm and HT at 914 nm, and the other side of the crystal was coated to be HT at 808 nm and HR at 914 nm. The low reflectance at 1064 nm at the crystal surfaces was initially not assumed to be an issue. The reason for not using a crystal, which was AR coated at 1064 nm, was simply that such a crystal was not available in the lab at time when the first experiments were performed.

The pump beam was focused to a spot with the $1/e^2$-intensity beam radius 105 μm parallel to the crystal c-axis and 96 μm perpendicular to the crystal c-axis. As input coupler, a flat mirror coated to be HR at 1064 nm and HT at 808 nm was used. As output coupler, two different planoconcave mirrors were used, both with the radius of curvature 200 mm. One of the mirrors had the reflectance 85 % at 1064 nm, and the other mirror had the reflectance 90 % at 1064 nm.

The output power at 1064 nm as function of the pump power is plotted in figure 5.2. Note that there is a sudden change in the slope efficiency around 15 W of pump power. This behavior has earlier been observed, and was then believed to be a consequence of a higher mode starting to lase at a higher pump threshold.[46] This do however not explain the high beam quality factor close to the pump threshold; higher order modes normally start to lase at higher pump powers, meaning that higher beam quality factors are normally found at higher pump powers. An explanation for the high beam quality factor close to the pump threshold in this case might be that the

coatings on the crystal disturbed the build-up of a nice laser mode at low powers. In fact, later on it was found out that the reflectance on the side of the crystal closest to the outcoupling mirror, was high enough in order to obtain lasing between this side of the crystal and the incoupling mirror. Hence, the laser built actually consisted of two coupled cavities. A such configuration was not usable for the Q-switching purpose, since the switch was going to be placed closer to the outcoupling mirror than the crystal, and would therefore only be able to kill the outer cavity. Hence, the inner cavity would still lase even though the outer cavity was killed. This behavior was confirmed experimentally. In conclusion, the obvious fact that the crystal surfaces should be coated for the wavelengths intended to be present in the laser cavity, is of vital importance when Q-switching a laser.

Crystal II was coated to be HT at 1064 nm and HT at 808 nm on one side, and to be HR at 1064 nm and HT at 808 nm on the other side. Hence, the latter side functioned as incoupling mirror. In figure 5.3, the output power as function of the pump power is plotted for two different outcoupling mirrors. As can be seen, the slope efficiency is approximately the same for both outcouplings, which is a sign of low losses in the cavity. The sudden drop in power at higher pump powers is believed to be caused by damage of the coatings at higher intensities.

Thermal lensing can be a critical issue for high power lasers. In figure 5.4, the results from a simulation of the thermal lens in the $Nd:YVO_4$ crystal are shown. From the graph, the focal length is determined to be as short as 20 mm when the pump power is 15 W. According to simulations done in WinLase, such a short thermal focal length gives an unstable cavity. However, in reality the laser was stable at a pump power of 18 W. The model was hence too simplified in this case, but might anyway give an estimate of the thermal focal length.

5.3 Q-switching experiments

The setup of the Q-switched laser built in this project is illustrated in figure 5.5. The four last components in the cavity, including the outcoupling mirror, functioned as an electrooptic amplitude modulator. A similar setup was described in section 3.2, with the only exception that a quarter-wave plate was not used there. In the setup in figure 5.5, the quarter-wave plate introduces a π radians phase shift, meaning that the amplitude modulator reflects 100 % of the incoming light back when the voltage is held at the quarter-wave voltage, in contrast to the setup depicted in figure 3.4, where no light is reflected back when the voltage is held at the quarter-wave voltage. Thus, by using the configuration in figure 5.5, there is no need of having a constant bias voltage over the crystal in order to supress lasing, and hence electrochormic damage could be avoided.

In the last section, two different crystals were compared. Here only the

Figure 5.2. *Laser output power as function of pump power (when using crystal I), measured for two different outcoupling mirrors. The pump threshold was estimated to be 0.4 W for both outcouplings.*
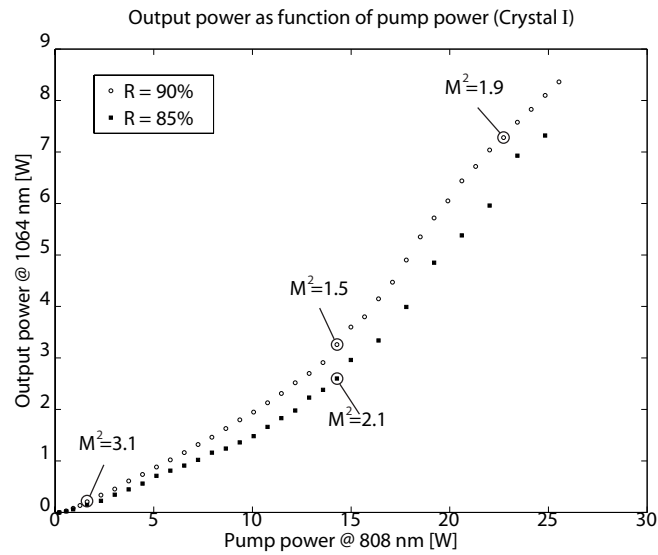
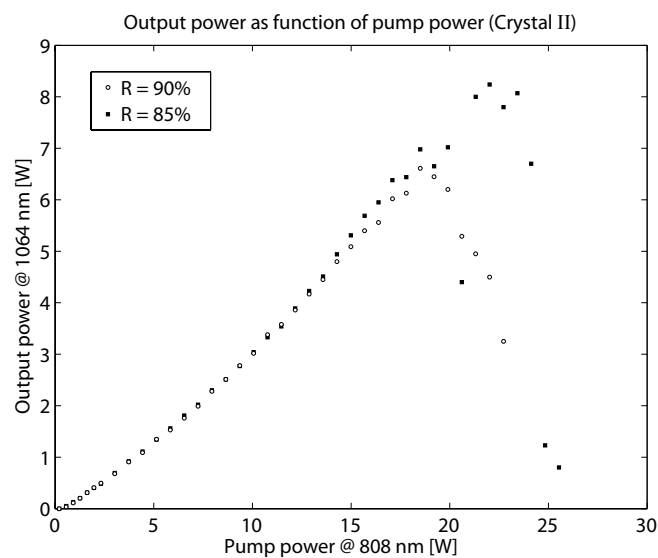

Figure 5.3. *Laser output power as function of pump power (when using crystal II), measured for two different outcoupling mirrors. The pump threshold was estimated to be 0.3 % for the 10 % outcoupling and 0.4 W for the 15 % outcoupling.*
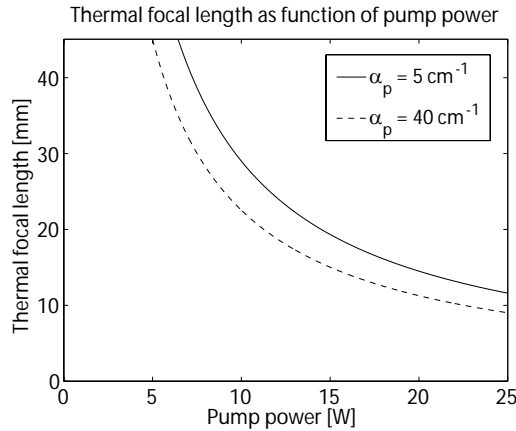
43

Figure 5.4. *Thermal focal length as function of pump power calculated using a simple model described by Innocenzi et al [47]. The thermal focal length is dependent on the effective absorption coefficient, which in turn is dependent on the overlap between the emission spectrum of the pump and the absorption spectrum of the gain medium. In the ideal case of a pump with narrow bandwidth and perfect overlap, the effective absorption coefficient is approximately $\alpha_p = 40$ cm^{-1}. However, in the normal case, the absorption is considerably lower.*

Q-switching experiments of crystal II will be described. As already mentioned, one side of this crystal acted as input coupler and therefore the leftmost mirror in figure 5.5 was not needed. As a first Q-switching experiment, the optical elements of the cavity were simply aligned, without any compensation for the phase shift contribution resulting from the nonperfect birefringence compensation in the electrooptic modulator. To adjust the wave plate into its correct rotational angle, the pump power was first turned on and increased until the cavity started to lase. Then, the quarter wave plate was rotated, until the cavity stopped lasing. However, it was only possible to stop the lasing at low powers, not at higher powers. This was probably because of the fact that the light, which had propagated twice through the modulator, was not perfectly linear, and therefore there was some amount of the light which could pass through the polarizer. When the pump power was increased, the amount of light passing through the polarizer also increased, and at some point laser threshold was reached.

In order to optimize the output power from the laser, a number of parameters could be adjusted, for instance the voltage of the low voltage supply, the voltage of the high voltage supply, the pulse repetition frequency and the length of the pulses from the pulse generator. The voltage of the low voltage supply and the length of the pulses from the pulse generator were kept at the same values as in the electrooptic amplitude modulation experiments in the last chapter. As expected the average power was strongly dependent on
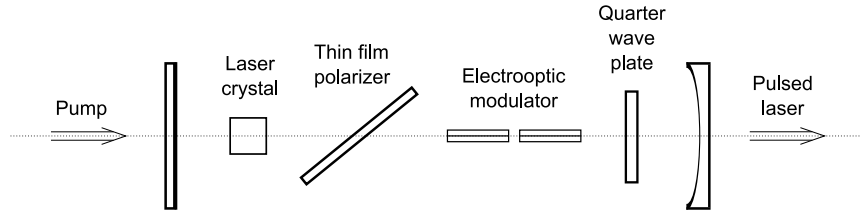
Figure 5.5. *Setup of the Q-switched laser. Note that a thin film polarizer, tilted in its Brewster angle, was used.*

the pulse repetition frequency; the average power increased with the pulse repetition frequency and was limiting a constant value for higher frequencies. The optimized voltage of the high voltage supply depended on the rotational angle of the quarter wave plate and on the exact orientation of the modulator.

With an output coupling of 10 %, the maximum pulse energy was detected when pumping the crystal with 3.9 W at 808 nm. At this pump power and at a pulse repetition frequency of 1000 Hz, the pulse energy was measured to be 12.2 μJ. The peak pulse power was 360 W and the pulse length was 32 ns. When the pump power was increased further above 3.9 W, the pulse energy started to decrease. This was probably because of the problem with the nonperfect birefringence compensation in the electrooptic modulator discussed above, but could also be caused by thermal lensing in the laser crystal.

With an output coupling of 15 %, the maximum output power was obtained when pumping the crystal with 5.3 W at 808 nm. At this pump power and at a pulse repetition frequency of 1000 Hz, a pulse energy of 36 μJ was obtained. The pulse shape is plotted in figure 5.6. From the figure, it can be seen that the peak pulse power was approximately 1.1 kW.

In order to increase the pulse energies, the nonperfect two-crystal compensation of the electrooptic modulator needed to be compensated somehow. This was done by inserting an additional wave plate in the cavity beside the quarter-wave plate, see figure 5.7. Two different available compensation wave plates were evaluated: a quarter-wave plate at 946 nm and a half-wave plate at 1064 nm. To achieve the best possible compensation, the wave plates were rotated in all degrees of freedom. To do this compensation a little more systematic, a small laser cavity was first built using a help mirror, as can be seen in figure 5.7. Then the electrooptic modulator was placed after the help mirror, whereupon the polarization state after the modulator was measured. At the best, a contrast ratio of 1:100 was obtained.

After the modulator, the quarter-wave plate was placed. The contrast
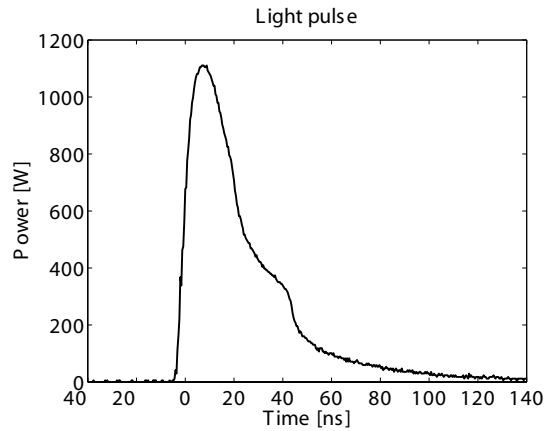
Figure 5.6. *Shape of the Q-switched pulse when the outcoupling was 15 % and the pump power was held at 5.3 W.*

ratio was measured to be 1:1.36, which was not close to the sought ratio 1:1 (circularly polarized light). With a half-wave plate at 1064 nm placed after the quarter-wave plate, a contrast ratio of 1:1.06 was achieved. Finally the output mirror was mounted after the last wave plate. With an outcoupling of 15 % this setup gave a maximum pulse energy of 22.3 μJ at a pulse repetition frequency of 1000 Hz and with a pump power of 5.8 W. Hence, the pulse energy obtained using this procedure was actually lower than the pulse energy obtained in the experiments without any compensation at at all.
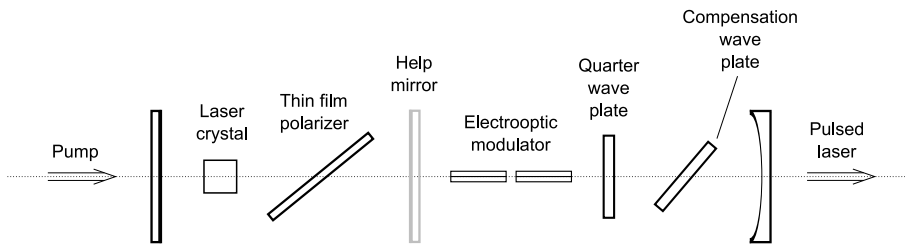
Figure 5.7. *Setup of the Q-switched laser with a compensation wave plate.*

In table 5.2, the data of the obtained pulses are summarized. As can be seen, the pulse energy was increased when the reflectivity of the outcoupling mirror was changed from 10 % to 15 %. One could therefore expect that even higher pulse energies would be achieved if the transmittance of the outcoupling would be increased even more. Unfortunately, there were no curved mirrors with lower reflectivity at 1064 nm available in the lab. However, one flat mirror with reflectivity 60 % was found. To use this mirror

as outcoupler, a folded cavity was built. When charchterized in CW mode, the slope efficiency of the folded cavity laser was found to be lower than the slope efficiency of the systems examined earlier. This was probably because of high losses in the folded cavity. Due to the low slope efficiency, the pulse energy obtained in the Q-switched mode was only slightly higher than the pulse energy obtained in the Q-switched system with the outcoupling transmission 15 % examined above - only 37.1 μJ pulses were obtained at a pulse repetition frequency of 1000 Hz.

	Outcoupling	
	15 %	10 %
Pulse energy [μJ]	36	12
Peak pulse power [W]	1100	360
Pulse length (FWHM) [ns]	24	30
Pump power [W]	5.3	3.9

Table 5.2. *Characteristics of the pulses achieved from the Q-switched laser when the pulse repetition frequency was held at 1000 Hz.*

As a final experiment, a combined actively and passively Q-switched laser was built. Two different Cr^{4+}:YAG passive absorbers with the initial transmissions 75 % and 94 % respectively were examined. The absorbers were placed directly after the laser crystal. With 15 % outcoupling and with the saturable absorber having an initial transmission of 75 %, a pulse energy of 5 μJ was obtained, i.e. much lower pulse energy was obtained with this saturable absorber than without the absorber inserted. When the saturable absorber with 94 % of initial transmission was used instead, a pulse energy of 39 μJ was achieved, i.e. the pulse energy was slightly higher with the absorber than without the absorber.

5.4 Conclusions

The pulsed lasers described in this chapter gave pulse energies of only a couple of tens of micro Watts. The best configuration, which included a saturable absorber, gave an output pulse energy of 39 μJ. The most important reason why the obtained energies were low, was the difficulty to compensate for the non-perfect birefringence compensation in the electrooptic crystals. In order to achieve higher pulse energies, the double-crystal birefringence compensation need to be improved.

In the following chapters, the frequency conversion stage of the RGB laser will be treated. *Note* that the lasers, which have been described in this chapter, will not be used in the frequency conversion measurements due to the low pulse energy and the low peak power.

6 Nonlinear optics

In classical optics, i.e. in the linear regime, two light beams which are sent into a material do not interact. However, for high intensities in some materials, interaction between the beams takes place, due to nonlinear effects. In this chapter, an overview of the basic theory of nonlinear optics will be presented, followed by a more in-depth description of the optical properties of KTP and a short introduction to the nonlinear-optics simulation software SNLO.

6.1 Nonlinear electrical polarization

Far away from resonances, the electric polarization $\mathbf{P}$ in a material, caused by an applied electric field $\mathbf{E}$, can be approximated by the following Taylor expansion:

$$\mathbf{P} = \varepsilon_0 \left(\boldsymbol{\chi}^{(1)} \cdot \mathbf{E} + \boldsymbol{\chi}^{(2)} : \mathbf{E}\,\mathbf{E} + \dots \right) \tag{6.1}$$

where $\boldsymbol{\chi}$ is the so called the dielectric susceptibility. The first term which just describes the linear behavior is often denoted by $\mathbf{P}_{\mathrm{L}}$ and the following nonlinear terms are often denoted $\mathbf{P}_{\mathrm{NL}}$. In nonlinear optics, the second and third order terms are the important terms.[48] For the processes described in this thesis only the second order term is of interest and therefore this specific case will be treated in detail.

The oscillation frequency of the polarization is directly linked to the frequency of the incident fields. For instance if two beams of frequencies ω_1 and ω_2 are sent into a nonlinear medium, the oscillation frequencies of the polarization can be any integer combination of the frequencies of the two beams ($n\,\omega_1 + m\,\omega_2$). Each of the fourier components of the polarization can now be written using compact tensor notation. For instance the sum frequency ($\omega_3 = \omega_1 + \omega_2$) component can be written as:

$$P_i^{(2)}(\omega_3) = \varepsilon_0 \, D^{(2)} \, \chi_{ijk}^{(2)}(\omega_3, \omega_1, \omega_2) \, E_j(\omega_1) \, E_k(\omega_2) \tag{6.2}$$

where $D^{(2)}$ is the second order degeneracy factor, which is equal to one if the fields are indistinguishable and equal to two if the fields are distinguishable. [48, 31]

At this point it can be noted that the earlier discussed linear electrooptic effect is actually a second order nonlinear effect. This can be understood from the fact that there are two electric fields interacting, one of which has zero frequency. With a field of zero frequency, there will be a term in the expression for the second order polarization, which is proportional to both the constant electrical field and the optical field. Since the term is linear in the optical field, it will have a similar property as the first order terms. This means that the refractive index, which is normally dependent on $\chi_{ijk}^{(1)}$, now

also will have a dependency of the term proportional to the applied electric field. Accordingly, by changing the d.c. field, the refractive index can be changed.[49, 50] This is just the principle of the electrooptic effect described in section 3.1.2.

6.2 Symmetries of the susceptibility tensor

There are several symmetries of the susceptibility tensor which are of importance in the study of nonlinear optics. The first symmetry is the interchangeability of the last indices of the susceptibility tensor, caused by the fact that there is nothing physically corresponding to changing orders of the electric fields in for instance formula 6.2. However, to keep this symmetry, also the indices of the frequencies must be interchanged. For the second order susceptibility, the symmetry can mathematically be described by:

$$\chi_{ijk}^{(2)}(\omega_3, \omega_1, \omega_2) = \chi_{ikj}^{(2)}(\omega_3, \omega_2, \omega_1) \tag{6.3}$$

This symmetry is referred to as the *intrinsic permutation symmetry*. [48, 51]

The second symmetry is the so called *Kleinman symmetry*. It is valid in a region where the optical frequencies are far away from the resonances of the medium. In addition there should be no resonances between the interacting waves. For regular materials and wavelengths this is also the case. From theory and experiments it can now be shown that if these conditions are satisfied, then the susceptibility can be considered as independent of frequencies. Mathematically this means that the cartesian coordinates (ijk in the equation above) can be permuted independently of the frequencies, from which follows that the arguments of the susceptibility tensor are often left out. [51]

$$P_i^{(2)} = \varepsilon_0 \, \chi_{ijk}^{(2)} \, E_j \, E_k \tag{6.4}$$

To make it clear that the Kleinman symmetry holds, the susceptibility tensor is often substituted for the so called d-tensor defined through the following relation:

$$d_{ijk} = \frac{1}{2} \, \chi_{ijk}^{(2)} \tag{6.5}$$

Since the d-tensor is symmetric in the last two indices, a contracted notation, $jk \rightarrow l$, is used in order to make the presentation of the tensor elements compact and nonsuperfluous. The contracted index representation is the same as used for the linear electrooptic effect, see table 6.1. [51]
The Kleinman symmetry does not only state that the tensor d_{ijk} is symmetric in the last two indices, but also that it should be symmetric for all permutations. This means that only 10 of the 18 elements of the reduced tensor d_{il} are independent: [51]

Elements	Reduced form
11	1
22	2
33	3
23,32	4
13,31	5
12,21	6

Table 6.1. *Connection between elements and their reduced forms.*

$$d_{il} = \begin{pmatrix} d_{11} & d_{12} & d_{13} & d_{14} & d_{15} & d_{16} \\ d_{16} & d_{22} & d_{23} & d_{24} & d_{14} & d_{12} \\ d_{15} & d_{24} & d_{33} & d_{23} & d_{13} & d_{14} \end{pmatrix} \tag{6.6}$$

A third important symmetry is based on the crystal structure of the material. Just as for the linear electrooptic tensor, the d-tensor must must be invariant with respect to the *symmetry operations of the point group* of the crystal. By considering mirror-plane symmetries and rotational-axis symmetries of the crystal, the number of elements can often be drastically reduced. In addition, constraints can sometimes be put on the nonzero elements. A table of d-tensors of different point groups can for instance be found in Yariv [31].

A last symmetry can be found in lossless media and these must be proved using quantum mechanics. However, in the context of this thesis this symmetry is not of major importance and will therefore not be presented here. The interested reader is recommended to consult Boyd [51] or Sutherland [48].

6.3   Coupled wave equations

In this section, nonlinear interactions between optical waves will be explained mathematically. As a starting point, the following wave equation will be used:

$$\boldsymbol{\nabla}^2 \mathbf{E} - \frac{1}{c^2} \frac{\partial^2 \mathbf{E}}{\partial t^2} = \mu_0 \frac{\partial^2 \mathbf{P}}{\partial t^2} \tag{6.7}$$

where it is assumed that there are no free charges and that there is no current density in the material. Furthermore, the magnetization has been set to zero.[48] For many nonlinear materials these assumptions are justified. By taking only the first and second order electric polarization into account, the above wave equation becomes:

$$\boldsymbol{\nabla}^2 \mathbf{E} - \frac{1}{c^2} \frac{\partial^2 \mathbf{E}}{\partial t^2} = \mu_0 \frac{\partial^2 \mathbf{P}^{(1)}}{\partial t^2} + \mu_0 \frac{\partial^2 \mathbf{P}^{(2)}}{\partial t^2} \tag{6.8}$$

By inserting $\mathbf{P}^{(1)} = \epsilon_0 \chi^{(1)} \mathbf{E}$ into this differential equation and then using the relations $c = (\mu_0 \epsilon_0)^{-1/2}$ and $n^2 = 1 + \chi^{(1)}$, one obtains

$$\nabla^2 \mathbf{E} - \frac{n^2}{c^2} \frac{\partial^2 \mathbf{E}}{\partial t^2} = \mu_0 \frac{\partial^2 \mathbf{P}^{(2)}}{\partial t^2} \tag{6.9}$$

where the tensorial property of the electric susceptibility has been left out. To simplify even a little bit further, it is common to assume plane wave propagation in for instance the z-direction: [31]

$$\frac{\partial^2 \mathbf{E}}{\partial z^2} - \frac{n^2}{c^2} \frac{\partial^2 \mathbf{E}}{\partial t^2} = \mu_0 \frac{\partial^2 \mathbf{P}^{(2)}}{\partial t^2} \tag{6.10}$$

Now consider two plane waves with frequencies ω_1 and ω_2 and a third plane wave with frequency ω_3 which is generated by the two other:

$$E_i^{(\omega_1)}(z,t) = \frac{1}{2} \left(E_i^{(\omega_1)}(z)\, e^{i(\omega_1 t - k_1 z)} + c.c. \right) \tag{6.11}$$

$$E_j^{(\omega_2)}(z,t) = \frac{1}{2} \left(E_j^{(\omega_2)}(z)\, e^{i(\omega_2 t - k_2 z)} + c.c. \right) \tag{6.12}$$

$$E_k^{(\omega_3)}(z,t) = \frac{1}{2} \left(E_k^{(\omega_3)}(z)\, e^{i(\omega_3 t - k_3 z)} + c.c. \right) \tag{6.13}$$

Here the subscripts just denote the Cartesian coordinates. Inserting the total field into the left side of equation 6.10 and performing the derivatives give rise to a large number of terms. To make the mathematics overviewable, only the terms which origin from the first term of equation 6.11 will explicitly be treated here:

$$\begin{aligned} LHS \;=\; & \frac{1}{2} \frac{\partial^2 E_i^{(\omega_1)}}{\partial z^2} e^{i(\omega_1 t - k_1 z)} - i k_1 \frac{\partial E_i^{(\omega_1)}}{\partial z} e^{i(\omega_1 t - k_1 z)} \\ & - k_1^2 E_i^{(\omega_1)} e^{i(\omega_1 t - k_1 z)} - \frac{n^2 w_1^2}{c^2} E_i^{(\omega_1)} e^{i(\omega_1 t - k_1 z)} + \dots \end{aligned} \tag{6.14}$$

By noticing that $k_1^2 = n^2 w_1^2 / c^2$, it can be seen that the third and fourth term cancel each other. Furtheron, the amplitude of the electric field can in most cases be assumed to change slowly over the distance of a wavelength.[48, 31] Mathematically this so called *slowly varying envelope approximation* (SVEA) can be expressed as:

$$\left| k_1 \frac{\partial E_i^{(\omega_1)}}{\partial z} \right| \gg \left| \frac{\partial^2 E_i^{(\omega_1)}}{\partial z^2} \right| \tag{6.15}$$

If this condition is applied on equation 6.14 only one important term of the original four terms remains.

$$LHS = -i k_1 \frac{\partial E_i^{(\omega_1)}}{\partial z} e^{i(\omega_1 t - k_1 z)} + \dots \tag{6.16}$$

Now, if the polarization on the right hand side of equation 6.9 is explicitly expressed using tensors, and if the derivation is performed, there will appear quite many terms of different frequency components. However, it is possible to separate the terms of different frequency components into different differential equations, because in this case the number of involved frequencies are finite and then it can be assumed that each frequency component must fulfill the differential equation.[31] By performing these steps, the following equations are obtained for the frequency components ω_1, ω_2 and ω_3:

$$-ik_1 \frac{\partial E_i^{(\omega_1)}}{\partial z} e^{-ik_1 z} = -2\,\varepsilon_0\,\mu_0\,\omega_1^2\,d_{ijk}'\,E_j^{(\omega_3)} E_k^{(\omega_2)*} e^{-i(k_3-k_2)z} \quad (6.17)$$

$$-ik_2 \frac{\partial E_k^{(\omega_2)}}{\partial z} e^{-ik_2 z} = -2\,\varepsilon_0\,\mu_0\,\omega_2^2 d_{kij}'\,E_i^{(\omega_1)*} E_j^{(\omega_3)} e^{-i(k_3-k_1)z} \quad (6.18)$$

$$-ik_3 \frac{\partial E_j^{(\omega_3)}}{\partial z} e^{-ik_3 z} = -2\,\varepsilon_0\,\mu_0\,\omega_3^2\,d_{jik}'\,E_i^{(\omega_1)} E_k^{(\omega_2)} e^{-i(k_1+k_2)z} \quad (6.19)$$

where the primes over the d-coefficients indicate that the coordinate system of the waves is used instead of the coordinate system of the crystal.[31] It is usual to denote this transformed nonlinear coefficient as d_{eff}. After some further simplifications, the expressions take the following forms:

$$\frac{\partial E_i^{(\omega_1)}}{\partial z} = -i\,2\,k_1\,d_{ijk}'\,E_j^{(\omega_3)} E_k^{(\omega_2)*} e^{-i(k_3-k_1-k_2)z} \quad (6.20)$$

$$\frac{\partial E_k^{(\omega_2)}}{\partial z} = -i\,2\,k_2\,d_{kij}'\,E_i^{(\omega_1)*} E_j^{(\omega_3)} e^{-i(k_3-k_1-k_2)z} \quad (6.21)$$

$$\frac{\partial E_j^{(\omega_3)}}{\partial z} = -i\,2\,k_3\,d_{jik}'\,E_i^{(\omega_1)} E_k^{(\omega_2)} e^{-i(k_1+k_2-k_3)z} \quad (6.22)$$

These are the so called *coupled wave equations* and they can be used to calculate the electric fields as they propagate through the medium. In the equations it is common to define the so called phase mismatch as $\Delta k = k_3 - k_2 - k_1$. Special solutions to the coupled wave equations will be presented in the next section.

6.4 Second order processes

In figure 6.1 the most important second order nonlinear processes are schematically presented. Three of these are of particular importance in this thesis: the second harmonic generation, the sum frequency generation and the optical parametric oscillation. The basics of these processes will be discussed in the following two sections.

6.4.1 Second harmonic generation and sum frequency generation

Second harmonic generation (SHG) is the process when two photons with the same frequency ω_f, is added to become one photon with frequency ω_{sh}.
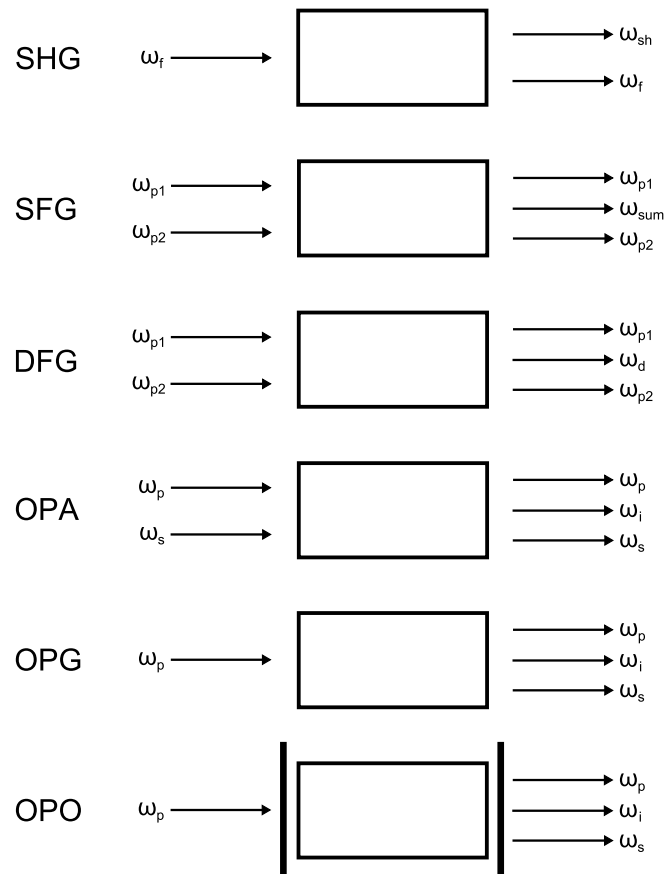
Figure 6.1. *Summary of second order nonlinear processes. From above: Second harmonic generation (SHG), Sum Frequency Generation (SFG), Difference Frequency generation (DFG), Optical Parametric Amplification (OPA), Optical Parametric Generation (OPG) and Optical Parametric Oscillation (OPO).*

Since the efficiency is the most important parameter describing the system, an analytical expression for this quantity would be very useful, not only as a calculation aid but also for the physical understanding. In many practical situations the incident field, usually called the pump field or the fundamental field, can be assumed to be undepleted, which simplifies the derivation of an expression for the efficiency from the coupled wave equations a little bit. After some calculations, the following expression for the conversion efficiency is obtained, if the assumption is applied:

$$\eta_{sh} = \frac{P_{sh}}{P_f} = \frac{8\,\pi^2\,d_{eff}^2\,L^2\,I_f}{\varepsilon_0\,n_f^2\,n_s\,c\,\lambda_f^2}\,\mathrm{sinc}^2(\Delta k L/2) \tag{6.23}$$

where P_{sh} is the power of the second harmonic field, P_f is the power of the fundamental field, L is the interaction length, I_f is the intensity of the fundamental field and $\Delta k = 2k_\omega - k_{2\omega}$ is the phase mismatch. In the case when $\Delta k \to 0$ and the intensities are high, the above formula is no longer valid since the pump will be depleted. Instead the efficiency is described by the following formula:

$$\eta_{sh} = \tanh^2\left(L/L_{NL}\right) \tag{6.24}$$

where

$$L_{NL} = \frac{1}{4\,\pi\,d_{eff}}\sqrt{\frac{2\,\varepsilon_0\,n_f^2\,n_s\,c\,\lambda_f^2}{I_f(0)}} \tag{6.25}$$

is a typical length, which gives a conversion efficiency of approximately 58 % in the phase-matched case.[48] Furthermore, there are analytical expressions for the conversion efficiency valid for Gaussian beams and for pulses.[52]

Sum frequency generation is the process when two photons of different frequencies, ω_{p1} and ω_{p2}, are added to generate one photon with frequency $\omega_{sum} = \omega_{p1} + \omega_{p2}$. In the undepleted case, the conversion efficiency for this process can be estimated by:

$$\eta_{sum} = \frac{P_{sum}}{P_{p2}} = \frac{8\,\pi^2\,d_{eff}^2\,L^2\,I_{p1}}{\varepsilon_0\,n_{p1}\,n_{p2}\,n_s\,c\,\lambda_s^2}\,\mathrm{sinc}^2(\Delta k L/2) \tag{6.26}$$

where $\Delta k = k_{p1} + k_{p2} - k_{sum}$ is the phase mismatch. It is assumed that $I_{p1} \geq I_{p2}$. The expression for the conversion efficiency with pump depletion is somewhat more complicated:

$$\eta_{sum} = \frac{\lambda_{p2}}{\lambda_s}\,\mathrm{sn}^2[(L/L_{NL}), \gamma\,] \tag{6.27}$$

where

$$L_{NL} = \frac{1}{4\pi d_{eff}} \sqrt{\frac{2\,\varepsilon_0\,n_{p1}\,n_{p2}\,n_s\,c\,\lambda_{p2}\,\lambda_s}{I_{p1}(0)}} \tag{6.28}$$

and

$$\gamma^2 = \frac{\lambda_{p2}\,P_{p2}(0)}{\lambda_{p1}\,P_{p1}(0)} \tag{6.29}$$

Here $\mathrm{sn}(u,\gamma)$ is the so called Jacobi elliptic sine function. The period of this function depends on the so called elliptic modulus, γ. As the modulus goes from 0 to 1, the period goes from 2π to infinity.[48] Since the function is only defined for $0 < \gamma < 1$, equation 6.29 implies that $\lambda_{p1}\,P_{p1}(0) > \lambda_{p2}\,P_{p2}(0)$. Even though the expression for the conversion efficiency seems to be complicated, it can easily be calculated in for instance MATLAB.

6.4.2 Parametric processes

Optical parametric amplification (OPA) is a process in which two waves of different frequencies ω_s and ω_p are interacting, where $\omega_p > \omega_s$, and where the subscript 's' is abbreviation for signal. In the process, one photon of frequency ω_s and one photon of the difference frequency, $\omega_i = \omega_p - \omega_s$, are created from one photon with frequency ω_p. When the intensities of the signal and pump fields are approximately equally large, the process is referred to as *difference frequency generation* (DFG).[51] In that case the subscript 'i', which stands for idler, is usually substituted for 'd', which of course stands for difference, and the signal is usually just referred to as pump 2, abbreviated as 'p2'.

If the pump field is strong enough, there will be a spontaneous effect in which the pump photon is split into one idler photon and one signal photon. The effect is called *optical parametric generation* (OPG) and it requires a quantum mechanical description in order to be explained. Using perturbation theory the spontaneous effect is shown to have its origin in quantum fluctuations, and therefore the outgoing waves will have a spread in angle and hence also in the frequency. In many practical situations this spectral broadening is unwanted. However, the problem can be solved by putting the nonlinear crystal in a mirror cavity, generating a so called *optical parametric oscillation* (OPO). [48]

The OPO cavity can be configured in a number of ways. Firstly, the cavity can be built either as a linear cavity or as a ring cavity. Secondly, the cavity can be chosen to be either singly resonant (SRO), i.e. resonant at either the signal frequency or at the idler frequency, or it can be chosen to be doubly resonant (DRO), i.e. resonant at both the signal and the idler frequencies. The latter gives a lower pump threshold, but requires a more stable setup since its output fluctuates as a consequence of mechanical

vibrations and temperature variations. This is due to the fact that in an OPO, both the energy conservation and the cavity conditions for both the signal and the idler must be fulfilled at the same time, which happens only for frequencies separated by a relative large frequency interval $\Delta\omega$. Hence, for a small length change of the cavity, the frequency might do a large jump. [31, 53]

Because of the demands on the DRO setup, the more simple-to-build SRO is often used. The SRO can be chosen to be resonant either at the signal or the idler wavelength.

Just as a laser, an OPO has a pump threshold. In the case of optimized confocal near-field Gaussian beams, the pump threshold of a signal-resonant SRO can be estimated by the following expression, when the losses are small:

$$P_{p,th} = \frac{\varepsilon_0\, n_s^2\, c\, \lambda_p^3}{\pi^2\, d_{\text{eff}}^2\, L\,(1-\delta^2)}\left(1 - R_s\, e^{-\alpha_s L}\right) \tag{6.30}$$

where R_s is the mirror reflectance for the signal, α_s is the absorption coefficient for the signal and δ is the so called degeneracy factor defined through the following set of equations:

$$\omega_s = \frac{1}{2}\omega_p(1+\delta) \tag{6.31}$$

$$\omega_i = \frac{1}{2}\omega_p(1-\delta) \tag{6.32}$$

For an OPO, the conversion efficiency is defined as:

$$\eta = \frac{P_s + P_i}{P_p(x=0)} \tag{6.33}$$

Here P_s and P_i are the output powers from the OPO and $P_p(x=0)$ is the input pump power. [48]

The total spectral bandwidth of an SRO can be estimated by:

$$\delta\omega_{tot} = \frac{\delta\omega}{\sqrt{N}} \tag{6.34}$$

where $\delta\omega$ is the corresponding gain bandwidth of the OPG process and N is the number of round-trips in the cavity for the resonant wave. In the case of low gain and far away from degeneracy, the gain bandwidth can be calculated through:

$$\delta\omega_s = \frac{5.57c}{L\left|n_s - n_i + \omega_s\frac{\partial n_s}{\partial\omega_s} - \omega_i\frac{\partial n_i}{\partial\omega_i}\right|} \tag{6.35}$$

However, close to degeneracy the following expression must be used:

$$\delta\omega_s = \frac{3.33\sqrt{c}}{\sqrt{L\left(4\frac{\partial n_s}{\partial\omega_s} + \omega_p\frac{\partial^2 n_s}{\partial\omega_s^2}\right)}} \tag{6.36}$$

The bandwidths calculated with the expressions above broaden with the factor $\sqrt{1 + g^2 L^2/\pi^2}$ when the gain is increased towards higher values. [54]

In order to decrease the spectral bandwidth of the signal and the idler from the OPO, different techniques can be used. Some of these are presented in section 7.8. A rather new bandwidth narrowing technique is to use a volume Bragg grating as input or output coupler. A volume Bragg grating has a periodically varying refractive index, $n(z) = n_0 + n_1\cos(2\pi z/\Lambda)$, written into it. The grating period Λ and the deviation θ of the propagation direction from the z-direction, determines the reflected wavelength through the Bragg condition $\lambda_b = 2n_0\Lambda\cos\theta$.[55] The zero-to-zero spectral selectivity of such a grating, in the case $\theta = 0$, can be calculated through:

$$\delta\lambda = \frac{\lambda_0^2\sqrt{(\arctan\sqrt{\eta_0})^2 + \pi^2}}{\pi\, n_0\, L} \tag{6.37}$$

where η_0 is the diffraction efficiency and L is the length of the grating.

6.5 Quasi-phase matching

In the ideal case, the phase velocity of the interacting waves are the same, so that the phase mismatch $\Delta k = 0$, giving the highest possible conversion efficiency. However, waves in crystals suffers from dispersion, meaning that they will travel with different velocities. This will of course significantly reduce the conversion efficiency. Therefore two different techniques have been developed in order to compensate for this mismatch: birefringent phase matching and quasi-phase matching (QPM). In this thesis, quasi-phase matching in KTP crystals have been used.

The strategy of quasi-phase matching is that the sign of the nonlinear coefficient used is reversed every coherence length, L_c, where the coherence length is defined as the distance over which positive conversion occurs in the non-phase matched case. A reverse of the sign has the same effect as introducing a π radians phase shift in the coupled wave equations, which can be realized by making the substitution $d_{\text{eff}} \rightarrow d_{\text{eff}}\, e^{i\pi}$ in the equations.[52, 53] In this way there will be no back-conversion, which is easiest to realize by looking at a plot of the powers of the different fields; comparing the non-phase matched case (d) with the first order quasi-phase matched case (b) in figure 6.2 makes the point clear.

In wave-vector formulation, the quasi-phase matching can be described using the grating vector

$$\mathbf{k}_{\text{mQ}} = \frac{2\pi m}{\Lambda}\,\hat{\mathbf{k}}_{\text{mQ}} \tag{6.38}$$
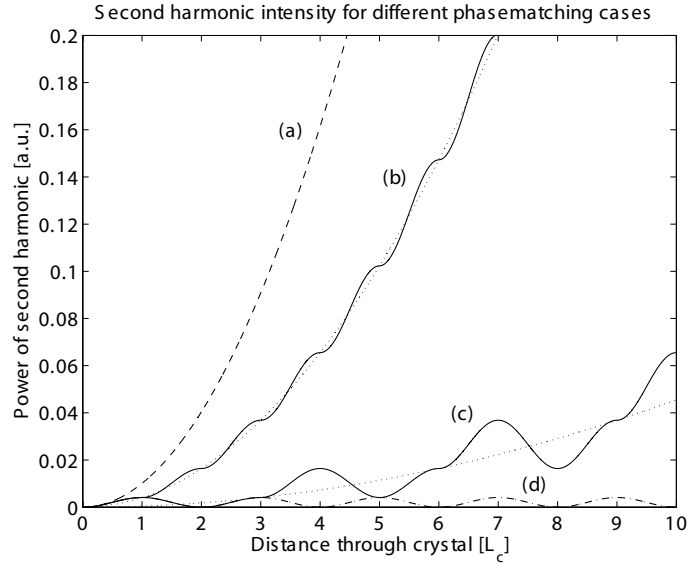
Figure 6.2. *Different phase matching cases. a) Full-phase matching b) First order quasi-phase matching c) Third order quasi-phase matching d) No phase matching. The dotted lines indicates the average growth in the first and third order quasi-phase matched cases respectively.*

where m is the grating order and $\Lambda = 2\,L_c$ is the grating period.[52, 53] With a correctly chosen grating period, zero phase mismatch ($\Delta k = 0$) is obtained. The grating period required in order to obtain zero phase mismatch for a certain process can be determined by considering momentum conservation. For instance a sum frequency process would give the vector equation, $\mathbf{k}_{\mathrm{p1}} + \mathbf{k}_{\mathrm{p2}} + \mathbf{k}_{\mathrm{mQ}} = \mathbf{k}_{\mathrm{sfg}}$, from which the grating period Λ could be determined. The only difficulty is to insert appropriate values of the refractive indices in the equation.

In figure 6.2 both the cases of first and third order quasi-phase matching are plotted. It can be shown that the average growths of the powers of the fields in the quasi-phase matched cases, are the same as the full-phase matched cases, with the following nonlinear coefficients: [48]

$$d_m = \frac{2}{m\pi}\,d_{\mathrm{eff}} \tag{6.39}$$

Since the efficiency is proportional to the square of the nonlinear coefficient, it is easily calculated from the above expression that the efficiency is 9 times higher in the first order quasi-phase matched case than in the third order quasi-phase matched case.

Different techniques have been developed in order to manufacture QPM crystals. In the laser physics group at KTH electric field poling in flux-
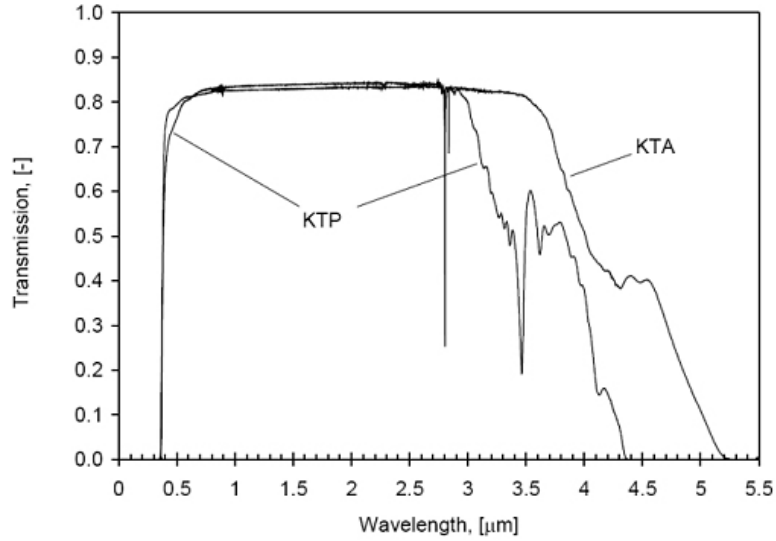
Figure 6.3. *Transmission graphs of a 10.00 mm long KTP crystal and a 10.05 mm long KTA crystal, respectively. Note that Fresnel losses is included in the presented transmissions. [57, 54]*

grown KTP is used. For more information about this and other techniques, see references [52, 56].

6.6 Optical properties of KTP

In the experiments which will be presented in the next chapter, the nonlinear material KTiOPO$_4$ (KTP) has been used. In order to get a deeper understanding of the behavior of this material, its optical properties will be shortly overviewed here.

A transmission curve of KTP, measured with light polarization along the z-axis and beam propagation along the x-axis, can be seen in figure 6.3. In the high transmission region, the absorption is as low as 0.6 %/cm.[54] The general decrease in transmission towards longer wavelengths in the IR-region can be explained by vibrations in the XO$_4$-group. At 2.8 μm there is a strong absorption line origin from a OH$^-$-group.[52] Of course this line should be avoided if possible.

In order to predict the poling period needed for different nonlinear processes, it is necessary to have good models to describe the refractive index variation with respect to certain parameters. The dispersion is often described using the two-poled Sellmeier equation:

$$n^2(\lambda) = A + \frac{B}{1 - C\,\lambda^{-2}} + \frac{D}{1 - E\,\lambda^{-2}} - F\lambda^2 \qquad (6.40)$$

where the wavelength λ should be given in μm. The constants are found by fitting the model to measurement data. Since it is quite hard to obtain values on the parameters, which accurately describes the dispersion over a wide range, it is a good idea to use different parameters for different wavelength regions. For longer wavelengths than 1 μm a Sellmeier equation described by Fradkin et al [58] models the dispersion quite accurate. For shorter wavelengths than 1 μm an equation published by Fan et al [59] works better. The Sellmeier coefficients for these models are found in table 6.2. [54, 52] Another commonly used set of Sellmeier coefficients has been presented by Kato et al [60].

Coefficient	Unit	Fan et al	Fradkin et al
A	-	2.25411	2.12725
B	-	1.06543	1.18431
C	μm^2	0.05486	0.0514852
D	-	0	0.6603
E	μm^2	0	100.00507
F	μm^{-2}	0.02140	0.00968956

Table 6.2. *Sellmeier coefficients for n_z in KTP. Model by Fan et al should be used when $\lambda < 1\,\mu m$ and model by Fradkin et al should be used when $\lambda > 1\,\mu m$.*

By changing the temperature both the refractive index and the length of the crystal changes. This means that it is possible to temperature tune the poling period and hence the phase matching condition. The temperature dependence of the refractive index can be described by the following formula:

$$\frac{dn_z}{dT} = \frac{p_1}{\lambda^3} + \frac{p_2}{\lambda^2} + \frac{p_3}{\lambda} + p_4 \tag{6.41}$$

Wiechmann et al [61] has presented coefficients for this formula which accurately describes the behavior for $\lambda < 1\,\mu m$, see table 6.3. In order to describe the temperature dispersion for longer wavelengths a model introduced by Ghosh [62] can be used: [54]

$$2n_z\frac{dn_z}{dT} = GR + HR^2 \tag{6.42}$$

where

$$R = \frac{\lambda^2}{\lambda^2 - \lambda_{ig}^2} \tag{6.43}$$

Values of the coefficients G, H and λ_{ig} for KTP can be found in table 6.3.

The thermal expansion of the material in the propagation direction, the x-axis, can be described by a second order polynomial:

Wiechmann et al			Ghosh		
Coefficient	Unit	Value	Coefficient	Unit	Value
p_1	$\mu m^3 \, ^\circ C^{-1}$	12.415E-6	G	$^\circ C^{-1}$	-7.4595E-6
p_2	$\mu m^2 \, ^\circ C^{-1}$	-44.414E-6	H	$^\circ C^{-1}$	52.9338E-6
p_3	$\mu m \, ^\circ C^{-1}$	59.129E-6	λ_{ig}	μm	0.279
p_4	$^\circ C^{-1}$	-12.101E-6			

Table 6.3. *Coefficients for the temperature dispersion model in the case of KTP. The model described by Wiechmann et al gives accurate results for $\lambda < 1.064 \, \mu m$ and the model introduced by Ghosh provides a good description when $\lambda > 1.064 \, \mu m$.*

$$L = L_0[1 + \alpha(T - 25) + \beta(T - 25)^2] \tag{6.44}$$

where L is the crystal length at T degrees Celsius and L_0 is the crystal length at 25 degrees Celsius. Emanueli et al [63] have determined the coefficients α and β for KTP to $(6.7\pm0.7)\cdot10^{-6} \, ^\circ C^{-1}$ and $(11\pm2)\cdot10^{-9} \, ^\circ C^{-2}$, respectively.

The last optical property to be presented is the *d*-coefficient. KTP belongs to the point group of symmetry mm2 and therefore the reduced nonlinear tensor only consists of five non-zero elements:

$$d_{il} = \begin{pmatrix} 0 & 0 & 0 & 0 & 1.91 & 0 \\ 0 & 0 & 0 & 3.64 & 0 & 0 \\ 2.52 & 4.35 & 16.9 & 0 & 0 & 0 \end{pmatrix} \quad [\text{pm/V}] \tag{6.45}$$

6.7 SNLO software

Computer simulations are necessary in order to make good estimations of the outcome of nonlinear systems. However, such simulations tends to be very complicated if for instance group velocity effects and bandwidth are accounted for. In the frame of this thesis there is no time to write such a program. Instead a nonlinear optics toolbox, called SNLO, developed by Arlee V. Smith at Sandia National Laboratories, US, will be used. This software is free to download at Sandia's webpage.[64] SNLO includes a number of different functions, for instance there are functions to simulate long pulse, short pulse and broadband OPO:s. The program also includes a large data base over nonlinear materials based on around 600 papers. [65]

7 Frequency conversion stage

In this chapter, the frequency conversion stage will be examined in detail. First different possible setups based on a source emitting around 1064 nm will be presented and discussed. Then simulations performed in the software SNLO will be described. The aim of the simulations was to find the most efficient system. Based on the results from these simulations, one system was chosen to be experimentally realized. A number of experiments have been done on the chosen system. These will be presented in chapter 7.6, followed by discussions and further improvements of the setup.

7.1 Possible setups

If an infrared pump source emitting at approximately 1064 nm is used, then many different frequency conversion schemes are possible. Here some of the most useful setups are going to be presented. All systems are assumed to use periodically poled KTP (PPKTP) crystals, since these type of crystals were available in the lab.

The first setup is visualized in figure 1(a). It starts with a SHG process generating green at 532 nm. The outgoing second harmonic is then sent into an OPO which produces a signal and an idler. For a certain poling period it is possible to obtain a signal at 920.8 nm and an idler at 1260 nm. Both of these are then frequency doubled in two separate crystals giving red at 630.0 nm and blue at 460.4 nm. A similar scheme has been described by Paschotta [8]. However, no performance data of the system is given in the reference. Moulton et al [15] also described a quite similiar scheme pumped with an acustooptically Q-switched Nd:YLF laser emitting at 1047 nm with a pulse repetition frequency of 22 kHz. They obtained a total output power of 15 W of white light D65, when pumping the OPO with 30 W of radiation at 524 nm.

A second system is depicted in figure 1(b). As the former setup, this system also starts with a SHG process generating green at 532 nm. Again the second harmonic is sent into an OPO, however this time the OPO crystal has a completely different poling period, which generates a red signal at approximately 634.5 nm and an idler at approximately 3293 nm. The green and idler is then sum frequency mixed in a third crystal giving blue at 458 nm. A similiar scheme has earlier been proposed and tested by Gao et al [16]. They obtained an output power of 394 mW of white light D58, when pumping the OPO with 1 W of radiation at 532 nm (at a pulse repetition frequency of 4 kHz).

A third setup is sketched in figure 1(c). Here the infrared light at 1064 nm is split up into two beams. One of the beams is sent into an OPO generating a signal at approximately 1572 nm and an idler at approximately 3293 nm. In the crystal denoted by three in the figure, the infrared at 1064 nm and the
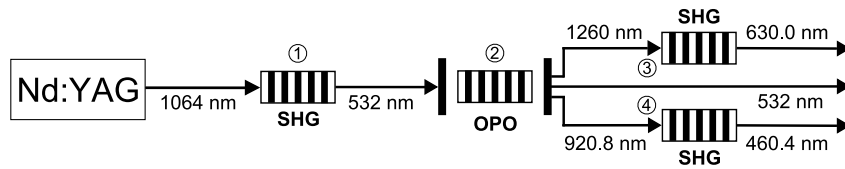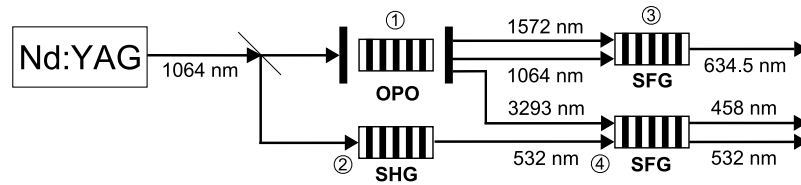
(a) *System 1. Simple and straightforward scheme, but requires four different crystals.*
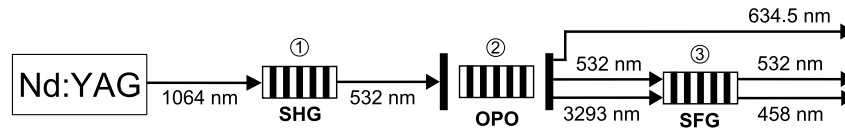
(b) *System 2. This system only requires three crystals, which is a big advantage considering the cost aspect. The sum frequency process can either be done in intra-cavity or in extra-cavity mode.*

(c) *System 3. The big advantage of this system is the possibility to steer the fractions of the incoming light which should be sent into crystal one and two. However, four crystals and a beam splitter is needed.*

Figure 7.1. *Overview of the different system configurations. The numbers in the circles are just crystal labels.*

signal is sum frequency mixed giving red at 634.5nm. The other beam from the laser source is frequency doubled generating green at 532 nm. In crystal four, the green and idler from the OPO is sum frequency mixed generating blue at 458 nm.[66]

A fourth possible setup (not drawn in figure 7.1), described by Henrich et al [14], will only be briefly discussed here. The system starts with a SHG process generating green. The remaining energy at the fundamental wavelength is pumping an OPO, producing a signal around 1530 nm, which is sum frequency mixed with the fundamental in a third crystal giving red. Finally blue is generated by sum frequency mixing between the remaining signal and the red radiation. Henrich et al pumped their system with a mode-locked Nd:YVO$_4$ laser emitting pulses with a repetition frequency of 80 MHz. In total they obtained an output power of 19 W of white light, when pumping the Nd:YVO$_4$ crystal with 110 W at 808 nm. This scheme will not be treated further in this diploma thesis, because of the predicted difficulty of obtaining high power at the blue wavelength.

7.2 Wavelength selection and power balancing

The selection of the red and blue wavelengths of the RGB systems will be based on three important aspects. First of all it is desirable to choose the wavelengths so that the triangle spanned in the CIE diagram, figure 2.4, becomes as large as possible. Secondly the sensitivity of the eye (figure 2.2 and 3(b)) at these wavelengths should not be too low, because then too high powers at these wavelengths would be needed, and since the powers of the red and blue wavelengths probably will be the limitations of the systems this is an important aspect. A third aspect is the transmission in KTP at long wavelengths; at certain frequencies the transmission drops to very low values, see figure 6.3, and of course these frequencies should be avoided.

The frequencies of the red and the blue beams can be found by considering energy relations. For system 1 the following must hold:

$$\omega_{green} = 2\,\omega_{laser} \tag{7.1}$$

$$\omega_{red} = 2\,\omega_{idler} \tag{7.2}$$

$$\omega_{blue} = 2\,(\omega_{green} - \omega_{idler}) \tag{7.3}$$

Inserting equation 7.1 into equation 7.2, and using $\omega = 2\pi c/\lambda$, gives the following expressions:

$$\lambda_{red} = \lambda_{idler}\Big/2 \tag{7.4}$$

$$\lambda_{blue} = 1\Big/\left(2\left(\frac{2}{\lambda_{laser}} - \frac{1}{\lambda_{idler}}\right)\right) \tag{7.5}$$
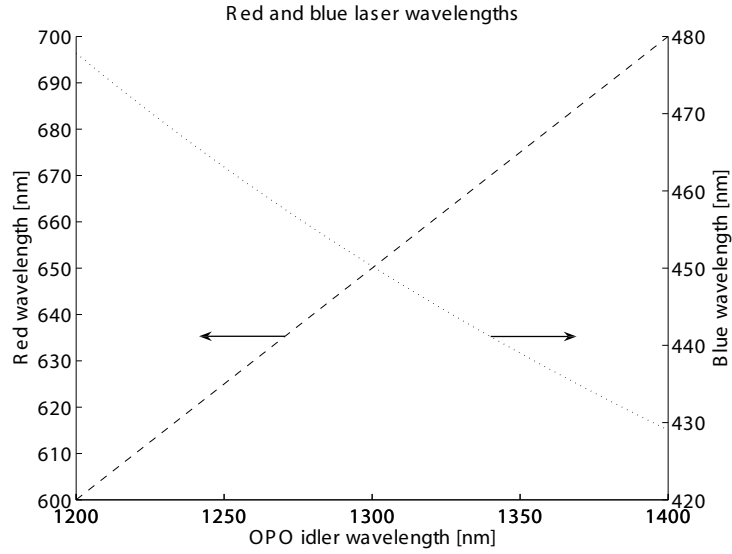
Figure 7.2. *The red and blue wavelengths as function of the idler wavelength for system 1.*

In figure 7.2 the red wavelength λ_{red} and the blue wavelength λ_{blue} are plotted as function of the idler wavelength λ_{idler}. Including this diagram, all tools needed for the wavelength selection have now been presented. Considering the CIE diagram, figure 2.4, the red wavelength should be as long as possible and the blue wavelength as short as possible. The curves in figure 7.2 shows that this means using as long idler wavelength as possible. However, by looking at the sensitivity curves of the eye, it can be seen that it would not be good to go for longer wavelengths than $\lambda_{red} = 630$ nm since the sensitivity then becomes too small. If $\lambda_{red} = 630$ nm, then $\lambda_{idler} = 1260$ nm and $\lambda_{blue} = 460.4$ nm. The blue wavelength thus becomes close to the sensitivity maximum for the blue sensors which of course is very good. Note that the transmission of KTP does not restrict the choice of the wavelengths in this case, because the idler is in the high transmission region.

Energy considerations for system 2 generate the following set of frequency relations:

$$
\begin{aligned}
\omega_{green} &= 2\,\omega_{laser} & (7.6) \\
\omega_{red} &= \omega_{green} - \omega_{idler} & (7.7) \\
\omega_{blue} &= \omega_{green} + \omega_{idler} & (7.8)
\end{aligned}
$$

Putting equation 7.6 into equations 7.7 and 7.8, and using $\omega = 2\pi c/\lambda$, gives:

66

$$\lambda_{red} \;=\; 1\left/\left(\frac{2}{\lambda_{laser}} - \frac{1}{\lambda_{idler}}\right)\right. \qquad (7.9)$$

$$\lambda_{blue} \;=\; 1\left/\left(\frac{2}{\lambda_{laser}} + \frac{1}{\lambda_{idler}}\right)\right. \qquad (7.10)$$

A plot of the red and blue wavelengths as function of the idler wavelength is found in figure 7.3. In this case, the limiting factor of which wavelengths which can be chosen is the transmission of the idler in KTP. From figure 6.3 it is obvious that the idler should not be chosen higher than $\lambda_{idler} = 3400$ μm, because there is a big dip in the transmission at $\lambda = 3500$ μm. If the blue wavelength is chosen to be $\lambda_{blue} = 458$ nm, then the idler wavelength becomes $\lambda_{idler} = 3293$ nm, which gives some safety margin to the dip. Even though the material is partly absorbing at $\lambda_{idler} = 3293$ nm, the absorption is believed to be of not so large importance because of the strong amplification of the signal and idler caused by the high non-linear coefficient of the periodically poled medium. Of course it would have been better to have chosen a more transparent material at these wavelengths. However, for these experiments only KTP crystals were available.

With an idler at $\lambda_{idler} = 3293$ nm, the red wavelength is calculated to be $\lambda_{red} = 634.5$ nm, which gives a little bit lower response by the eye than $\lambda_{red} = 630$ nm, which was the wavelength chosen for the former system. However, the sensitivity is still strong enough.

For the last system, the following expressions are found for the frequencies:

$$\omega_{green} \;=\; 2\,\omega_{laser} \qquad (7.11)$$

$$\omega_{red} \;=\; (\omega_{laser} - \omega_{idler}) + \omega_{laser} \qquad (7.12)$$

$$\omega_{blue} \;=\; \omega_{green} + \omega_{idler} \qquad (7.13)$$

which gives the same wavelength relations as obtained for system 2:

$$\lambda_{red} \;=\; 1\left/\left(\frac{2}{\lambda_{laser}} - \frac{1}{\lambda_{idler}}\right)\right. \qquad (7.14)$$

$$\lambda_{blue} \;=\; 1\left/\left(\frac{2}{\lambda_{laser}} + \frac{1}{\lambda_{idler}}\right)\right. \qquad (7.15)$$

Since the same set of equations have been discussed above, also the results from system 2 hold. Hence, the red wavelength should be $\lambda_{red} = 634.5$ nm and the blue wavelength should be $\lambda_{blue} = 458$ nm.

The optimizations performed in this chapter were not strictly mathematical. A such mathematical treatment would of course have been interesting, and could be a topic for future work.
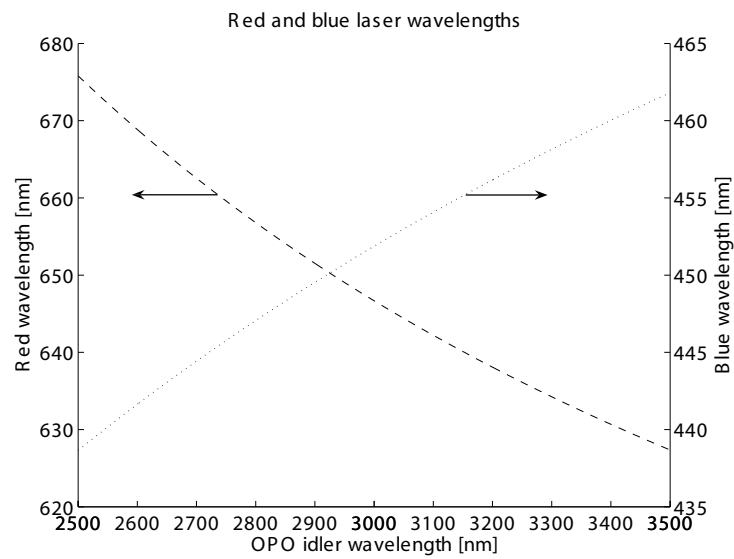
Figure 7.3. *The red and blue wavelengths as function of the idler wavelength for system 2 and system 3.*

Finally the color balanced power ratios for the different systems are calculated using equation 2.12. They are found to be 1 : 0.8226 : 0.6593, 1 : 0.7298 : 0.5575 and 1 : 0.7298 : 0.5575 for system 1, system 2 and system 3, respectively.

7.3 Efficiency simulations in SNLO

To estimate which system is most efficient, simulations have been performed in the software SNLO described in chapter 6.7. For the OPO:s, the function 2D-OPO-LP was used and for the SHG and SFG processes the function 2D-mix-LP was utilized. These functions do not take into account group velocity effects, which are of importance for short pulses below the nanosecond regime and for pulses with broad bandwidth.[65]

7.3.1 Laser source and simulation assumptions

The laser source was assumed to be a q-switched laser with the following charachteristics:

Repetition frequency	18 kHz
Average power	7.57 W
Pulse energy	420 μJ
Peak power	11 kW
Pulse length	38.3 ns

Table 7.1. *Simulated laser data used as in-data for the SNLO simulations.*

These data has directly been taken from a simulation conducted in MATLAB on the diode pumped Nd:YVO$_4$ laser described in section 5. Note that the pulse width is rather long - approximately 38 ns. For good actively Q-switched devices, the pulse length can of course be made much shorter.

In the simulations, all pulse shapes were assumed to be Gaussian, due to the fact that SNLO only accepts Gaussian inputs. The OPO-mirrors were chosen to be flat, except in system 3 where curved mirrors were needed in order to get a non-diverging simulation. Furthermore, the beam radiuses were set to $w = 200$ μm in all crystals, except in the OPO in system 3, where the pump focus was set to $w = 125$ μm. The fact that the same focus were used in all crystals is of course a simplification, because the processes are nonlinear, and therefore it will be possible to obtain more efficient results than those presented below. However, the results will anyway give a hint of how efficient the systems are.

In the simulations, the PPKTP crystals were set to have an effective nonlinear coefficient $d_{eff} = 9$ pm/V and a crystal length $L_{eff} = 11$ mm. The refractive indices for the different wavelengths were partly found using the "Ref. Ind." function in SNLO and partly found using a program written in MATLAB, based on the three different Sellmeier equations presented in section 6.6.

7.3.2 Setup 1

The first process in system 1 is a SHG process generating power at 532 nm from the fundamental at 1064 nm. In table 7.2 the input and output data of the simulation of this process is presented. Using these data, the conversion efficiency is calculated to be 59.5 %.

The next step is the OPO process pumped with the second harmonic at 532 nm from the first process. In this case, the OPO cavity is set to be singly resonant at the signal wavelength 632.5 nm, with a reflectance of 99 % at the incoupling mirror. Since it is quite interesting to know which outcoupling reflectance which gives the maximum conversion, the output energy from the OPO has been calculated for different reflectances, see figure 7.4.
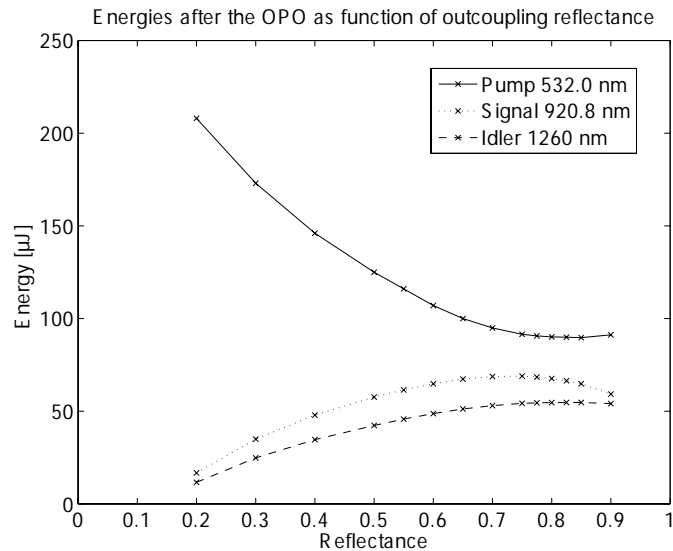

Figure 7.4. *The output energies from the OPO as function of the outcoupling reflectance. The marked points are data from the simulations.*

From the diagram, the reflectance is chosen to be R=77.5 %. This gives the outgoing pulse charchteristics shown in table 7.3, if the mirror losses at the other wavelengths are set to 4 %.

The output pulses from the OPO with the wavelengths 920.8 nm and 1260 nm are then put into the next simulation steps: the two SHG processes. The input and output data of these simulations are presented in table 7.4 and table 7.5. From the presented data, the conversion efficiency for process 3 and 4 is calculated to be 22.9 % and 37.6 %, respectively.

The average output powers of the red, green and blue beams are calculated to be 0.23 W, 1.63 W and 0.46 W, respectively, which gives an *overall efficiency* of 30.6 %. Note however that the overall efficiency, defined as the

System 1, Process 1		Unit	Input	Output
Pulse energy, fundamental	E_f	μJ	420	90.6
Pulse energy, second harmonic	E_{sh}	μJ	0	250
Pulse length, fundamental	τ_f	ns	38.3	69.0
Pulse length, second harmonic	τ_{sh}	ns	-	34.4
Peak power, fundamental	$\hat{P}_f$	kW	11	1.27
Peak power, second harmonic	$\hat{P}_{sh}$	kW	-	6.94

Table 7.2. *Input and output data from the simulation of the SHG process in crystal 1 of system 1. ($\lambda_{fundamental} = 1064$ nm, $\lambda_{second\ harmonic} = 532$ nm)*

System 1, Process 2		Unit	**Pump**	Signal	Idler
Pulse energy	E_{pulse}	μJ	**90.6**	68.4	54.5
Pulse length	τ	ns	26	28.5	27.4
Peak power	$\hat{P}$	kW	4.84	2.48	1.98

Table 7.3. *Output pulse charachteristics from the OPO in system 1. ($\lambda_{pump} = 532$ nm, $\lambda_{signal} = 920.8$ nm, $\lambda_{idler} = 1260$ nm)*

System 1, Process 3		Unit	Input	Output
Pulse energy, fundamental	E_f	μJ	54.5	32.6
Pulse energy, second harmonic	E_{sh}	μJ	0	**12.5**
Pulse length, fundamental	τ_f	ns	27.4	31.2
Pulse length, second harmonic	τ_{sh}	ns	-	21.4
Peak power, fundamental	$\hat{P}_f$	kW	1.98	0.98
Peak power, second harmonic	$\hat{P}_{sh}$	kW	-	0.56

Table 7.4. *Input and output data from the simulation of the SHG process in crystal 3 of system 1. ($\lambda_{fundamental} = 1260$ nm, $\lambda_{second\ harmonic} = 630$ nm)*

System 1, Process 4		Unit	Input	Output
Pulse energy, fundamental	E_f	μJ	68.4	31.2
Pulse energy, second harmonic	E_{sh}	μJ	0	**25.7**
Pulse length, fundamental	τ_f	ns	28.5	33.6
Pulse length, second harmonic	τ_{sh}	ns	-	25.6
Peak power, fundamental	$\hat{P}_f$	kW	2.48	0.81
Peak power, second harmonic	$\hat{P}_{sh}$	kW	-	1.06

Table 7.5. *Input and output data from the simulation of the SHG process in crystal 4 of system 1. ($\lambda_{fundamental} = 920.8$ nm, $\lambda_{second\ harmonic} = 460.4$ nm)*

sum of the the outgoing red, green an blue powers diveded by the total pump power, does not tell how much of the pump power that can be transformed into white light. Instead a new efficiency parameter need to be introduced, which only compares the total red, green and blue powers, which can be used to generate white light D65, with the pump power. This efficiency will be called *effective efficiency* from hereon. Using the power ratios from chaper 7, the effective effiency is calculated to 7 %. The red light was the limiting factor.

7.3.3 Setup 2

The first process step of setup 2 is the same as in setup 1, i.e. a SHG process generating green at 532 nm. Again the second harmonic is used to pump an OPO, however this time with a crystal poling period generating a signal at 632.5 nm and an idler at 3293 nm. As mentioned earlier, the SFG process can be done either in extra-cavity mode or in intra-cavity mode. The intra-cavity mode cannot directly be simulated in SNLO, but one could always simulate a regular OPO and introduce losses at 532 nm and at 3293 nm in order to compensate for the extra crystal in the cavity. It is important to notice that this method does not give a fully correct description of the system, because the processes are nonlinear and the losses are linear. For accuracy and simplicity only the extra-cavity mode configuration has therefore been simulated.

As in system 1, the output energies were calculated for different out-coupling reflectances, holding the incoupling mirror reflectivity constant at 99 %. The result is shown in figure 7.5, where it can be seen that the maximas of the idler and signal energy are not localized at the same reflectance and therefore a compromise must be accepted; choosing the reflectance to 92.5 % seems reasonable. For this reflectance, the output pulse charachteristics in table 7.7 is obtained.

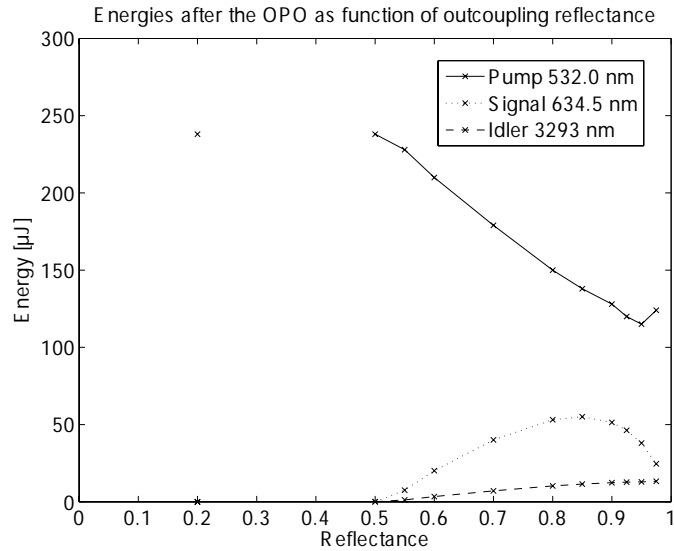Furtheron the outgoing idler and green is sum frequency mixed in the

Figure 7.5. *The output energies from the OPO as function of the out-coupling reflectance. The marked points are data from the simulations.*

third crystal generating blue. The input and output parameters for the corresponding simulation can be found in table 7.8.

Finally the average output powers for the red, green and blue beams are calculated to 0.84 W, 1.22 W and 0.61 W, respectively. This gives an overall efficiency of 35 % and an effective efficiency of 25 %. Again the red light was the limiting factor.

7.3.4 Setup 3

Setup 3 can physically be configured in different ways. One compact way of doing it, is to put the crystals after each other in the order 1, 3, 2 and 4. A setup with beam splitters would probably be more efficient, due to the fact that it is possible to control the output energies more videly, and hence not as much energy would be lost later during the power balancing. However, a system with seperate beams is more complicated to build and therefore the compact system without beamsplitters will be simulated here.

In contrast to the other systems above, the OPO in this system is directly pumped with the pump source at 1064 nm. To get a converging simulation, curved mirrors are needed in this case; two mirrors with radius of curvature 100 mm are selected, which seems to work fine. Again the output energies for different output mirror reflectances have been plotted, see figure 7.6. It is important to realize that the best RGB output is not given for the maximum conversion in the OPO. This is partly because the idler from the

System 2, Process 1		Unit	Input	Output
Pulse energy, fundamental	E_f	μJ	420	90.6
Pulse energy, second harmonic	E_{sh}	μJ	0	250
Pulse length, fundamental	τ_f	ns	38.3	69.0
Pulse length, second harmonic	τ_{sh}	ns	-	34.4
Peak power, fundamental	$\hat{P}_f$	kW	11	1.27
Peak power, second harmonic	$\hat{P}_{sh}$	kW	-	6.94

Table 7.6. *Input and output data from the simulation of the SHG process in crystal 1 of system 2. ($\lambda_{fundamental} = 1064$ nm, $\lambda_{second\ harmonic} = 532$ nm)*

System 2, Process 2		Unit	Pump	Signal	Idler
Pulse energy	E_{pulse}	μJ	124	**46.4**	12.7
Pulse length	τ	ns	20.0	20.5	21.0
Peak power	$\hat{P}$	kW	6.16	0.69	2.26

Table 7.7. *Output pulse charachteristics from the OPO in system 2. ($\lambda_{pump} = 532$ nm, $\lambda_{signal} = 634.5$ nm, $\lambda_{idler} = 3293$ nm)*

System 2, Process 3		Unit	Input	Output
Pulse energy, fundamental 1	$E_{f,1}$	μJ	124	**67.8**
Pulse energy, fundamental 2	$E_{f,2}$	μJ	12.7	2.4
Pulse energy, sum	E_{sh}	μJ	0	**33.9**
Pulse length, fundamental 1	$\tau_{f,1}$	ns	20	24
Pulse length, fundamental 2	$\tau_{f,2}$	ns	21	30.2
Pulse length, sum	τ_{sh}	ns	-	18.9
Peak power, fundamental 1	$\hat{P}_{f,1}$	kW	6.16	2.94
Peak power, fundamental 2	$\hat{P}_{f,2}$	kW	0.69	0.32
Peak power, sum	$\hat{P}_{sh}$	kW	-	1.84

Table 7.8. *Input and output data from the simulation of the SFG process in crystal 3 of system 2. ($\lambda_{fundamental\ 1} = 532$ nm, $\lambda_{fundamental\ 2} = 3293$ nm, $\lambda_{sum} = 458$ nm)*

OPO, which is used in the summation process in the last crystal, do not need to be of high energy in comparsion to the other beam at 532 nm to which it is summed, and partly because the red becomes too strong compared to the other colors if the conversion in the OPO is too high. After some investigation, $R = 60$ % seems to be the best choice. The output pulse charchteristics for this reflectance is shown in table 7.9.
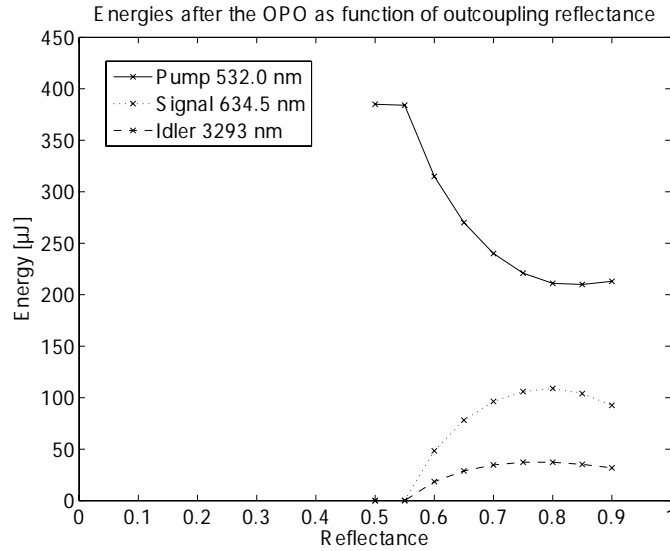

Figure 7.6. *The output energies from the OPO as function of the out-coupling reflectance. The marked points are data from the simulations.*

The simulations for the last three processes are straightforward and their results are shown in table 7.10, 7.11 and 7.12, respectively. From these data, the average ouput powers are calculated to be 1.24 W at red, 1.08 W at green and 0.57 W at blue. This gives an overall efficiency of 38 % and an effective efficiency of 29 % for white light D65. The blue light was the limiting factor.

System 3, Process 1		Unit	**Pump**	**Signal**	**Idler**
Pulse energy	E_{pulse}	μJ	315	48.0	18.3
Pulse length	τ	ns	28.7	11.9	11.5
Peak power	$\hat{P}$	kW	9.43	4.36	1.64

Table 7.9. *Output pulse charchteristics from the OPO in system 3. ($\lambda_{pump} = 1064$ nm, $\lambda_{signal} = 1572$ nm, $\lambda_{idler} = 3293$ nm)*

System 3, Process 2		Unit	Input	Output
Pulse energy, fundamental 1	$E_{f,1}$	μJ	315	220
Pulse energy, fundamental 2	$E_{f,2}$	μJ	48.0	11.6
Pulse energy, sum	E_{sh}	μJ	0	**68.7**
Pulse length, fundamental 1	$\tau_{f,1}$	ns	28.7	34.4
Pulse length, fundamental 2	$\tau_{f,2}$	ns	11.9	13.8
Pulse length, sum	τ_{sh}	ns	-	12.1
Peak power, fundamental 1	$\hat{P}_{f,1}$	kW	9.43	6.06
Peak power, fundamental 2	$\hat{P}_{f,2}$	kW	4.36	0.82
Peak power, sum	$\hat{P}_{sh}$	kW	-	5.66

Table 7.10. *Input and output data from the simulation of the SFG process in crystal 3 of system 3. ($\lambda_{fundamental\ 1} = 1064$ nm, $\lambda_{fundamental\ 2} = 1572$ nm, $\lambda_{sum} = 634.5$ nm)*

System 3, Process 3		Unit	Input	Output
Pulse energy, fundamental	E_f	μJ	220	67.8
Pulse energy, second harmonic	E_{sh}	μJ	0	112
Pulse length, fundamental	τ_f	ns	34.4	55.8
Pulse length, second harmonic	τ_{sh}	ns	-	33.0
Peak power, fundamental	$\hat{P}_f$	kW	6.06	1.28
Peak power, second harmonic	$\hat{P}_{sh}$	kW	-	3.61

Table 7.11. *Input and output data from the simulation of the SHG process in crystal 2 of system 3. The efficiency of the process is calculated to be 50.9 %. ($\lambda_{fundamental} = 1064$ nm, $\lambda_{second\ harmonic} = 532$ nm)*

System 3, Process 4		Unit	Input	Output
Pulse energy, fundamental 1	$E_{f,1}$	μJ	112	**59.8**
Pulse energy, fundamental 2	$E_{f,2}$	μJ	18.3	5.30
Pulse energy, sum	E_{sh}	μJ	0	**31.7**
Pulse length, fundamental 1	$\tau_{f,1}$	ns	33.0	43.6
Pulse length, fundamental 2	$\tau_{f,2}$	ns	11.5	9.9
Pulse length, sum	τ_{sh}	ns	-	13.9
Peak power, fundamental 1	$\hat{P}_{f,1}$	kW	3.61	1.61
Peak power, fundamental 2	$\hat{P}_{f,2}$	kW	1.64	0.48
Peak power, sum	$\hat{P}_{sh}$	kW	-	2.23

Table 7.12. *Input and output data from the simulation of the SFG process in crystal 4 of system 3. ($\lambda_{fundamental\ 1} = 532$ nm, $\lambda_{fundamental\ 2} = 3293$ nm, $\lambda_{sum} = 458$ nm)*

7.3.5 Simulation results

The results from the simulations are summarized in table 7.13.

		System 1	System 2	System 3
Total powers [W]	R	0.23	0.84	1.24
	G	1.63	1.22	1.08
	B	0.46	0.61	0.57
Balanced powers [W]	R	0.23	0.84	0.87
	G	0.19	0.61	0.79
	B	0.15	0.47	0.57
Overall efficiency		31 %	35 %	38 %
Effective efficiency		7 %	25 %	29 %

Table 7.13. *Summary of the results from the SNLO simulations. The balanced powers gives white light D65.*

7.3.6 Discussion of the simulations

Without testing the systems in reality it is hard to make a good accuracy analysis of the simulations. However, it seems that the conversion efficiencies of the OPO simulations are a little bit too high. This can be a result of that losses from back conversion and losses from group velocity dispersion effects were neglected in the simulations.

The conversion efficiencies of the SHG and SFG processes seem to be reasonable. For instance the conversion efficiency of a SHG process from 1064 nm to 532 nm is normally somewhere between 50% and 65 %, which can be compared to the found value of 59.5 %.

7.4 General discussion of system setups

When deciding which system to use there are two important factors to consider: cost and power efficiency. The costs of the systems are very dependent on the number of periodically poled crystals used, since these are very expensive. This means that system 2 would most probably be the least expensive system.

From an efficiency point of view, system 3 seems to be the best choice according to the simulation results above. However, when referring to the results above, one must remember that the three primaries were white balanced by simply scaling the output powers after the frequency conversion stage. However, there are more efficient methods which can be used in order to obtain a balanced output. Firstly, the conversion efficiency of the nonlinear process in each crystal can be controlled either by using crystals

of different lengths or by adjusting the focus of the beams in each of the crystals. Secondly, beam splitters can be used in some systems in order to control the energy flow through the system. In system 3 for instance, a dichroic mirror can be used to control the distribution of the incoming energy from the laser source between crystal one and crystal two. In system 2, one could put a dichroic mirror after the OPO in order to reflect off some of the energy at 532 nm. However, in reality it has been shown that there will be enough green power, even though no beam splitter is used. The method is not applicable to system 1 at all. When considering the additional color balancing methods now presented, system 3 still seems to have the largest possibility of achieving highest conversion efficiency.

Since the expected efficiency of system 2 and system 3 do not differ very much, and since the expected cost for system 2 is smaller than for system 3, system 2 seems to be the best compromise between cost and efficiency. Periodically poled crystals suitable for system 2 were also available in the lab.

7.5 Calculation of the grating periods

In this section, the poling period of the crystals needed in the OPO and SFG processes in system 2 will be calculated. The grating period of the SHG crystal will not be calculated here, since it has been well examined earlier ($\Lambda_g = 9.01$ μm).[67] As a starting remark it should be mentioned that, in order to make the experiments as simple as possible, collinear processes will be used. The momentum equation for a collinear OPO process is a scalar equation:

$$k_s + k_i + k_Q = k_p \tag{7.16}$$

This expression can be rewritten as

$$\frac{\omega_s\,n_s}{c} + \frac{\omega_i\,n_i}{c} + \frac{2\,\pi}{\Lambda_g} = \frac{\omega_p\,n_p}{c} \tag{7.17}$$

By using this equation and the equation for energy conservation, $\omega_p = \omega_s + \omega_i$, the grating period can be calculated. In theory the calculations are very straightforward. However, in order to obtain an accurate value of the grating period, appropriate numbers of the refractive indices must be inserted. Since the Sellmeier equations just models the reality, there will be a certain error in the calculated grating period. In figure 7.7, the signal and idler wavelengths have been plotted as function of the grating period for different cases, using different Sellmeier equations. As can be seen, the result far away from the degeneracy point is very dependent on which Sellmeier equation which has been used. The best way to determine the poling period might be to use Fradkin's Sellmeier equation [58] for wavelengths longer than 1 μm and Fan's Sellmeier equation [59] for wavelengths shorter than 1 μm. The solid line in
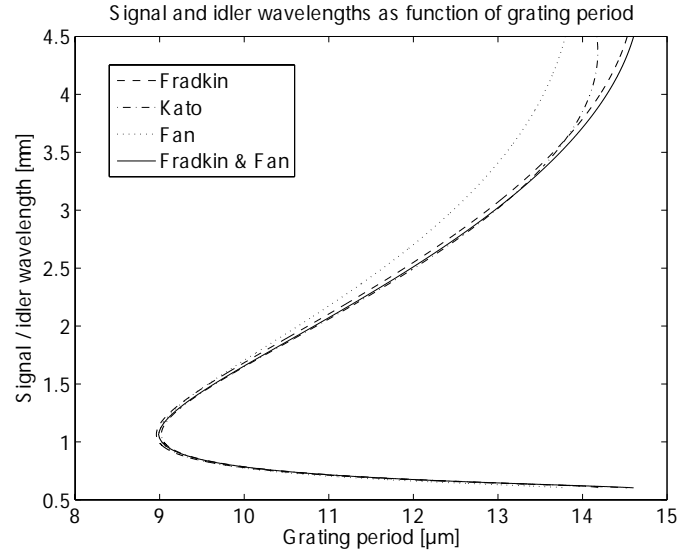
78

Figure 7.7. *The signal and idler wavelengths of the OPO as function of the grating period, calculated using three different Sellmeier equations. [58, 59, 60] The solid line represents a calculation using Fradkin's Sellmeier equation above 1 μm and Fan's Sellmeier equation below 1 μm.*

figure 7.7 represents the result of such a calculation. From this graph, the grating period needed in order to obtain a signal at 634.5 nm and an idler at 3293 nm is determined to be 13.44 μm.

For a SFG process the momentum equation takes the following form:

$$k_{p1} + k_{p2} + k_Q = k_{sum} \tag{7.18}$$

which can be rephrased as

$$\frac{\omega_{p1}\, n_{p1}}{c} + \frac{\omega_{p2}\, n_{p2}}{c} + \frac{2\,\pi}{\Lambda_g} = \frac{\omega_{sum}\, n_{sum}}{c} \tag{7.19}$$

Using this equation and the equation for energy conservation, the grating period required in order to obtain a phase matched sum frequency process between two pump beams, with the wavelengths 532 nm and 3293 nm, respectively, is calculated to be 9.38 μm (when the refractive indices are determined from Fradkin's and Fan's Sellmeier equations).

7.6 Primary experiments

In the following subsections, system 2 will be examined in detail through a number of experiments which have been performed in the lab. First temperature tuning measurements on the available periodically poled crystals will be presented. Then results from pump depletion measurements, beam quality measurements and spectrum measurements follows.

7.6.1 General experimental setup

The experiments in this section were performed using a flash-lamp-pumped Nd:YAG laser (New wave research's Minilase I/20 Hz), with pulse repetition frequency 20 Hz and 5 ns pulses. The laser could be internally frequency-doubled to produce light at 532 nm. Since this was possible, the first step of system 2 was not built; the SHG step has earlier been well examined in a number of papers and therefore the effort was put on investigating the two last steps, which do not deal with standard-wavelength conversions.

The setup shown in figure 7.8 was used to pump the OPO in all of the experiments in this section. After the laser, there was a pinhole in order to take away some of the higher order modes, and thus increasing the beam quality. Further on, a BG18 filter was inserted in the beam path, in order to the minimize the light at 1064 nm.

The emission from the laser was horizontally linearly polarized. However, the orientation of the PPKTP crystals in the setup required vertically polarized light. This means that the polarization had to be rotated, which was done with a half-wave plate. Together with a polarizer, transmitting light polarized in the vertical direction, it was possible to adjust the outgoing power by rotating the wave-plate.

The two next following lenses acted as a telescope, so that the beam diameter was reduced. In the telescope, an aperture stop (AS) was placed in order to take away scattering and some higher order modes. Finally, a last lens with focal length $f = 100$ mm, focused the beam so that a beam waist of $w_0 = 225$ μm was obtained. With this focus, the damage threshold of the KTP crystal was reached at a pulse energy of 2 mJ. The beam quality factor of the pump after the last lens was measured to $M^2 = 6$, using the knife-edge technique (see appendix).

7.6.2 Temperature tuning of the OPO

In order to keep the costs of the project down, available crystals should in first hand be used, instead of manufacturing new crystals. However, since there was no crystal with the desired grating period 13.44 μm, temperature tuning of the existing crystals was tried. The experimental setup, in addition to the steps described in the last section, is sketched in figure 7.9. The incoupling mirror was plano-concave, with a radius of 500 mm, made out of
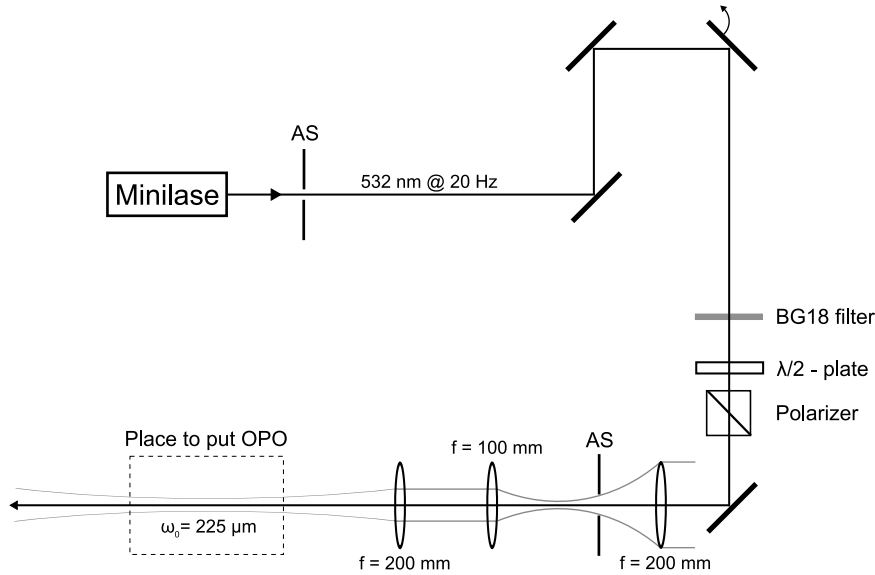
Figure 7.8. *General setup that was used for the experiments in this section. The laser source was a flash-lamp pumped Nd:YAG laser with internal frequency doubling. The dashed box indicates the position, where the OPO was placed in the later experiments.*

BK7 glass and coated to be HT @ 532 nm and HR @ 590-700 nm. The flat outcoupling mirror was made out of CaF_2, in order to be transparent for the idler at 3 μm, and it was coated to have a reflectance of 50 % @ 600-750 nm. Furthermore, the transmittance at 532 nm was larger than 90 % and the reflectivity at 3 microns was smaller than 7 %.

The crystal with the grating period closest to 13.44 μm was an 11 mm long KTP crystal, with three different poling periods: 12.7 μm, 13.1 μm and 13.5 μm. The lengths of each of the periodically poled areas were $L_{eff} = 9$ mm. In order to be able to control the temperature of the crystal, the crystal was placed on a copper holder, which was temperature controlled with a peltier element connected to a temperature controller: Profile's TED 350. Figure 7.10 and 7.11 shows the result of the temperature tuning measurements of the signal, for the grating periods 13.1 μm and 13.5 μm, respectively. The wavelength was measured with the pump power held at 2.3 times above the pump threshold.

The measurements showed that it was not possible to use the tested grating periods in order to obtain a signal at 634.5 nm with the available temperature supply: For the grating period 13.1 μm, a temperature of 165 °C was predicted to be necessary, in order to achieve the sought signal wave-
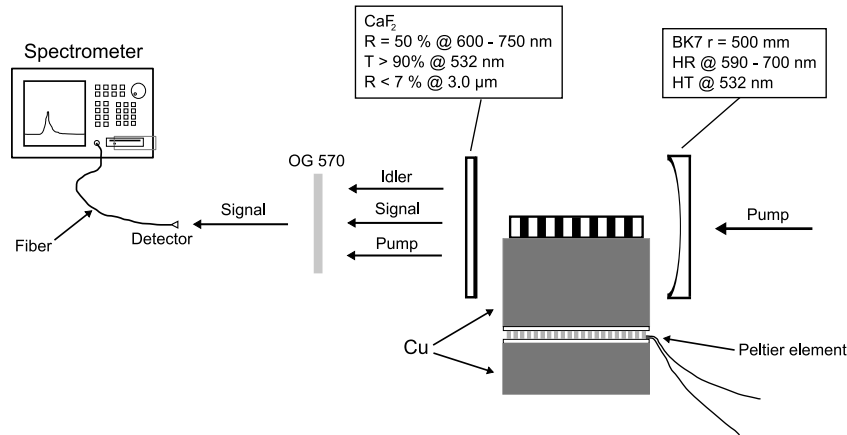
Figure 7.9. *Sketch of the temperature tuning setup, without focusing lenses and attenuation filters before the detector. The temperature detector, which was attached to the upper copper part, is not drawn in the figure.*

length. Such a high temperature would probably have destroyed the peltier element. An oven would have solved this, but there were no ovens ready to use in the lab. In any case, an oven would have been inconvenient to use due to its size. For the grating period 13.5 μm, a temperature of -10 °C was predicted. The peltier element would probably have been able to keep the low temperature, however, the crystal would have been covered with condensed water and ice. Of course this issue could have been solved by using a nitrogen atmosphere, but that would have been very impractical.

Instead of manufacturing a new PP crystal or constructing an oven, we decided to use the signal wavelength 632.0 nm, a wavelength which could be obtained with the crystal with the grating period 13.5 μm (at room temperature), heated to approximately 42 °C.

A comment that can be made regarding the temperature tuning simulations, the results of which are shown in figures 7.10 and 7.11, is that the grating periods in the simulations had to be adjusted to 13.12 μm and 13.52 μm, respectively, in order to achieve a good absolute correspondence between the measured values and the simulations. In the simulations, a combination of Fradkin's and Fan's Sellmeier equations were used, just as described in section 7.5. The discrepancies between the measured values and the simulations are probably caused by the uncertainty in Fradkin's Sellmeier equation around 3 μm. It should however be pointed out, that the rates of temperature changes, i.e. the slopes of the curves, are approximately the same before and after the adjustment. The differences are just the vertical placements of the lines.
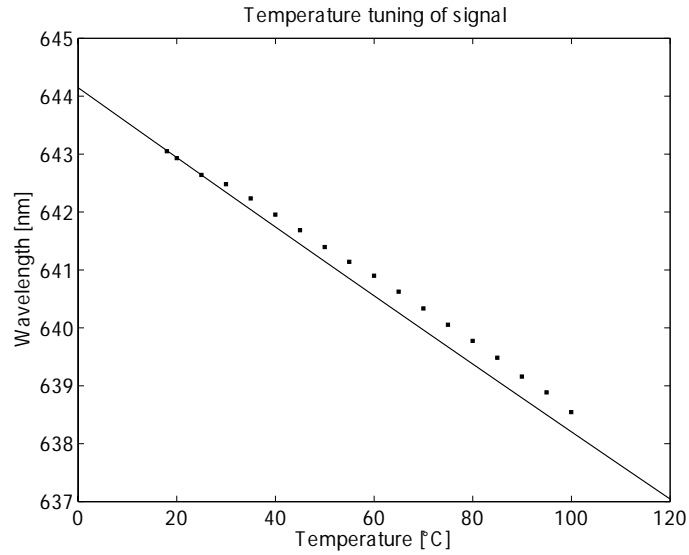
Figure 7.10. *Temperature tuning of the signal in a PPKTP crystal, with a grating period of 13.1 μm. The squares indicates the measured values and the line indicates the simulated temperature behavior.*

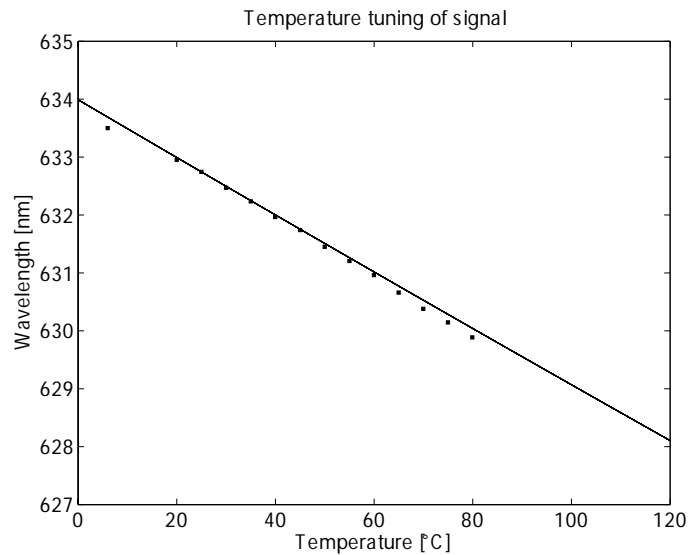**Figure 7.11.** *Temperature tuning of the signal in a PPKTP crystal, with a grating period of 13.5 μm. The squares indicates the measured values and the line indicates the simulated temperature behavior.*

7.6.3 Pump depletion and conversion efficiency

Two important characteristics of an OPO are the pump depletion and conversion efficiency. The pump depletion just depends on the pump and can be calculated through $1 - P_{pump,dep}^{out}/P_{pump,undep}^{out}$, where $P_{pump,dep}^{out}$ denotes the depleted pump and $P_{pump,undep}^{out}$ denotes the undepleted pump. Depleted pump means the outgoing pump, when there are signal and idler generated. Undepleted pump means the outgoing pump, when no signal and idler are generated. For the OPO in the setup, the pump depletion was indirectly measured for different incident pump powers, by measuring the depleted and undepleted pumps. The undepleted pump was measured, after the cavity had been misaligned, so that no signal was generated. In order to be able to just measure the pump, a green filter was placed after the OPO.

The conversion efficiency is calculated through $\eta_{eff} = (P_{idler}^{out} + P_{signal}^{out})/P_{pump}^{in}$, and as can be seen, it also depends on the outgoing signal and idler. For the OPO in the setup, the conversion efficiency was determined by measuring the outgoing signal power in addition to the incident pump power. To filter out the green light, OG570 filters were used. Unfortunately the idler power was not measured and therefore it had to be calculated theoretically by assuming that for each outgoing signal photon, one idler photon was also emitted from the OPO. In reality probably some fraction of the idler photons is absorbed in the PPTKP crystal.

The results of the measurements are shown in figure 7.12. Note that the pump depletion and conversion efficiency are plotted as function of the pulse energy *inside* the PPKTP crystal. By comparing the two quantities, it is possible to determine if there are any losses of the signal and idler in the system. From the figure, it is clear that there actually are losses of the signal somewhere in the cavity. This can be caused by several problems. Firstly, there could be cascaded interactions, like SFG between the pump and the signal, between the pump and the idler or between the signal and idler, that take away some of the energy from the signal and the idler. Secondly, there could be losses due to a crack, that was observed in the crystal. Thirdly, there might be diffraction losses in the cavity, caused by an unstable cavity. The difference in the beam quality values M^2 between the idler and signal (see next section) can be a sign of this. However, the difference in the beam quality values can also have several other origins as discussed earlier.

7.6.4 Signal and idler beam quality

The signal beam quality was measured using the technique described in the appendix. One lens directly after the OPO produced a beam waist approximately 200 mm further away. A second lens positioned 400 mm behind the first lens, focused the diverging light onto the power meter. To take away all green emission, two OG570 filters were put into the beam
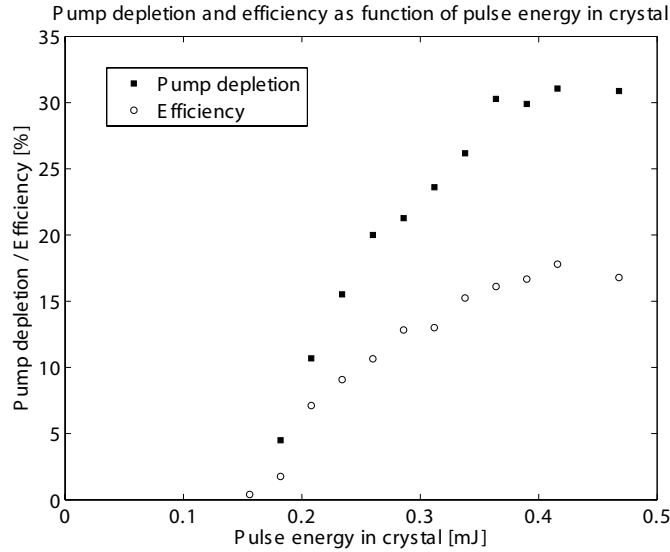
Figure 7.12. *Pump depletion and conversion efficiency as function of pulse energy inside the crystal.*

path. The idler was absorbed in the two filters and in the two following BK7 lenses, and therefore no additional filters were needed for filtering away that wavelength. As in the appendix, both the beam radius at the waist and the beam radius some distance further away from the beam waist were measured. From the measurements, the beam quality factor was estimated to be $M^2 = 5.5$, at a pulse energy of 0.90 mJ, and the signal beam waist in the OPO was estimated to be approximately $w_0 = 220$ μm.

The idler beam quality was slightly more complicated to measure, because the wavelength around 3 μm was of course not visible and could not be detected with any of the IR detector cards available in the lab. Instead a PbS detector was used to track the beam. Another important aspect of the idler wavelength, was that ordinary lenses could not be used, since they are not transparent so far into the IR region. In the setup one Germanium (Ge) lens, with focal length $f = 5'' \approx 127$ mm, and one Zinc Selenide (ZnSe) lens, with focal length $f \approx 80$ mm, were used. Both of these lenses absorbed a part of the idler radiation. However, this was not an issue, because in the razor blade technique, only the relative intensity changes are of interest, not the absolute intensity changes. Note that the measurement technique was in principle the same as the one described above for the signal.

The PbS detector was coupled to an oscilloscope (Tektronix TDS 5104). The area under pulses detected on the oscilloscope was used as a measure of the intensity, and in order to get accurate values of the areas, the oscilloscope was set to take the mean value of a large number of measurements. With the
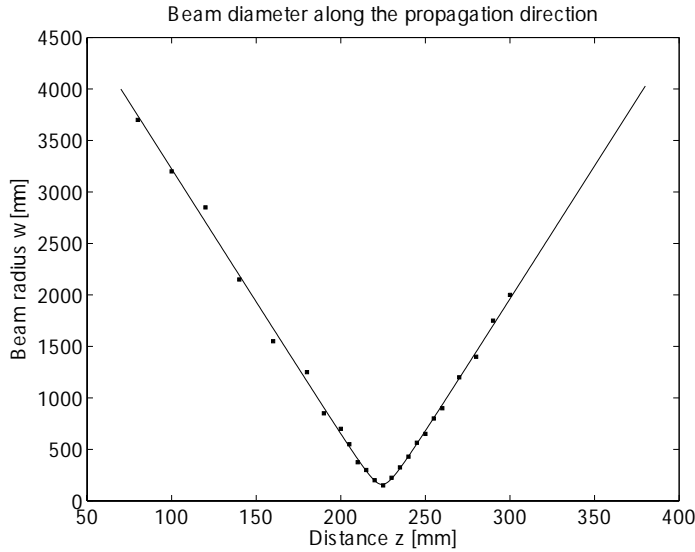
Figure 7.13. *Measured values of the beam radius along the beam propagation direction. The line is the fit of equation A.4 to the measured values. From the curve fit, the beam quality factor is determined to be $M^2 = 3.9$.*

setup ready to use, the beam radius was measured for some points around the beam waist, keeping the incident pulse energies at 0.95 mJ. The result is plotted in figure 7.13. By doing a parameter fit of equation A.4 to the data, using Gauss-Newton's method with the parameters w_0, M and z_0 as fitting parameters, the beam quality factor was determined to be $M^2 = 3.9$. The beam waist of the idler in the OPO was estimated to $w_0 = 185$ μm.

Table 7.14 summarizes the important results of this section. As can be seen, the fundamental modes of the different beams overlap quite good. The beam quality, on the other hand, differs quite a lot between the different beams. This can be due to several reasons. Firstly, the higher order modes of the pump beam might overlap with lower order modes of the signal and idler, and therefore only the lower order modes of the signal and idler might be amplified. This in turn might lead to better beam quality for the signal and idler than for the pump. The phenomena is directly linked to the diffraction and becomes very clear here due to the large differences in the wavelengths. Secondly, the signal oscillates in the cavity, in contrast to the pump and idler, and therefore its beam radius and its beam quality factor also depend on the cavity condition.

7.6.5 Test of different SFG configurations

Two different crystals were examined for the SFG process. The first crystal had three different grating periods: 9.10 μm, 9.20 μm and 9.33 μm, and the

	w_0 [μm]	M^2	$\omega_{00} = \omega_0/M$ [μm]
Pump	225	6.0	92
Signal	220	5.5	94
Idler	185	3.9	94

Table 7.14. *Beam waists in the OPO and beam quality factors for the different beams.*

second crystal had a grating period of 9.5 μm.

The SFG crystal could either be put in the cavity or after the cavity, as seen in figure 7.14. Commonly the intra-cavity mode is more efficient than the extra-cavity mode. However, this had to be tested for the actual system. To make the extra-cavity mode setup as simple as possible, the SFG crystal was put close to the OPO-cavity, so that no lenses were needed to refocus the pump at 532 nm and the idler at 3362 nm. Using lenses, would probably also have required that the wavelengths were split up and focused separately, in order to achieve a good focus overlap. Different types of lenses for the pump and the idler would also have been needed, because there were no lenses available, fully transmitting both the signal and the idler. If such lenses were available, a single ray system could have been constructed. However, the design of such a system would not have been easy, taking into account chromatic aberrations.

For each of the grating periods, the temperature was tuned in order to achieve as high blue power as possible. When the signal wavelength was held at 632.0 nm ($T_{OPO} = 42$ °C), and hence the idler wavelength held at 3362 nm, the highest blue power was obtained in the extra-cavity mode, with the grating period 9.5 μm and the SFG crystal heated to 55 °C. But the pulse energy was very low - less than 1 μJ. When the signal wavelength was tuned to 632.8 nm ($T_{OPO} = 26$ °C), and hence the idler tuned to 3340 nm, the highest blue power was obtained when the SFG crystal was heated to 30°C.

7.6.6 Spectral bandwidth of signal and sum

The spectrum of the OPO signal is plotted in figure 7.15. Since there is always a certain spread in angle of the generated signal, the frequency will always be slightly angle dependent. In order to measure the full bandwidth, a lens was therefore used to collect the diverging light and focus it onto the detector. Furthermore, one NG4 and one NG5 filter were placed in the beam path to lower the intensity of the incident light, so that the detectors in the spectrometer did not become saturated. From the measured spectrum, the spectral bandwidth is estimated to be $\delta\lambda_s = 0.2$ nm.

The spectrum of the idler could not be measured with the spectrometer in the lab, and therefore the spectrum of the idler must be calculated from
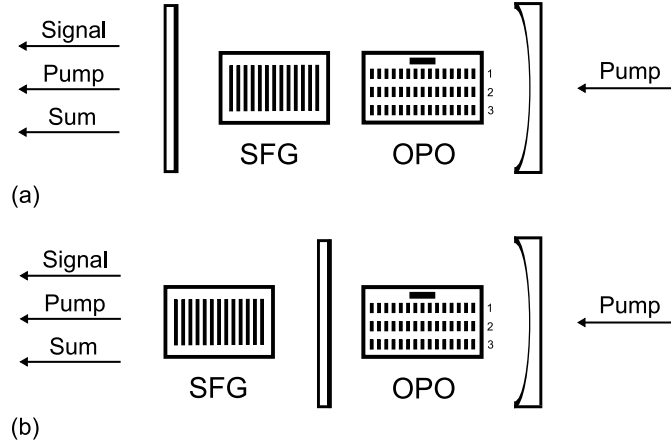
Figure 7.14. *Cavity configurations viewed from above.* **(a)** *Intra-cavity sum frequency generation.* **(b)** *Extra-cavity sum frequency generation. The numbers 1, 2 and 3 on the OPO crystal indicates the grating periods 12.7 μm, 13.1 μm and 13.5 μm, respectively.*

the signal. It can be shown from the law of energy conservation, that $\delta\lambda_i = (\lambda_i/\lambda_s)^2 \delta\lambda_s$. This gives an idler bandwidth of $\delta\lambda_i = 5.1$ nm.

In figure 7.16, the spectrum of the sum is shown. The bandwidth is estimated to be around $\delta\lambda_{sum} = 0.2$ nm.

7.6.7   Determination of the effective nonlinear coefficients

In order to be able to evaluate the results later on, it is important to know the effective nonlinear coefficients of the crystals used. The nonlinear coefficient of a crystal can be determined in several ways.

One way is to build an OPO based on the crystal and measure the pump threshold. From the pump threshold, the effective nonlinear coefficient can then be calculated using a technique described in reference [54]. For the crystal with the grating period 13.5 μm, an OPO has already been built and characterized. Using the technique described in reference [54], the pump threshold found from the measurements gives an effective nonlinear coefficient of $d_{eff} = 17.4$ pm/V. In order to determine the effective nonlinear coefficient of the crystal with the poling period 9.5 μm, a new OPO had to be built. This OPO generated a signal at 848 nm and an idler at 1429 nm. Again the pump threshold was determined, and from the determined value, the effective nonlinear coefficient was calculated to be $d_{eff} = 9.2$ pm/V.

The values of the effective nonlinear coefficients of the crystals calculated above are higher than expected, especially when considering the low
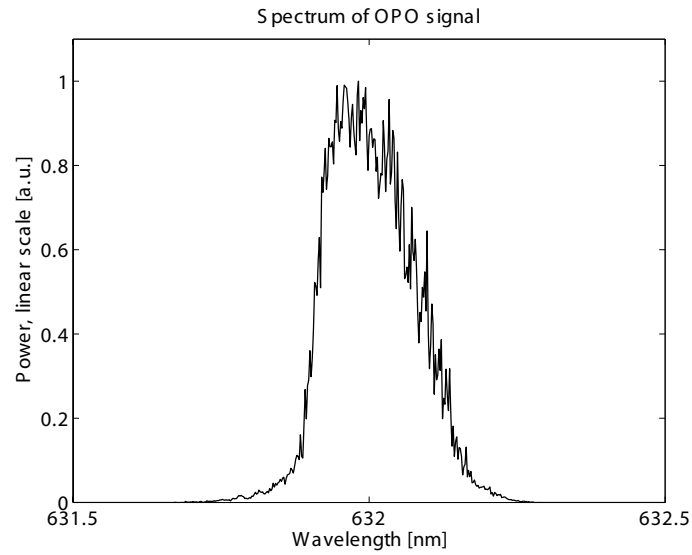
Figure 7.15. *Spectrum of the OPO signal. The bandwidth is approximately $\delta\lambda_i = 0.2$ nm.*
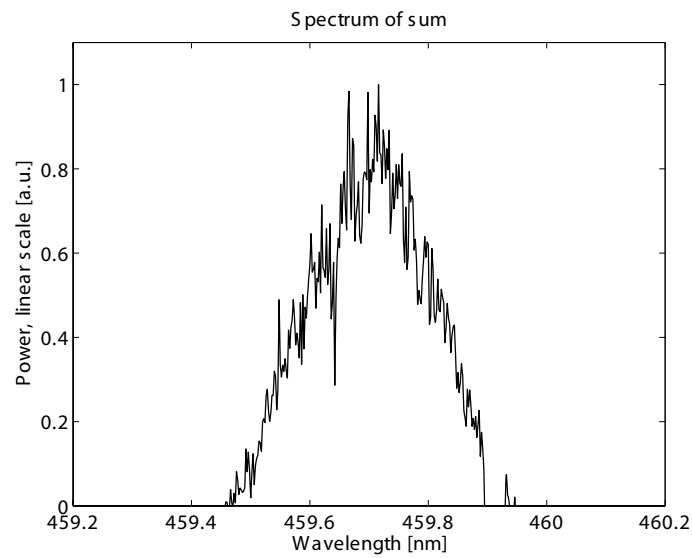

Figure 7.16. *Spectrum of the sum. The bandwidth is approximately $\delta\lambda_{sum} = 0.2$ nm.*

89

conversion efficiencies of the OPO:s. A reason for the overestimations can be that the theoretical calculations do not take into account that the beams have different M^2 values.

Since the results above were not satisfactory, another method had to be utilized in order to determine the effective nonlinear coefficients of the crystals more accurately. In this second method, the crystals were kept at room temperature, while pumped with a tunable Ti:Sapphire laser. The wavelength of the laser was set so that third order quasi-phase matching was achieved for second harmonic generation in the crystal. The reason why not utilizing first order quasi-phase matching was simply that the laser was not tunable to high enough wavelengths.

After the wavelength had been set, the second harmonic power after the crystal was measured as function of the pump power. From the measured data, it was possible to determine the effective nonlinear coefficient of the crystal by using a variant of equation 6.23. For the crystal with the poling period 13.5 μm, the effective nonlinear coefficient was determined to be $d_{eff} = 15.5$ pm/V, and for the crystal with the poling period 9.5 μm, the coefficient was determined to be $d_{eff} = 9.2$ pm/V.

When evaluating the found effective nonlinear coefficients, it is important to note that the crystals were not coated for the wavelengths of the second harmonics generated in this experiment, but for other wavelengths, which means that the reflectance of the second harmonics at the apertures of the crystals could have been fairly high. This in turn could have resulted in interference effects in the crystals, which would have increased the conversion. In that case, the effective nonlinear coefficients would have been overestimated. Probably this was the case for the coefficient measured for the crystal with the grating period 13.5 μm. The conclusion of these measurements must therefore be that in order to do more accurate measurements, the crystals must either be coated for the wavelengths used in the measurements, or they should not be coated at all before the measurements are performed. Alternatively, the crystals could be slightly rotated in order to prevent interference effects. Unfortunately there was no time to evaluate such a procedure within this project.

In addition to the effective nonlinear coefficients, the effective lengths of the crystals were also determined. This was done by first measuring both the wavelength for which the maximum power of the second harmonic was achieved and the wavelength for which the second harmonic power was lowered to the half of its maximum value. Then by letting $L = L_{eff}$ in equation 6.23, it was realized that the effective length could be calculated through $L_{eff} = 0.8806\pi/\Delta k$. For the crystal with the poling period 13.5 μm, the effective length was determined to be 5.8 mm, and for the crystal with the poling period 9.5 μm, the effective length was determined to be 6.1 mm. This can be compared to the physical lengths of the poled regions, which were measured to be 9.0 mm and 8.5 mm for the crystals with the grating

periods 13.5 μm and 9.5 μm, respectively.

7.7 Discussion of primary experiments

The experiments showed that the pump depletion in the OPO was low, but also that the difference in the pump depletion and efficiency was large. This combination meant low red and idler output powers. The low idler power in turn affected the SFG process, so that also the blue output power became low. However, only the low idler power, could not explain the very low blue power - there also had to be other reasons why the efficiency of the SFG process was so low. One explanation could be that the pump and idler beam radiuses in the SFG crystal were quite large, caused by bad pump and idler beam qualities. A solution to this problem would be to put the crystals even closer together. In the extreme case, one could make a single crystal with both of the periods inside. Another solution would be to use focusing optics after the OPO cavity, as discussed earlier. Besides from lowering the intensities of the fields, the high M^2 values could also have resulted in a bad modal overlap of the beams, which in turn would have decreased the conversion efficiency of the SFG process.

In addition to bad beam quality, also the large spectral bandwidth of the idler could have been an important factor why so low blue power was obtained. In figure 7.17, the acceptance bandwidth of the SFG process at the idler wavelength is plotted together with the idler spectrum, which has been calculated from the measured signal spectrum, assuming negligible bandwidth at 532 nm. From the figure, it is obvious that a large part of the idler power is waisted.

7.8 Suggestions for frequency narrowing setups

In order to narrow the idler bandwidth, different techniques can be used, see figure 7.18. Setup (a) uses a volume Bragg grating (VBG) as outcoupling mirror, with a grating period giving a peak reflectivity at the idler wavelength. With this setup, it is possible to directly influence the bandwidth of the idler.[55] A VBG with thickness between 5 and 7 mm, would for instance give a FWHM selectivity between 1 and 1.5 nm. However, there are several disadvantages with letting the idler resonate. Firstly, the absorption of the idler in the volume Bragg grating is very high - approximately 8 %/mm is absorbed already when the diffraction efficiency is as low as 80 %. Secondly, the grating period of these volume bragg gratings comes with a quite large uncertainty; according to one of the manufacturer's specifications, the peak reflectivity could vary as much as 10 nm from the specified wavelength. Thirdly, it would be quite hard to align the idler-resonant cavity, due to the fact that the idler is so far in the IR.

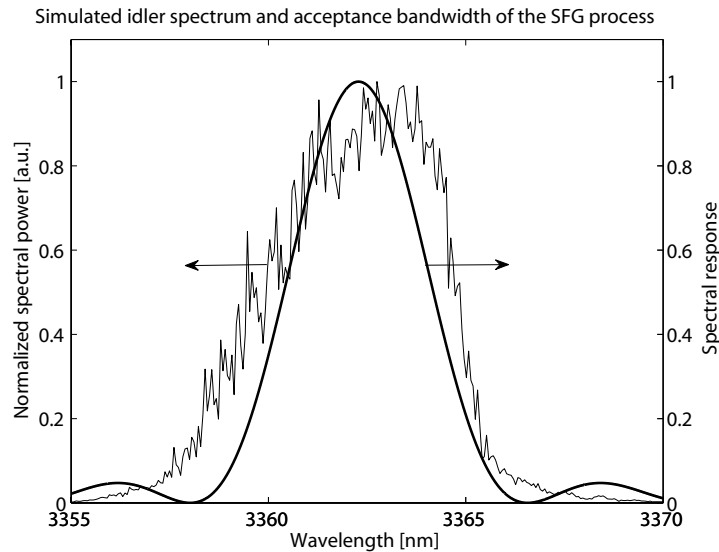A way of getting around the difficulties described above, would be to

Simulated idler spectrum and acceptance bandwidth of the SFG process

Figure 7.17. *Plot of the acceptance bandwidth of the SFG crystal (bold line) and the spectrum of the idler (thin line) calculated from the measured signal spectrum.*

make the signal resonant instead of the idler, as in setup (b). In this way the idler bandwidth would be indirectly narrowed, as the signal bandwidth is narrowed. Note, however, that in order to be able to use the idler in the SFG process outside the OPO, a CaF_2 mirror must be used as output coupler, because of the absorption of the idler in quartz glass. Therefore the VBG has to be moved to the incoupling side. However, this has a disadvantage, because the pump at 532 nm is partly absorbed and scattered in the volume Bragg grating. At a glance, a solution to this problem, in the case when the selectivity is not that critical, seems to be to just make the grating thinner. However, when the grating becomes thinner, the amplitude modulation of the refractive index has to be made larger, in order to maintain the diffraction efficiency of the VBG. This in turn increases the absorption (and the scattering losses). For a 5 mm thick VBG with 98 % diffraction efficiency, the absorption (together with the scattering losses) could be as high as 15 % at 532 nm according to one manufacturer.

Setup (c) uses a reflective surface diffraction grating in order to obtain a narrowband feedback. Both the so called Littrow and Littman (drawn) configurations could be implemented. For a more thoroughly discussion about these configurations, see for instance reference [68]. It must be noted that there are several disadvantages with this type of feedback systems. Firstly, they are more complicated to build than for instance setup (b) above. Secondly, the reflection gratings can take damage if the peak intensity is too high. This can partly be prevented by letting a dichroic mirror reflect only

a fraction of the signal or idler power onto the grating. Finally, the beam spot size on the grating needs to be large, because the feedback wavelength becomes narrower if it is incident with a larger number of grooves.

The final setup (d) is an OPO seeded with an external narrowband laser. (Probably it would here be possible to just use an OPA, instead of an OPO.) This setup gives a bandwidth determined by the seeding laser. One could of course argue that the idea with an OPO vanishes, if there is an external laser available emitting at the sought wavelength; the initial idea of an OPO is indeed that the wavelength can be tuned to regions not reachable by other lasers. In most cases also narrowing techniques need to be applied to the seeding laser, and hence the bandwidth problem is just moved from one place to another. Nevertheless, higher output power can in many cases be achieved with a seeded OPO, in comparison to the seeding laser itself. At this point it should be mentioned, that the initial goal of this thesis was to build a single source RGB laser, and with injection seeding the original concept is lost.

7.9 Experiment with volume Bragg grating

According to the discussion in the previous section, the setup depicted in figure 7.18 (b) seems to be the most promising frequency narrowing configuration, and therefore this configuration has been examined experimentally. The volume Bragg grating, which was used in the experiments, was manufactured by OptiGrate. The peak reflectivity of the grating was specified to be 633.2 nm and the FWHM bandwidth was specified to be 0.2 nm. Measurements showed that the diffraction efficiency of the grating was 92 % and that the losses in the grating exceeded 6 % of the incident power. The transmission at 532 nm was measured to be approximately 76 %. (The faces of the VBG were AR coated both at 532 nm and at 633 nm.)

The experimental setup in front of the OPO was almost identical with the setup depicted in figure 7.8, except that the last lens was changed to a lens with focal length 250 mm. This gave a beam waist of 240 μm. The beam quality of the pump after the last lens was measured to be $M^2 = 3.0$.

In the OPO configuration (see figure 7.18 (b)), the same OPO crystal as earlier was used ($\Lambda = 13.5$ μm), but now the temperature of the crystal was held at 19.3 °C. As for the experiments with the curved mirror in section 7.6.3, the pump depletion and the efficiency were measured for different pump energies. The result is plotted in figure 7.20. Reference measurements were done for an OPO with a flat BK7 mirror as incoupler, see figure 7.21. The losses were high in both OPO configurations, but slightly higher in the OPO with the VBG as incoupler. In figure 7.19, the signal and idler energies are plotted as a function of the pump energy for the two different cases. As can be seen, the flat mirror configuration is slightly more efficient than the VBG configuration. The most important observation from the figures is
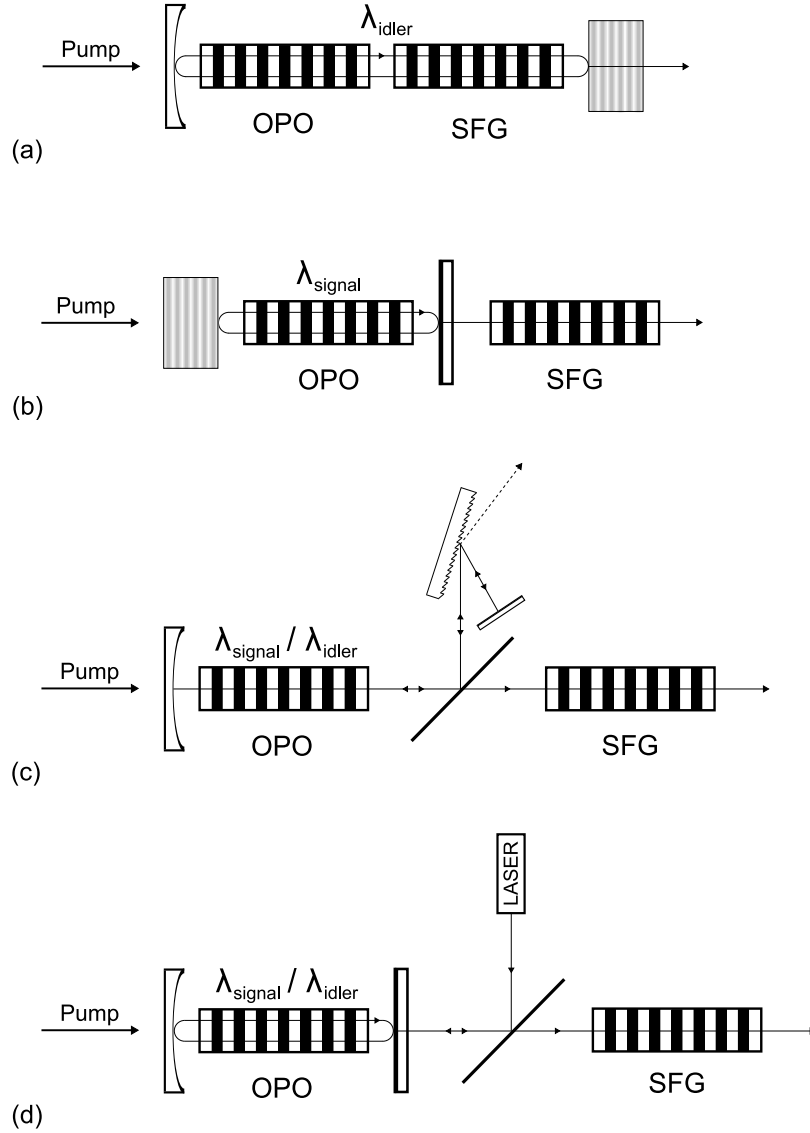
Figure 7.18. *Different techniques to obtain narrow bandwidths at the signal and idler wavelengths.* **(a)** *Idler resonant OPO setup with a reflection Bragg grating as output coupler.* **(b)** *Signal resonant OPO setup with a reflection Bragg grating as input coupler.* **(c)** *A dichroic mirror, acting as output coupler, reflects a fraction of the signal or idler onto a reflective diffraction grating in Littman configuration, which gives a narrow bandwidth feedback into the OPO.* **(d)** *Injection seeding by an external laser into the OPO cavity.*

however that there were high losses of the idler in both of the OPO:s; the expected power ratio between the idler and signal is 1:0.19, but the measured ratio was 1:0.12, meaning that almost 37 % of the idler was lost in the OPO. For the OPO with the VBG as incoupler, both the signal and idler beam qualities were measured to be $M^2 = 4.0$ at a pump energy of approximately 0.5 mJ (in the OPO crystal).
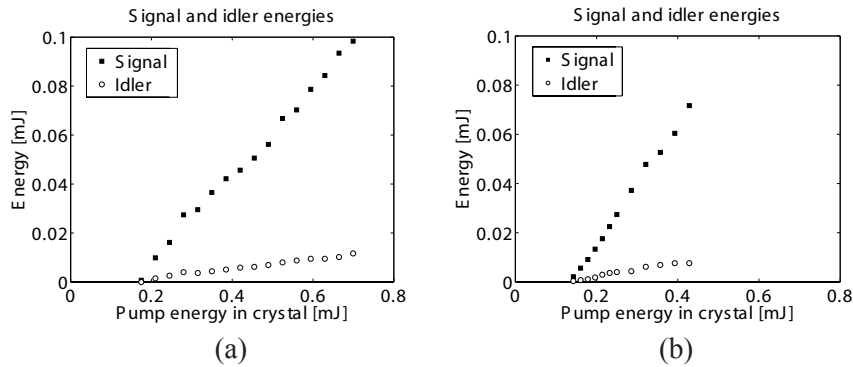

Figure 7.19. *Signal and idler energies as a function of the pump energy for an OPO with a VBG as incoupler (a) and for an OPO with a flat mirror as incoupler (b).*

In order to be able to evaluate the performance of the frequency narrowing configuration, the spectrum of the signal was measured and compared with the spectrum obtained when a flat mirror was used, see figure 7.22. Since the bandwidth in the normal case depends on the gain (see section 6.4.2), the spectra were recorded at different pump powers. From the measurement results, three important observations can be made. Firstly it can be seen that the bandwidth was more than 50 % narrower in the case when a VBG was used, compared to the case when a flat mirror was used. Secondly the bandwidth of the signal obtained from the VBG configuration did not change when the pump power was increased, in contrast to the bandwidth of the signal obtained from the configuration with the flat mirror, which was strongly dependent on the pump power. Thirdly the VBG locked the spectral peak at the peak reflectivity of the grating. With the flat mirror the spectral peak fluctuated a little bit.

With a narrower signal spectrum, and therefore a narrower idler spectrum, the sum frequency process was believed to become more efficient. To test this predication, the sum frequency crystal ($\Lambda = 9.5$ μm, $T = 17.5$ °C) was placed after the OPO and the blue power was measured as function of the pump power. The result is shown in figure 7.23. As can be seen, the blue power did not increase much when the flat mirror was replaced by the VBG. An important comment is however that the measurement of the
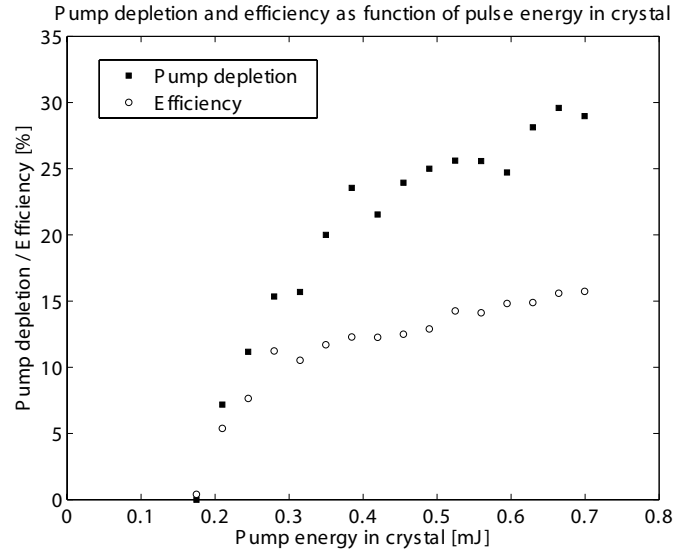
Figure 7.20. *Measured pump depletion and efficiency as a function of the pump energy for an OPO with a volume Bragg grating as incoupler.*
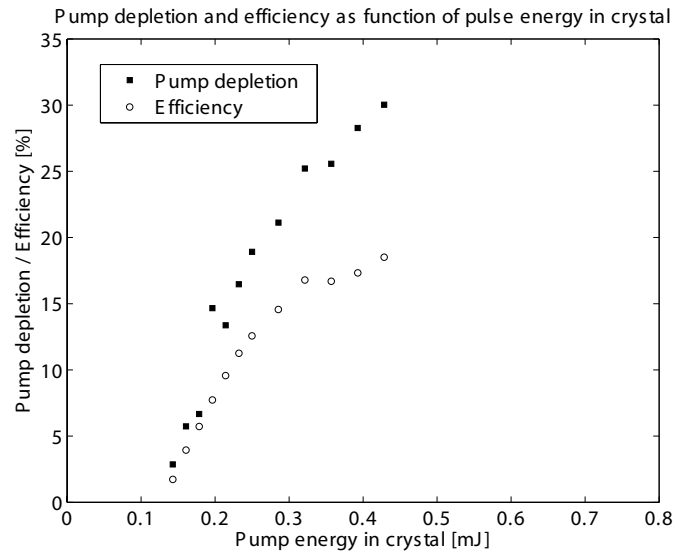

Figure 7.21. *Measured pump depletion and efficiency as a function of the pump energy for an OPO with a flat BK7 mirror as incoupler. No data points are available for pump energies above 0.45 mJ in this case, since the upper limit of the pump energy in the OPO crystal was reached as a consequence of that the incoupling mirror only transmitted 41 % of the incident pump energy.*
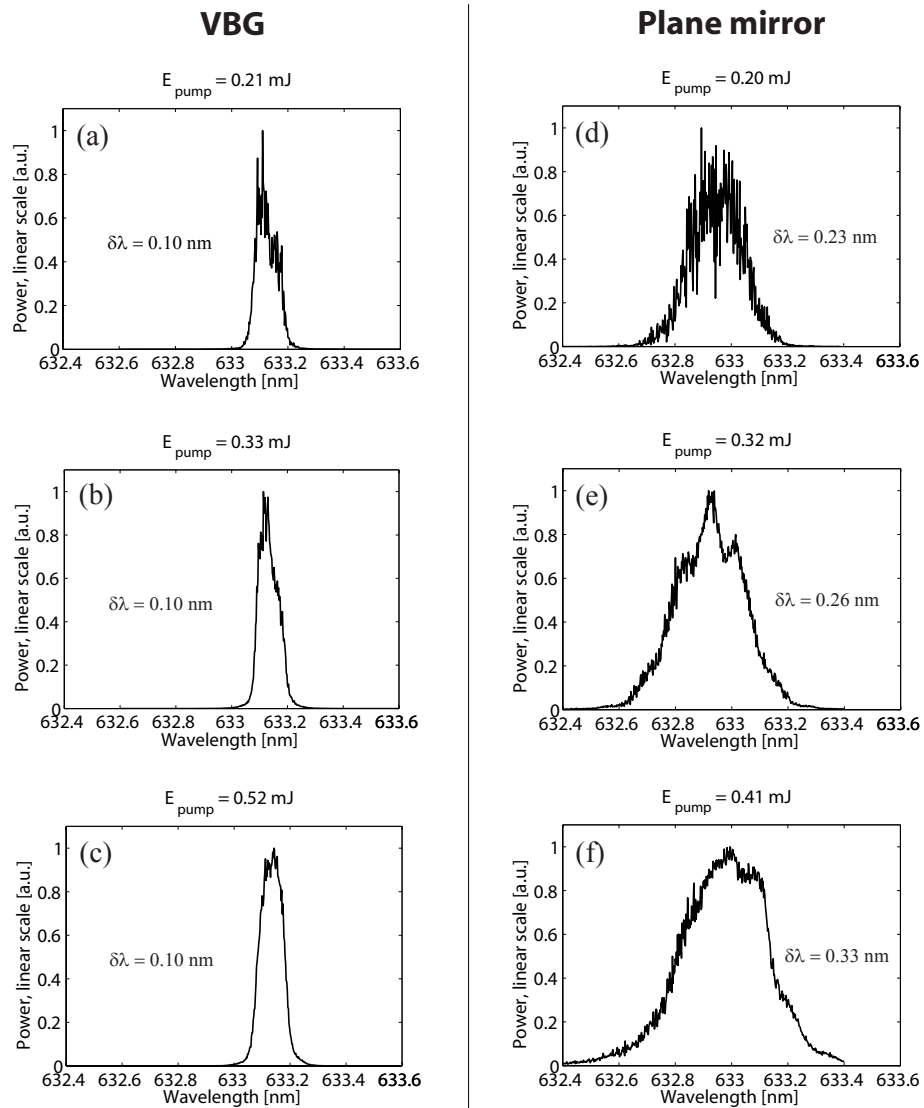
Figure 7.22. *Spectra of the signal in the case where a VBG was used as incoupler (a-c) and in the case where a plane mirror was used as incoupler (d-f). The spectra were measured close to the pump threshold (a,d), two times above the pump threshold (b,e), and at high pump power (c,f).*

blue power obtained from the configuration with the flat mirror was very unstable; the value fluctuated over 100 %, which rises the question if one could trust the result.
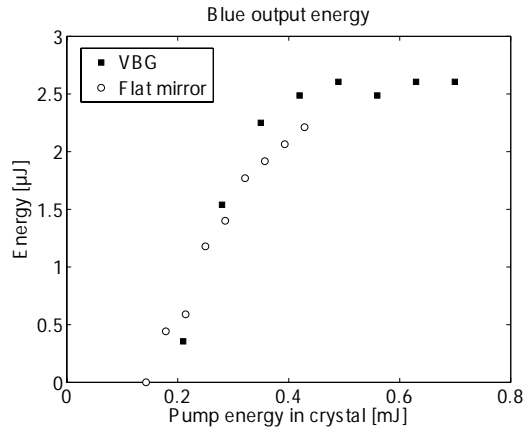

Figure 7.23. *Blue output energy as a function of the pump energy in the OPO crystal in the case where a VBG was used as incoupler (■) and in the case where a flat mirror was used as incoupler (○). The measurement of the blue power in the latter case was very unstable.*

In order to be able to discuss the results later on, it is important to know the bandwidth of the pump and the sum. With the spectrum analyzer both of these bandwidths were determined to be 0.1 nm.

Another interesting property of the OPO is the temporal behavior. In figure 7.24, the temporal pulse shapes of the undepleted pump and the depleted pump are plotted, as well as the pulse shapes of the signal (red) and sum (blue) outputs. From the figure, it can be seen that the red pulse starts approximately 3 ns after the pump pulse starts. This means that it takes the pump pulse approximately 3 ns to reach the OPO threshold.

7.10 Discussion of experiment with volume Bragg grating

The measurements in the last section showed that the bandwidth of the signal was narrowed when a VBG was used as incoupler, which was an expected result. Despite this the blue power did not increase considerably. This could just be a measurement problem, since the measured blue power from the OPO with the flat incoupler was very unstable. But, this could also be a sign that the model used to describe the sum frequency process in figure 7.17 was too simplified; the model assumed negligible bandwidth at 532 nm, but experimentally the bandwidth was measured to be around 0.1 nm. However, one must remember that the resolution of the spectrum analyzer was specified to be 0.05 nm, which means that the relative measurement uncertainty of such a narrow spectrum is large.
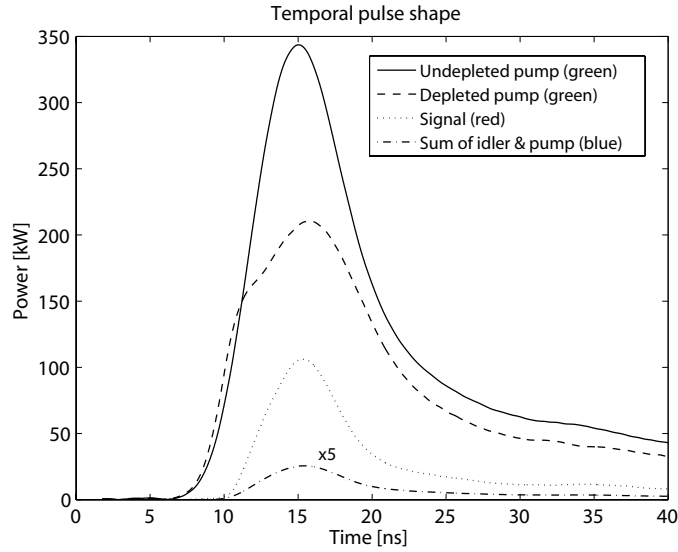
Figure 7.24. *Temporal pulse shapes measured after the OPO. Note that the amplitude of the blue pulse is multiplied by five in order to make the shape more visible. The small shift between the depleted and undepleted pulses was caused by a small measurement error.*

In order to investigate the frequency narrowing setup further, the model describing the sum frequency process need to be developed in order to take account for the pump spectrum. Experimentally, a spectrum analyzer with better resolution, such as a Fabry-Perot interferometer, would be needed for further analysis.

7.11 Experiments using a high average power laser with good beam quality

In order to investigate how the beam quality of the pump at 532 nm affected the performance of the RGB system, the pump source was changed to a diode-pumped Nd:YVO$_4$ laser (Edgewave INNOSLAB IS41-E). This laser emitted light at 1064.3 nm with a beam quality of $M_x^2 = 1.9$ in the horizontal direction and $M_y^2 = 1.3$ in the vertical direction. During the experiments, the average output power from the laser was kept at approximately 20 W at a pulse repetition frequency of 10 kHz. In order to reduce the average output power, a chopper which reduced the power with 94 % was used. This meant that the average pulse repetition frequency after the chopper became approximately 600 Hz.

As a first step in the RGB system, the light at 1064.3 nm had to be converted into light at 532.2 nm. For this purpose a 4 mm long PPKTP crystal with grating period 9.01 μm was used. In order to be able to fit

the output beam from the laser into the SHG crystal, the beam had to be resized, and therefore a telescope was built (see figure 7.25). Directly after the telescope, the beam radius was measured to be 480 μm in the horizontal direction and 360 μm in the vertical direction. Phase matching for the SHG process was obtained at a temperature of 27.1 °C, and at an incoming pump power of 1.07 W, a conversion efficiency of 51 % was achieved. The beam quality of the outgoing green light was measured to be $M_x^2 = 1.5$ in the horizontal direction and $M_y^2 = 1.1$ in the vertical direction.
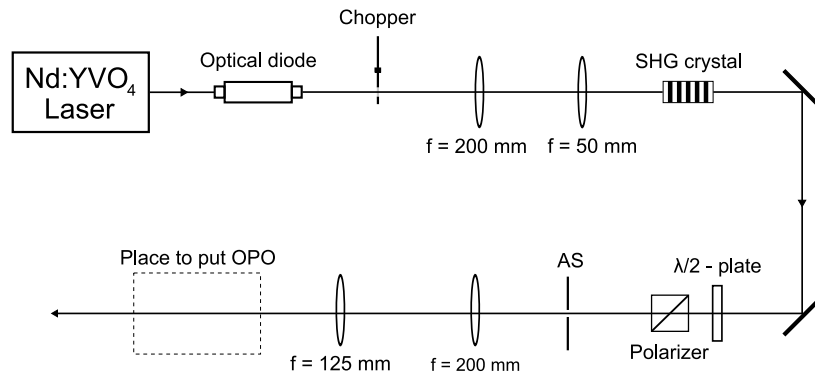

Figure 7.25. *Schematic sketch of the experimental setup. Note that only the most important optical components are drawn in the figure.*

After the SHG crystal, three dichroic mirrors which had high reflectance at 532 nm and high transmission at 1064 nm were put in order to take away the rest of the radiation at 1064 nm (one mirror is missing in the figure). To be able to adjust the power at 532 nm, a half-wave plate and a polarizer were placed after the mirrors. Since the beam at 532 nm was slightly divergent, it had be resized in order to fit into the OPO crystal. A second telescope was therefore used, as shown in figure 7.25. With this second telescope, a beam radius of 270 μm was obtained in both the horizontal and vertical direction at the position where the OPO crystal was later on put.

7.11.1 Extra-cavity mode

The extensively examined OPO setup in previous sections was configured in extra-cavity mode. Therefore we started the examination of the OPO based on the new laser source by using this type of configuration. Note however that in the experiments which will be described below, a VBG with peak reflectivity at 632.4 nm ($R \approx 90\%$, Losses $\approx 6\%$) had to be utilized instead of the VBG with peak reflectivity at 633.2 nm utilized in the earlier experiments. The reason for this was that the Nd:YVO$_4$ laser emitted light at 1064.3 nm, i.e. at a slightly longer wavelength than emitted from the

Nd:YAG laser used in previous experiments. This in turn gave a green pump at 532.2 nm (instead of 532.1 nm as earlier), which together with a signal at 633.2 nm gave a phase matching temperature around 0 °C for the SFG process. Due to the risk of condensation, such a system was not practically usable. However, with a signal at 632.4 nm ($T_{OPO} = 30.0$ °C) instead, phase matching was achieved at the much more convenient temperature $T_{SFG} = 34.0$ °C.

In figure 7.27 the pump depletion and efficiency are plotted as function of the pump energy at 532 nm in the OPO crystal. Comparing this figure with figure 7.20, one can see that the pump depletion and efficiency were slightly lower in this new setup than in the previous setup, but also that the threshold was slightly lower in the new setup. In figure 7.28 the output energies are plotted. The signal and idler energies were measured directly after the OPO and the blue energies were measured after the SFG crystal. Also shown in the figure are the theoretical idler energies calculated from the signal energy. As can be seen, the obtained energy ratio between the signal and idler was approximately 1:0.11, which can be compared with the theoretical ratio 1:0.19. Hence, as in the previous setups, there were large losses in the OPO cavity.

In figure 7.26 (a), a close-up plot of the blue energy can be found, and in figure 7.26 (b), the temperature phase matching curve of the SFG process is plotted. By comparing figure 7.26 (a) with figure 7.23, two important differences are apparent. Firstly, one can see that the blue output energy is considerably higher when better beam quality is used. Secondly, there is a linear dependence between the input pump power and the output blue power in figure 7.26 (a), which is not the case in figure 7.23.

From the measurement data, one could calculate that approximately 18 % of the idler photons which are sent into the SFG crystal are used for the generation of blue photons.

7.11.2 Intra-cavity mode

Experiments were also done on the RGB system configured in intra-cavity mode. In figure 7.29 the pump depletion and efficiency of the intra-cavity system are plotted as function of the pump energy in the OPO crystal. The pump depletion was simply measured in the same way as if the SFG crystal had not been in the cavity, i.e. the depletion of the pump origin from the SFG process was included in these measurements. This resulted in a rather high pump depletion. Furthermore, the efficiency was calculated by assuming that an idler photon was emitted from the cavity for every signal photon, which of course resulted in an overestimation of the value. Despite this, the efficiency anyway became low, see figure 7.29. A reason for this could be that the signal energy was partly lost in the cavity due to the fact that the coatings of the SFG crystal was not optimized for the red

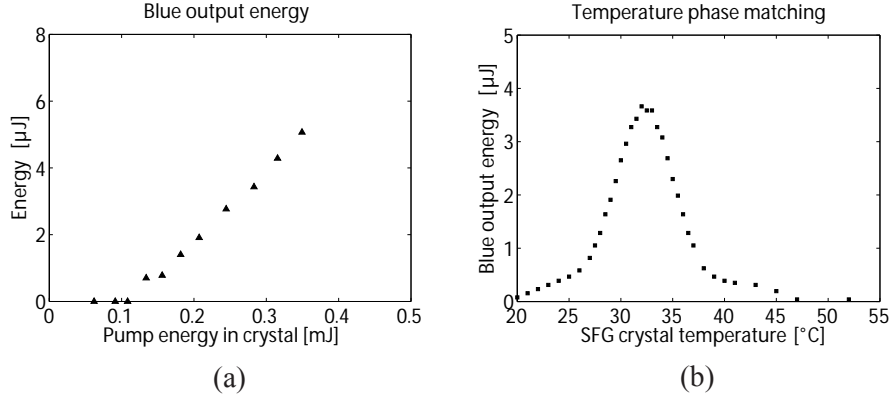**Figure 7.26.** **(a)** *Blue output energy as function of the green pump
energy in the OPO crystal (extra-cavity mode).* **(b)** *Temperature phase
matching of the SFG process.*

wavelength.

The output energies from the cavity are plotted in figure 7.30 and a close-
up plot of the blue output energy can be found in figure 7.31. It should be
noted that at a pump energy of 0.35 mJ approximately 36 % more blue
output energy was achieved with the intra-cavity mode setup than with the
extra-cavity mode setup. The red output energy on the other hand decreased
with 15 %, probably due to the coatings of the SFG crystal.

The highest average pump power used was 330 mW (measured before
the OPO). At this pump power, the average output powers were 24.2 mW,
117 mW and 4.4 mW at the red, green and blue wavelengths, respectively.

The beam quality of the outgoing signal was measured to be $M_x^2 = 8.5$ in
the horizontal direction and $M_y^2 = 5.4$ in the vertical direction. The quality
of the blue beam was even worse: $M_x^2 = 11.2$ in the horizontal direction and
$M_y^2 = 9.4$ in the vertical direction.

7.12 Discussion of measurements performed using a pump source with good beam quality

The experiments in this section showed that better beam quality just slightly
improves the red output energy, but drastically increases the blue output
energy. For instance, when the system was configured in extra-cavity mode
and the OPO was pumped with a beam with quality $M^2 = 6$, a red out-
put pulse energy of 41 μJ and a blue output pulse energy of 2.4 μJ were
obtained at a pump energy of 350 μJ in the OPO crystal. However, with
a beam quality of $M^2 = 1.5$ x 1.1, a red output pulse energy of 41 μJ and
a blue output pulse energy of 5.0 μJ were achieved. Hence, the red output
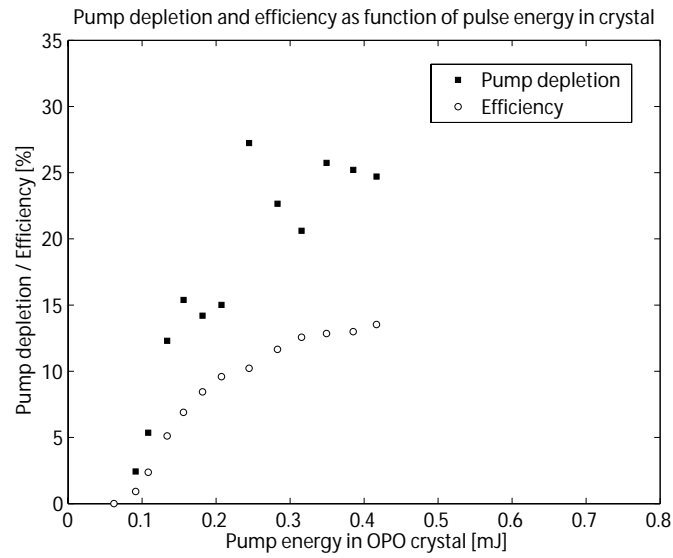
Figure 7.27. *Pump depletion and conversion efficiency as function of the green pulse energy inside the OPO crystal (extra-cavity mode).*
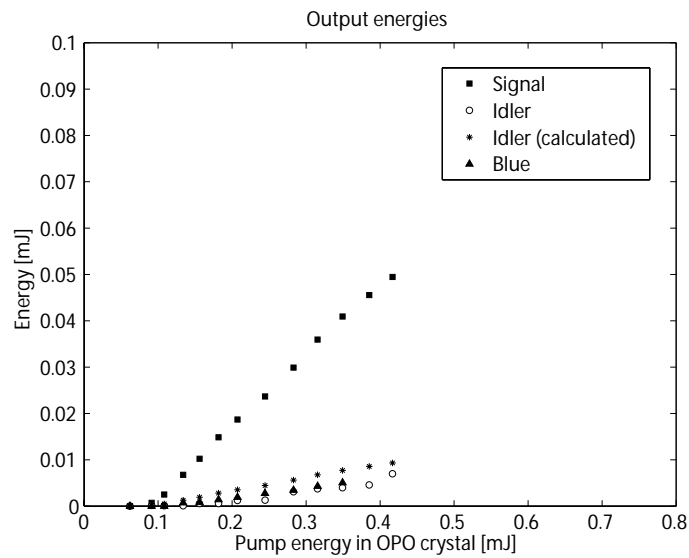

Figure 7.28. *Output energies from the RGB system in extra-cavity SFG configuration. The signal and idler energies were measured directly after the OPO, and the blue energy was measured after the SFG crystal.*
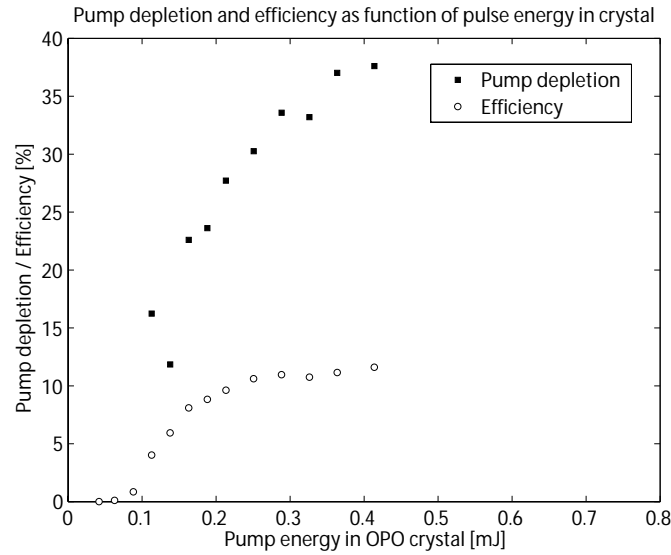
Figure 7.29. *Pump depletion and conversion efficiency as function of the green pulse energy inside the OPO crystal (intra-cavity mode). Note that the plotted pump depletion includes the depletion origin from the SFG process.*
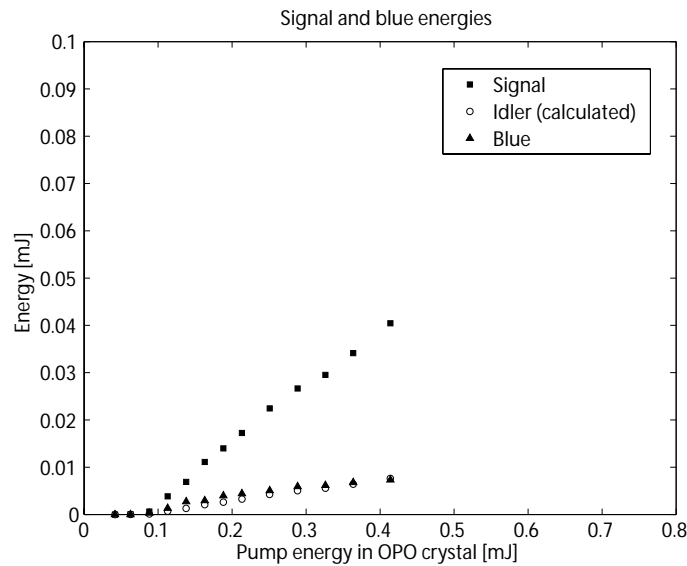

Figure 7.30. *Output energies from the RGB system with intra-cavity SFG.*

Figure 7.31. *Blue output energy as function of the green pump energy in the OPO crystal (intra-cavity mode).*

energy increased with 18 % and the blue energy increased with almost 108 % when the pump source was changed. An important remark is however that the two different experiments were performed using two slightly different pump wavelengths, which meant that two different VBG:s had to be utilized. However, since the charcteristics of the VBG:s were quite similar, this ought not have altered the performance of the system to a larger extent.

With intra-cavity SFG the highest conversion from the pump to blue was obtained; at a pump energy of 350 μJ in the OPO crystal, a blue output energy of 6.7 μJ was achieved. However, as already mentioned the red output energy decreased using this type of mode.

8 Conclusions and outlook

In this chapter, the main results of this project will be summarized and conclusions will be made. Based on the conclusions, proposals for future studies will be discussed.

8.1 Q-switched laser source

8.1.1 Results

In this part of the project, actively Q-switched solid-state lasers based on an electrooptic modulator were constructed and evaluated. The electrooptic modulator consisted of two RTP crystals rotated 90 degrees relative each other in order to compensate for the birefringence in the crystals (see figure 4.1). The rise time of the modulator was measured to be 15 ns.

When the laser cavity had an outcoupling of 10 %, a pulse energy of 12 μJ was obtained at a pulse repetition frequency of 1000 Hz. When the outcoupling was increased to 15 %, the pulse energy increased to 36 μJ. The peak pulse power was then measured to be 1.1 kW and the pulse length was estimated to be 25 ns. A saturable absorber with an initial transmission of 94 % increased the pulse energy slightly to 39 μJ.

8.1.2 Conclusions

The low output energies from the lasers were probably caused by the imperfect birefringence compensation in the electrooptic modulator (see discussion in section 5.3). In order to obtain higher pulse energies, the matching between the crystals must be improved. With the holder used in this project, it was hard to obtain good matching since the relative alignment between the crystals could not be changed after the crystals had been glued onto the holder. Neither it was possible to measure the compensation performance at the same time as the crystals were glued onto the holder, since no realtime polarization analyzer was available in the lab.

8.1.3 Future work

In order to obtain a good relative alignment between the crystals when gluing them onto the holder, some sort of alignment laser setup with a realtime polarization analyzer must be used. A completely different solution to the matching problem would be to construct a holder, with which one could change the positions of the two crystals independently of each other. These two solutions have not been examined in this project, but might be interesting for future studies.

A recommendation for future work is also to use RTP crystals with larger apertures than used in this project (1.0 x 1.0 mm^2), since crystals with larger

apertures would be easier to align in the cavity. However, larger apertures also implies that a higher voltage over the crystals is needed, and hence a better pulse amplifier than used in this project have to be used.

8.2 Frequency conversion stage

8.2.1 Results

The frequency conversion stage examined in this work was based on nonlinear processes in periodically poled KTP. In the initial experiments an OPO was pumped with a Q-switched frequency-doubled Nd:YAG laser emitting green light at 532 nm at a pulse repetition frequency of 20 Hz. The beam quality of this pump was $M^2 = 6$. When the OPO crystal, which had a poling period of 13.5 μm, was heated to 42 °C, a signal at 632.0 nm and an idler at 3362 nm were obtained. At a pump energy of 0.5 mJ, the pump depletion was measured to 30 % and the efficiency was measured to 18 %.

In a crystal placed directly after the OPO, the sum and the idler were sum frequency mixed, which gave blue at 459.3 nm. The crystal, which had a poling period of 9.5 μm, was heated to 55 °C in order to obtain phase matching. However, only a maximum of 2.2 μJ of blue energy was achieved (at the maximum pump energy 420 mJ in the OPO crystal). The low blue output energy was believed to have several reasons. Firstly, low intensities of the pump and the idler in the SFG crystal gave a low conversion efficiency. Secondly, the bandwidth of the idler was much broader than the acceptance bandwidth of the SFG process, which also resulted in a low conversion efficiency. Thirdly, the idler was partly absorbed in the KTP crystals.

In this work, an attempt was made to solve the second issue, i.e. the broad bandwidth of the idler. By using a volume Bragg grating as incoupler to the OPO, the bandwidth of the signal was decreased by 50 %. The bandwidth of the idler was believed to decrease by the same fraction. Despite this, the blue output power did not increase as expected.

A final experiment showed that the blue output energy was strongly dependent on the beam quality of the pump at 532 nm: When the OPO was pumped with a beam with quality $M^2 = 6$, a blue output pulse energy of 2.4 μJ was obtained at a pump pulse energy of 350 μJ in the OPO crystal. However, with a beam quality of $M^2 = 1.5$ x 1.1, a blue output pulse energy of 5.0 μJ was achieved at the same pump energy. An important remark here is that the two different experiments were performed using two slightly different pump wavelengths, which meant that two different VBG:s had to be utilized. However, since the characteristics of the VBG:s were quite similar, this ought not have altered the performance of the system to a larger extent. Hence, the conclusion must be that the 108 % higher blue output pulse energy in the latter experiment was to a large extent caused

by the improved beam quality.

The setup which was most efficient in the generation of blue energy from the pump energy was an OPO configuration with intra-cavity SFG pumped with green light of good beam quality. From this system, a red pulse energy of 40.4 μJ and a blue pulse energy of 7.3 μJ were achieved at a pump energy of 415 μJ in the OPO crystal. The average output powers were 24.2 mW, 117 mW and 4.4 mW at the red, green and blue wavelengths, respectively.

8.2.2 Conclusions

The main conclusion of this work is that it is possible to obtain red and blue light from the frequency conversion stage which was designed and constructed within this project. The experiments showed however that it was hard to obtain enough blue power and the reasons for this were discussed. Further experimental work will be needed in order to find a satisfying solution to the problem.

An important observation from the experiments performed in this work is that the beam qualities of the red and blue beams are not good enough for the laser projection application. This is of course a critical issue which must be solved.

8.2.3 Future work

In order to maximize the performance of the system examined in this project, the crystals need to be AR coated at the wavelengths used; the AR coatings of the crystals in the experimental setup were not optimized for the wavelengths present, and therefore losses were introduced. Another improvement of the setup would be to use a nonlinear material with less absorption at the idler wavelength. A third improvement would be to refocus the pump and idler into the SFG crystal. Alternatively, the OPO and SFG crystals could be combined into a monolithic device, as described by Gao et al. [16] In such a configuration it would be interesting to use a volume Bragg grating as incoupling mirror.

For future studies it would also be interesting to investigate the two other systems presented in section 7.1. System 1, depicted in figure 7.1(a), would be interesting to examine, since the idler generated in the OPO would not be absorbed in the crystals. Note however that the expected efficiency of the system is only 7 % (see section 7.3). Furtheron, system 3, depicted in figure 7.1(c), would be interesting to examine, since there are more freedoms to control the energy flow through this system.

8.3 Outlook

The final goal of future work is to combine the Q-switched laser source and the frequency conversion stage into a ns-pulsed RGB laser with a pulse

repetition frequency of approximately 20 kHz and with an output power of several Watts. Such a device would probably be commercially competitive in the sector of large home cinema systems and smaller projection systems. It is therefore of great public interest to further develop the laser source and the frequency conversion stage.

Appendix

How to measure the beam radius w and the beam quality factor M^2

In most cases, the intensity distribution of the cross-section of a laser beam can be approximated to be Gaussian [31]:

$$I(r) = I_0 \exp\left(-2\,\frac{r^2}{w^2}\right) \tag{A.1}$$

where w is called the $1/e^2$ intensity radius. For a perfect Gaussian beam, the radius changes in the propagation direction, $\hat{\mathbf{e}}_z$, according to the following expression [31]:

$$w(z) = w_0^2\left[1 + \left(\frac{\lambda(z - z_0)}{\pi w_0^2}\right)^2\right] \tag{A.2}$$

where w_0 is the radius at the beam waist, and z_0 is the position of the beam waist. In the non-ideal case, for instance when higher order modes are involved, the beam is not Gaussian, and the above description is no longer valid. In order to be able to describe the propagation of a beam with an arbitrary intensity distribution, the beam radius must be defined through the second order intensity moment [69]:

$$< w_x(z)^2 > = 4\,\frac{\iint (x - x_c)^2 I(x, y, z)dxdy}{\iint I(x, y, z)dxdy} \tag{A.3}$$

where x_c is the x-coordinate of the intensity centroid. The corresponding expression for the y-direction is obvious. The change of the second order moment along the beam propagation direction is now given by:

$$< w_{x,y}(z)^2 > = < w_{0x,0y}^2 >\left[1 + \left(\frac{\lambda\,M^2(z - z_0)}{\pi < w_{0x,0y}^2 >}\right)^2\right] \tag{A.4}$$

where M^2 is called the beam propagation factor or beam quality factor. For a perfect Gaussian beam $M^2 = 1$, otherwise $M^2 > 1$.[69]

In order to measure the beam waist and the beam quality factor, different techniques can be used. In fact, there are some special procedures which are ISO standardized (EN ISO 11146).[69] Two of them include the calculation of the intensity moment from intensity distribution. If the intensity distribution cannot be measured with high enough accuracy, there are three other methods based on power meter measurements which can be used. However, in order to be able correlate the results from the methods
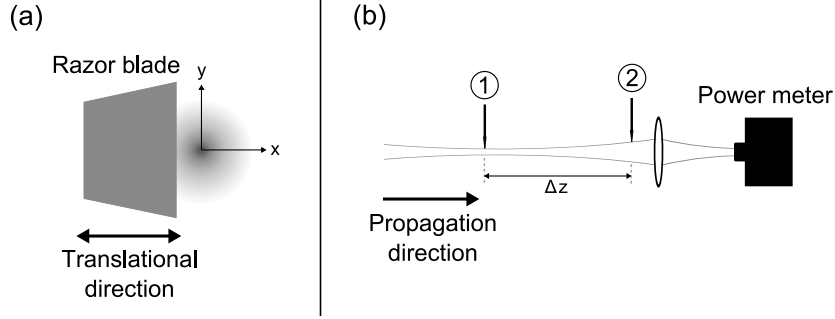
Figure A.1. *Principle of the moving knife edge technique. **(a)** A razor blade is translated across the beam in the x-direction and the power of the beam after the razor blade is detected by a power meter. The beam radius w is then given as the translational distance between the positions where 16 % and 84 % of the total beam power are detected. **(b)** The beam quality factor M^2 can be found by measuring the beam radius at the beam waist (1) and some Rayleigh lengths further away (2).*

based on power meter measurements, with the results from the methods based on intensity distribution measurements, corrections must be made, see reference [69].

In this diploma thesis project, the beam radii were measured using the so called *moving knife edge technique.*[70, 69] The principle is illustrated in figure A.1. A metal with sharp edge, here a razor blade, cuts the laser beam from one side. By assuming Gaussian distribution of the intensity in the beam cross-section, the detected power after the razor blade as function of the razor blade position x is given by:

$$P(x) = \frac{P_{tot}}{2} \left(1 + \mathrm{erf} \left(\sqrt{2} \, \frac{x}{w_{uc}} \right) \right) \tag{A.5}$$

where w_{uc} is the uncorrected beam radius. From this formula, one can easily deduce that the uncorrected radius is given by $w_{uc} = x_1 - x_2$, if x_1 is the position where 16 % of the total power is measured and x_2 is the position where 84 % of the total power is measured. Due to the high uncertainty of the measurements in this project, caused by the unstability of the laser etc., the differences between the corrected and uncorrected beam radii were in most cases smaller than the measurement errors, which means that it has not been critical to correct the uncorrected beam radii. Hence, during this work, the beam radii have simply been assumed to be equal to the uncorrected beam radii, i.e. $w = w_{uc}$.

The beam quality factor M^2 can be determined by first measuring the beam radius at the waist and a couple of Rayleigh lengths further away. The quality factor is then given by expression A.4 with the second order intensity moments replaced by the measured beam radii. Just as in the case of the

measured beam radii, the measured M^2 values have not been corrected in this project. It should also be noted that the ISO standardized procedure requires that the beam radius is measured at more than ten points along the beam path, see reference [69].

References

[1] Greg Niven. Laser TV: coming to a home theatre near you. *Optics & Lasers Europe*, pages 33–34, September 2006.

[2] Coherent and Osram collaborate on laser TV. `http://compoundsemiconductor.net/articles/news/10/12/21`, 2006 (accessed March 19, 2007).

[3] Felix Brunner, Edith Innerhofer, Sergio V. Marchese, Thomas Südmeyer, Rüdiger Paschotta, Takeshi Usami, Hiromasa Ito, Sunao Kurimura, Kenji Kitamura, Gunnar Arisholm, and Ursula Keller. Powerful red-green-blue laser source pumped with a mode-locked thin disk laser. *Optics letters*, 29(16):1921–1923, August 2004.

[4] DLP, Texas Instruments. `http://www.dlp.com`, 2007 (accessed March 19, 2007).

[5] Stephen Fenech. Laser TV to topple plasma. `http://www.news.com.au`, 2006 (accessed March 19, 2007).

[6] Future Sony televisions feature laser projection. `http://compoundsemiconductor.net/articles/news/11/1/10`, 2007 (accessed March 19, 2007).

[7] Greg Niven and Aram Mooradian. Trends in Laser Light Sources for Projection Display. `http://www.novalux.com/assets/downloads/IDW%20Novalux%20Paper.pdf`, 2006 (accessed March 20, 2007).

[8] Rüdiger Paschotta. Encyclopedia of laser physics and technology. `http://www.rp-photonics.com/encyclopedia.html`, 2007 (accessed January 26, 2007).

[9] Jenoptik AG. `http://www.jenoptik-laserdisplay.de`, 2007 (accessed March 19, 2007).

[10] Anna Fragemann. Design and construction of a laser display and a new electro-optic modulator. Master's thesis, Lund Institute of Technology, Lund, Sweden, 2001.

[11] Alain Brenier, Chaoyang Tu, Zhaojie Zhu, and Baichang Wu. Red-green-blue generation from a lone dual-wavelength $GdAl_3(BO_3)_4$:Nd^{3+} laser. *Applied Physics*, 84(12):2034–2036, March 2004.

[12] J. Capmany. Simultaneous generation of red, green and blue continuous-wave laser radiation in Nd^{3+}-doped aperiodically poled lithium niobate. *Applied Physics Letters*, 78(2):144–146, January 2001.

[13] Edith Innerhofer, Felix Brunner, Sergio V. Marchese, Rüdiger Paschotta, and Ursula Keller. RGB source powers up - laser projection displays. *Photonics Spectra*, pages 50–54, June 2004.

[14] B. Henrich, T. Herrmann, J. Kleinbauer, R. Knappe, A. Nebel, and R. Wallenstein. Concepts and technologies of advanced RGB sources. In *Advanced Solid-State Lasers*, 2002.

[15] Peter F. Moulton, Kevin J. Snell, Dicky Lee, Kevin F. Wall, and Robert Bergstedt. High-power rgb laser source for displays. http://www.qpeak.com/Papers/IMAGE02/ Image%202002%20RGB%20OPO%20paper.pdf, 2002 (accessed March 20, 2007).

[16] Z.D. Gao, S.N. Zhu, Shih-Yu Tu, and A.H. Kung. Monolithic red-green-blue laser light source based on cascaded wavelength conversion in periodically poled stoichiometric lithium tantalate. *Applied Physics Letters*, 89:181101, October 2006.

[17] M. Robles-Agudo, R.S Cudney, and L.A. Ríos. RGB source based on simulataneous quasi-phase-matched second and third harmonic generation in periodically poled lithium niobate. *Optics express*, 14:10663–10668, October 2006.

[18] T W Ren, J L He, C Zhang, S N Zhu, Y Y Zhu, and Y Hang. Simultaneous generation of three primary colours using aperiodically poled LiTaO$_3$. *Journal of physics: Condensed matter*, 16:3289–3294, April 2004.

[19] H.X. Li, Y.X. Fan, S.N. Zhu, P. Lu, Z. D. Gao, H. T. Wang, Y. Y. Zhu, N. B. Ming, and J.L. He. 530-mW quasi-white-light generation using all-solid-state laser technique. *Journal of applied physics*, 96(12):7756–7758, December 2004.

[20] Bengt Lundh, editor. *Bra Böckers Stora Läkarlexikon*, volume 10, pages 178–179. Bokförlaget Bra Böcker AB, 1995.

[21] Wikipedia, the free encyclopedia. `http://en.wikipedia.org`, 2007.

[22] Helga Kolb, Eduardo Fernandez, Ralph Nelson, and Bryan William Jones. Webvision. `http://webvision.med.utah.edu/`, 2007 (accessed January 22, 2007).

[23] Max Born and Emil Wolf. *Principles of Optics*. Pergamon Press, 6:th edition, 1991.

[24] Gernot Hoffmann. CIE color space. `http://www.fho-emden.de/ ~hoffmann/ciexyz29082000.pdf`, 2007 (accessed January 26, 2007).

REFERENCES

[25] Stefan Spiekermann. *Compact diode-pumped solid-state lasers.* PhD thesis, KTH, Royal Institute of Technology, Stockholm, Sweden, 2004.

[26] Steven K. Shevell. *The Science of Color.* Elsevier, 2:nd edition, 2003.

[27] Günther Wyszecki and W.S. Stiles. *Color science.* John Wiley & Sons, 2:nd edition, 2000.

[28] RIT Munsell Color Science Laboratory. Ask a color scientist! `http://www.cis.rit.edu/mcsl/outreach/faq.php?catnum=0\#249`, 2007 (accessed January 26, 2007).

[29] Eugene Hecht. *Optics.* Addison Wesley, 4:th edition, 2002.

[30] Peter Günter. Elektro-optik, 2006. Manuscript from course in electro optics given at ETH Zürich.

[31] Amnon Yariv. *Quantum electronics.* John Wiley & Sons, 3:rd edition, 1989.

[32] J.F. Nye. *Physical properties of crystals: their representation by tensors and matrices.* Clarendon press, 1957.

[33] Cristal Laser S.A. RTP - technical data. `http://www.cristal-laser.fr/prod_pdf/tech5.pdf`, 2006 (accessed December 27, 2006).

[34] Red Optronics. RTP - technical data. `http://www.redoptronics.com/RTP-crystal.html`, 2006 (accessed December 27, 2006).

[35] Lambda Corporation. RTP - technical data. `http://www.lphotonics.com/products/Non-Linear%20Crystals/RTP.htm`, 2006 (accessed December 27, 2006).

[36] M. Roth, M. Tseitlin, and N. Angert. Oxide crystals for electro-optic q-switching of lasers. *Glass physics and chemistry*, 31(1):86–95, January 2005.

[37] Raicol crystals. http://www.raicol.com/, 2007 (accessed March 29, 2007).

[38] Christopher A. Ebbers and Stephan P. Velsko. High average power $KTiOPO_4$ electro-optic Q-switch. *Applied Physics Letters*, 67:593–595, July 1995.

[39] P.A. Morris and M.K. Crawford. Influence of water vapor on the susceptibility to electric-field damage of $KTiOPO_4$. *Applied Physics Letters*, 62(8):799–801, February 1993.

[40] John R. Quagliano, Roger R. Petrin, Thomas C. Trujillo, Nigel J. Cockroft, Mark T. Paffett, George Havrilla, Carl J. Maggiore, and John C. Jacco. An investigation of the chemical and physical properties of prestine, electrochromically damaged $KTiOPO_4$ (KTP) using surface analytical and optical spectroscopic techniques. In *Advanced Solid-State Lasers*, 1995.

[41] Anthony E. Siegman. *Lasers*. University Science Books, 1986.

[42] Stefan Bjurshagen. *Diode-pumped rare-earth-doped quasi-three-level lasers*. PhD thesis, KTH, Royal Institute of Technology, Stockholm, Sweden, 2005.

[43] Walter Koechner. *Solid-state laser engineering*. Springer-Verlag, 5:th edition, 1999.

[44] Mool C. Gupta. *Handbook of photonics*. CRC Press, 1997.

[45] Christoph Czeranowsky. *Resonatorinterne Frequenzverdopplung von diodengepumpten Neodym-Laser mit hohen Ausgangsleistungen im blauen Spektralbereich*. PhD thesis, Hamburg University, Hamburg, Germany, 2002.

[46] Ida Häggström. Monolithic single mode Nd-laser using a volume Bragg grating. Master's thesis, KTH, Royal Institute of Technology, Stockholm, Sweden, 2006.

[47] M.E. Innocenzi, H.T. Yura, C.L. Fincher, and R.A. Fields. Thermal modeling of continuous-wave end-pumped solid-state lasers. *Applied Physics Letters*, 56(19):1831–1833, May 1990.

[48] Richard L. Sutherland. *Handbook of nonlinear optics*. Marcel Dekker Inc., 1:st edition, 1996.

[49] Paul N. Butcher and David Cotter. *The elements of nonlinear optics*. Cambridge University Press, 1:st edition, 1990.

[50] Pär Jelger. UV light source for ozone detection. Master's thesis, Royal Institute of Technology, Stockholm, Sweden, 2005.

[51] Robert W. Boyd. *Nonlinear optics*. Academic Press Inc., 1:st edition, 1992.

[52] Shunhua Wang. *Fabrication and characterization of periodically-poled* KTP *and* Rb-*doped* KTP *for applications in the visible and* UV. PhD thesis, KTH, Royal Institute of Technology, Stockholm, Sweden, 2005.

[53] Mikael Tiihonen. *Spectral management in quasi-phasi-matched parametric devices.* PhD thesis, KTH, Royal Institute of Technology, Stockholm, Sweden, 2006.

[54] Jonas Hellström. *Nanosecond optical parametric oscillators and amplifiers based on periodically poled* KTiOPO$_4$. PhD thesis, KTH, Royal Institute of Technology, Stockholm, Sweden, 2001.

[55] Björn Jacobssson, Mikael Tiihonen, Valdas Pasiskevicius, and Fredrik Laurell. Narrowband bulk Bragg grating optical parametric oscillator. *Optics Letters*, 30(17):2281–2283, September 2005.

[56] Carlota Canalias. *Domain engineering in* KTiOPO$_4$. PhD thesis, KTH, Royal Institute of Technology, Stockholm, Sweden, 2005.

[57] Göran Hansson, Håkan Karlsson, Shunhua Wang, and Fredrik Laurell. Transmission measurements in KTP and isomorphic compounds. *Applied optics*, 39:5058–5069, September 2000.

[58] K. Fradkin, A. Arie, A. Skliar, and G.Rosenman. Tunable midinfrared source by difference frequency generation in bulk periodically poled KTiOPO$_4$. *Applied physics letters*, 74:914–916, February 1999.

[59] Tso Yee Fan, C.E. Huang, B.Q. Hu, R.C. Eckardt, Y.X. Fan, Robert L. Byer, and R.S. Feigelson. Second harmonic generation and accurate index of refraction measurements in flux-grown KTiOPO$_4$. *Applied optics*, 26:2390–2394, June 1987.

[60] Kiyoshi Kato and Eiko Takaoka. Sellmeier and thermo-optic dispersion formulas for KTP. *Applied optics*, 41:5040–5044, August 2002.

[61] W. Wiechmann, S. Kubota, T. Fukui, and H. Masuda. Refractive-index temperature derivatives of postassium titanyl phosphate. *Optics letters*, 18:1208–1209, August 1993.

[62] Gorachand Ghosh. Temperature dispersion in KTP for nonlinear devices. *IEEE Photonics technology letters*, 7:68–70, January 1995.

[63] Shai Emanueli and Ady Arie. Temperature-dependent dispersion equations for KTiOPO$_4$ and KTiOAsO$_4$. *Applied optics*, 42:6661–6665, November 2003.

[64] Sandia National Laboratories. `http://www.sandia.gov`, 2007 (accessed February 18, 2007).

[65] Arlee V. Smith. How to use SNLO nonlinear optics software to select nonlinear crystals and model their performance. In *Proceedings of SPIE*, volume 4972, 2003.

[66] Valdas Pascivicius. personal communication, 2006.

[67] Valdas Pasiskevicius, Shunhua Wang, Jens A. Tellefsen, Fredrik Laurell, and Håkan Karlsson. Efficient Nd:YAG laser frequency doubling with periodically poled KTP. *Applied Optics*, 37(30):7116–7119, October 1998.

[68] Stefano Bertani. Tunable laser diodes for oxygen sensing. Master's thesis, KTH, Royal Institute of Technology, Stockholm, Sweden, 2006.

[69] Norman Hodgson and Horst Weber. *Laser Resonators and Beam Propagation*. Springer-Verlag, 2:nd edition, 2005.

[70] Markus Henriksson. *Nanosecond tandem optical parametric oscillators for mid-infrared generation*. KTH, 2006.